KAUNAS UNIVERSITY OF TECHNOLOGY

JUSTINA ŠEŠTOKĖ

INVESTIGATION OF PMN-32%PT PIEZOELECTRIC CRYSTALS AND THEIR APPLICATION FOR AIR-COUPLED ULTRASONIC TRANSDUCERS AND ARRAYS

Doctoral dissertation
Technological Sciences, Measurement Engineering (10T)

2016, Kaunas

UDK 53.082.73 + 681.586.48](043.3)

The Doctoral Dissertation has been prepared during the period of 2012-2016 at Kaunas University of Technology, Professor Kazimieras Baršauskas Ultrasound Research Institute.

Scientific supervisor:

Prof. Dr. Habil. Rymantas Jonas KAŽYS (Kaunas University of Technology, Technological Sciences, Measurement Engineering, 10T).

Doctoral dissertation has been published in:
http://ktu.edu

Editor:

Armandas Rumšas (Publishing Office “Technologija”)

ISBN 978-609-02-1270-7

KAUNO TECHNOLOGIJOS UNIVERSITETAS

JUSTINA ŠEŠTOKĖ

PMN–32%PT PJEZOELEKTRINIŲ KRISTALŲ TYRIMAS IR JŲ TAIKYMAS ULTRAGARSINIAMS ORINIAMS KEITIKLIAMS BEI DAUGIAELEMENTĖMS GARDELĖMS

Daktaro disertacija
Technologijos mokslai, Matavimų inžinerija (10T)

2016, Kaunas

UDK 53.082.73 + 681.586.48](043.3)

Disertacija rengta 2012-2016 metais Kauno technologijos universiteto Prof. K. Baršausko ultragarso mokslo institute.

Mokslinis vadovas:

Prof. habil. Dr. Rymantas Jonas KAŽYS (Kauno technologijos universitetas, Technologijos mokslai, Matavimų inžinerija, 10T).

Interneto svetainės, kurioje skelbiama disertacija, adresas:
http://ktu.edu

Redagavo:

Armandas Rumšas (Leidykla “Technologija”)

ISBN 978-609-02-1270-7

INTRODUCTION

Relevance of the problem

Air-coupled ultrasonic techniques are already extensively used for material characterization, non-destructive evaluation [1-2] and even for secure wireless transmission of data [3]. The main currently encountered problem is the big losses of ultrasonic signals caused by the attenuation and significant mismatch of acoustic impedances of ultrasonic transducers and air. One of the ways of solving this issue is the application of composite piezoelectric elements whose specific acoustic impedance is lower than that of monolithic piezoelectric ceramics [4]. Performance of the 1 – 3 connectivity piezocomposite disks may be improved by matching layers made of materials with low acoustic impedance, for example, polypropylene foam ferroelectric film [5]. Further enhancement of the performance of ultrasonic air transducers is limited by the piezoelectric effect of the piezoelectric material being used.

The advent of novel piezoelectric materials with a very strong piezoelectric effect such as lead magnesium niobate – lead titanate [$PbMg_{1/3}Nb_{2/3}O_3$ – $PbTiO_3$ (PMN-PT)] crystals enables to improve the performance of ultrasonic transducers. The electromechanical coupling factors of PMN-32%PT crystals are very high. The electromechanical coupling factor for the thickness extension mode is $k_{33} > 0.90$, for the transverse shear mode it reaches as high as $k_{15} > 0.95$ whereas for the transverse extension it measures $k_{32} > (0.84 – 0.90)$. The properties of the PMN-32%PT crystals may be further improved by using domain engineering [6-8]. These parameters are of higher values than the comparable parameters of piezoelectric ceramic elements used as active elements in ultrasonic transducers.

PMN-32%PT crystals are already widely used in very high frequency ultrasonic phased arrays for medical applications [9], in ultrasonic transducers for non-destructive testing [10] and ultrasonic hydrophones [11]. Application of the PMN-32%PT crystals for air-coupled ultrasonic transducers was suggested in our previous works [12-14].

However, to the best of our knowledge, the PMN-32%PT piezoelectric element has never been systematically investigated before from the point of view of their application for air-coupled ultrasonic transducers and arrays.

Objective and tasks

The main objective of the dissertation is to analyse and develop measurement methods of the piezoelectric properties of PMN-PT single crystals during a poling process and to apply these crystals in novel air-coupled ultrasonic transducers and multi-element arrays. In order to achieve this objective, the following tasks were outlined:

1. To analyse the properties of PMN-32%PT piezoelectric crystals and methods of their measurements;

2. To develop a measurement technique for simultaneous monitoring of variations of the domain structure and piezoelectric coefficients during the poling process;
3. To conduct theoretical and experimental investigation of the vibrations of PMN-32%PT elements;
4. To develop wide band air-coupled ultrasonic transducers and arrays with enhanced performance.

Scientific innovation of the work

1. A novel measurement technique for simultaneous monitoring of the piezoelectric properties and structural changes of the PMN-32%PT single crystal during the poling process has been proposed and successfully implemented.
2. Numerical and experimental analysis of vibrations of piezoelectric PMN-32%PT crystals in steady state and transient modes has been performed. Ultrasonic air-coupled transducers and phased arrays operating in the range of low frequencies have been developed and investigated both in the transmitting and receiving modes.
3. The selection of the appropriate vibration modes and optimization of the geometry of PMN-32%PT crystals for air-coupled ultrasonic transducers and arrays has been made.

The practical application of the work

The research leading to these results received funding from the Lithuanian-Swiss cooperation programme seeking to reduce economic and social disparities within the enlarged European Union under project agreement No. CH-3-ŠMM-01/02. The investigations results were used in the project Swiss-Lithuanian Ferroelectrics: From Controlled Internal Fields to Energy Harvesting/ Medical Diagnostics/ Microelectronic Applications.

Research methodology

Operation of ultrasonic transducers was simulated by employing the finite element method using ANSYS Mechanical APDL Product Launcher software. The spatial distribution of displacements inside piezoelectric elements and matching strips was obtained. Experimental investigation was carried out with the Wayne Kerr impedance meter, the laser Doppler vibrometer Polytec OFV-5000 and the ULTRALAB (developed and produced at Professor Kazimieras Baršauskas Ultrasound Research Institute, KTU) measurement system featuring the XYZ scanner, the Bruel&Kjaer 4138 acoustic microphone with the measurement amplifier NEXUS WH 3219.

Approbation of results

In the course of the research, 7 scientific papers have been published. Five papers were published in a journal included in the database “ISI Web of Science”,

one article was published in other journals included in international databases and one paper was published in a peer-reviewed scientific journal. The main results of the work were presented in 7 international conferences. Some parts of the present work were used and reported in the Swiss-Lithuanian project in which Professor Kazimieras Baršauskas Ultrasound Research Institute participated.

Results presented for the defence

1. The monitoring method of the variations of piezoelectric properties and the domain structure of the PMN-32%PT single crystal plates of <011> cuts during the poling process was proposed and successfully implemented. The reliability of the measurement method was assessed.
2. Optical images of the crystals at different time instants demonstrated how the domain structure transforms and what piezoelectric properties of PMN-32%PT crystals develop during the poling process.
3. Due to the high electromechanical coupling factor of the transverse extension mode of PMN-32%PT single crystals, good performance of the proposed air-coupled transducers was achieved.
4. Finite element modelling and experiments showed that the performance of the developed air-coupled ultrasonic transducer is superior in comparison to air-coupled PZ-29 composite ultrasonic transducers of similar dimensions.
5. Investigation results of the acoustic fields radiated in air by the developed multi-element arrays are presented.

Structure and content of the dissertation

The present doctoral dissertation consists of the introduction, 4 chapters of the main body, conclusions and the list of references. The thesis contains 124 pages in total featuring 96 illustrations, 14 tables and 109 mathematical expressions. The list of references covers 123 items.

The introduction of the dissertation describes the relevance of the problem, the objective and tasks of the thesis, its scientific novelty and the scope of the practical application of the work, its research methodology and the approbation of results.

In the first chapter, a review of air-coupled ultrasonic transducers, PMN-PT piezoelectric properties including their vibration modes and measurement methods are presented.

In the second chapter, simultaneous monitoring of structural changes in the PMN-32%PT crystals and their piezoelectric properties during the poling process is presented.

The third chapter is devoted to the investigation of PMN-32%PT piezoelectric crystals which were used in air-coupled transducers. Two measurement methods were employed: the frequency method and the laser interferometer method. The operation of ultrasonic transducers was simulated by the finite element method using ANSYS Mechanical APDL Product Launcher software.

In the fourth chapter, description of the conducted investigation of the air-coupled ultrasonic array is given. The performance of the air-coupled transducers

and the array was estimated by analysing the frequency responses and the efficiency both theoretically and experimentally. The structure of ultrasonic fields radiated in air by the developed array is presented.

Each chapter ends with conclusions.

At the end of the thesis, conclusions of the theoretical and experimental investigations, the list of references and the list of publications on the topic of the dissertation are presented.

1. AIR-COUPLED ULTRASONIC TRANSDUCERS AND PROPERTIES OF PMN-PT PIEZOELECTRIC CRYSTALS

Air-coupled ultrasonics is a non-contact technique which has become increasingly common in non-destructive testing and material characterization. Air-coupled ultrasound has more advantages over conventional ultrasonic techniques. The primary advantage of air-coupled ultrasonics is that there is no contact with the object under investigation. For this reason, it is ideally suited for inspecting materials susceptible to interaction with or damage by water, including wood, foam, certain ceramic composites, paper and even foodstuff [2]. Ultrasonic air-coupled methods are already being used for the characterization of elastic properties of various materials, especially in the case when direct acoustic contact with the investigated material is not allowed/ possible [14].

Application of non-contact inspection ranges from the aircraft industry to the inspections in the tyre industry. Air-coupled ultrasonics is exploited for the generation and reception of Lamb waves in order to detect defects in composite materials using air as a coupling medium [15-16]. The air-coupled ultrasonic technique was shown to be very efficient and fast for the testing of large areas [17]. Airborne ultrasound is a useful non-contact method of detecting and imaging defects in aging aircraft structures, given efficient transducers for use as transmitters and receivers are available [18-19]. Modern airliners use significant amounts of composite materials reducing their weight. Composites have found increasing application in commercial aircraft structures as a result of the strength, stiffness, fatigue and corrosion resistance and weight benefits jointly contributing to the improvement of performance. Air-coupled ultrasonic techniques are used to test such structures by means of guided waves.

Application of these techniques is mainly limited by big losses of ultrasonic signals mainly due to attenuation and mismatch of acoustic impedances of ultrasonic transducers and air. There are several ways to overcome the above mentioned obstacles and to make air-coupled ultrasound efficient for the non-destructive testing industry.

1.1. Air-coupled ultrasonic transducers and arrays

During the last two decades, major progress has been achieved in the technology of air-coupled ultrasonic transduction [1]. The capabilities of several types of air-coupled transducers employing piezoceramic elements, composite piezoceramic transducers and electrostatic capacitive transducers have made significant advances [15].

Air is very compliant; thus waves from a high acoustic impedance source couple poorly into air [20]. Therefore, application of air-coupled ultrasonic measurements is problematic due to substantial acoustic transduction losses of the conventional ultrasonic air-coupled transducers [1]. The large acoustic impedance mismatch between air and most solid and liquid materials is the main limitation. The acoustic impedance of air is 0.445 kRayl at room temperature and (30 – 35) MRayl of most

piezoelectric materials. One way of reducing this mismatch is to add acoustic matching layers to the front surfaces of the transducers [11-12]. The necessity of efficient acoustic matching in order to develop successful air-coupled ultrasonic systems was recognized by many researchers [21-22]. However, in order to achieve ideal impedance matching, e.g., when maximal energy transfer via interface piezoelectric ceramic – air is obtained, materials for matching layers should possess very low acoustic impedance (0.12 MRayl). There are not so many materials with such impedance – e.g. some foams, rubber or paper. Yet, most of them are not mechanically robust. Therefore, instead of a single layer, the matching elements consisting of a few layers with different acoustic impedances have been proposed [23]. This enables the use of a richer variety of materials for matching layers.

Another way to solve this problem was the application of piezoelectric composites possessing lower acoustic impedance than monolithic piezoceramic elements. Such a feature allows to get improved impedance matching in comparison with bulk piezoceramics [1]; however, matching as a rule is obtained in a relatively narrow frequency band. The primary advantage of a piezocomposite transducer is that it is mechanically robust.

Piezoelectric membranes made of poled PVDF film are also used as air-coupled hydrophones [24].

Piezoelectric air-coupled transducers are resonant in nature and usually possess a narrow bandwidth [19]. The wider bandwidth can be achieved by adding on two quarter wave front matching layers which are made of fibreglass and silicone. In this case, the transmission coefficient increases by 12 dB [25]. Isotropic materials can be used as the matching layers. The properties of materials are the same in any direction. Conventional electrostatic air transducers and bending mode piezoelectric air transducers operating below 100 kHz have been widely used for acoustic range finders and object detectors within a wide range of distances from 0.1 to 10 m. They are denoted by the wide ultrasonic beam width [1]. Piezoceramic type air-coupled ultrasonic transducers are commercially available in both planar and focused design in the frequency range from 50 kHz to 1 MHz.

Modern microelectronic and microelectromechanical technologies were also applied for the fabrication of air-coupled ultrasonic transducers and the so-called capacitive micro-machined ultrasonic transducers (cMUT) [26]. Such transducers have been designed, modelled and fabricated by several research groups and companies during the last decade and have been used in various fields [1]. In the air environment, cMUT ultrasound transducers show good performance, especially in terms of sensitivity and bandwidth; however, the values are not as good as those of piezoelectric composite transducers. Another disadvantage of the cMUT transducers is that they are not robust and need DC voltage bias, which is sometimes inconvenient. The broadband response of the electrostatic capacitance transducers can provide additional inspection capabilities in air-coupled ultrasonic NDT [27].

The advent of novel piezoelectric materials with a very strong piezoelectric effect such as lead magnesium niobate – lead titanate [$PbMg_{1/3}Nb_{2/3}O_3$-$PbTiO_3$ (PMN-PT)] crystals enables to improve the performance of air-coupled ultrasonic

transducers [28]. The electromechanical coupling factors of such crystals for the thickness extension case is $k_{33} > 0.90$, for the transverse extension it is within the range of $k_{32} = (0.84 \sim 0.97)$ whereas for the transverse shear case it reaches $k_{15} > 0.95$ [29]. Those parameters are higher than the same parameters of most piezoelectric ceramics existing in the market and used for manufacturing ultrasonic transducers. The high electromechanical factor of the transverse extension mode should allow achieving good performance of air-coupled transducers. The application of such materials should also enable the user to reduce impedance mismatch losses leading to higher sound pressure in the air and to higher sensitivity. This may be achieved due to the lower acoustic impedance of PMN-PT elements. Our measurements presented in Chapter 2 showed that in the transverse extension mode of the PMN-32%PT piezoelectric crystals, the velocity of the ultrasonic wave is $c = 1.6$ km/s and the acoustic impedance is $Z = 13$ MRayl, which is much lower than the values of a conventional piezoelectric material.

High frequency ultrasonic transducers and arrays made of PMN-PT type elements are already being used for medical diagnostic purposes [30-31]. However, to the best of our knowledge, such piezoelectric crystals have not yet been used for low-frequency air-coupled ultrasonic transducers.

In this work, we shall investigate the application of PMN-32%PT elements for novel air-coupled ultrasonic transducers operating in the low frequency range of (30 kHz – 80 kHz). In order to select the optimal vibration modes of piezoelectric elements, detailed analysis of PMN-32%PT crystals with different cuts and poling directions will be presented. Taking into account that the piezoelectric properties of PMN-32%PT crystals may be improved by domain engineering [32], monitoring of piezoelectric properties and the domain structure of the crystals during poling, this process majorly gains in importance. We shall present the technique we have developed enabling simultaneous monitoring of the evolution of the domain structure and piezoelectric properties during the poling process.

Theoretical and experimental investigations of vibrations of PMN-32%PT piezoelectric crystals allow selecting the geometry which is most suitable for air-coupled applications. For this purpose, strip-like piezoelectric elements vibrating in the transverse extension (TE) mode were proposed. For the reduction of the transfer losses in the air, plastic matching elements in the shape of strips were developed.

Such a design of individual transducers enables to assemble them into multi-element arrays. We shall present the results of modelling of the pressure fields radiated by unfocused and electronically focused arrays and shall demonstrate the possibilities of electronic steering of ultrasonic fields in the air. The theoretical results will be validated by experiments. Such arrays significantly extend the fields of application of air-coupled techniques.

1.2. Engineered domain states for PMN-PT single crystals

Solid solutions of lead magnesium niobate – lead titanate [$PbMg_{1/3}Nb_{2/3}O_3$-$PbTiO_3$ (PMN-PT)] have already been studied for 40 years. Pure PMN is a relaxor material. PMN-PT single crystals have first been successfully grown in 1990 by

employing the Bridgman method using PbO as a flux [33-34]. These single crystals possess excellent piezoelectric properties. The electromechanical coupling factors of PMN-PT single crystals are high, for example, (0.90 – 0.96) for the transverse extension k_{3j} mode [35-36].

The superior properties of PMN-PT crystals lead to the following benefits for piezoelectric applications:

- broad bandwidth;
- high signal – noise ratio, size reduction.

There are some examples of successful application of PMN-PT crystals in the fields of acoustics and ultrasonics [27, 37]:

- medical ultrasonic imaging where [001] poling large single crystal wafers have been successfully commercialized for medical imaging purposes;
- sonars where [001] and [011] poling PMN-PT crystal elements have been successfully demonstrated for torpedo guidance and torpedo countermeasure transducers;
- accelerometers where super high mode (36 mode and 15 mode) PMN-PT single crystal elements with the highest shear charge coefficients (d_{15}>7000 pC/N) in the history of piezoelectric materials have been used;
- acoustic vector sensors where [011] poling PMN-PT crystal elements with low noise and high sensitivity have been used for 3D vector sensor array with significantly enhanced sensitivity and reduced size;
- non-destructive testing;
- hydrophones such as ocean mining-oil and gas hydrophones.

PMN-PT single crystals of various sizes and aspect ratios required for the resonant measurements are available today. Materials are also very attractive for the application in ultrasonic transducers and arrays.

Perovskite single crystals have three polar directions: <001>, <011> and <111>. Every single PMN-PT crystal has three poling directions: [001], [011] and [111]-poling.

The PMN single crystal has a trigonal structure (3m) whereas lead titanate (PT) has a tetragonal ferroelectric structure (4mm) at room temperature. Both components have a morphotropic phase boundary (MPB) between rhombohedral and tetragonal ferroelectric phases. This is the orthorhombic ferroelectric structure (mm2), in which the character of high frequency vibrations may be highly sophisticated.

The Curie temperature is in the range from 0 °C to 250 °C for PMN-PT when PT is within 0 – 50%. For the ferroelectric phase diagrams of PMN-PT, see Fig. 1.2.1 [29, 32, 38-39]. PMN and PT components undergo the phase transition to the paraelectric cubic phase at the Curie temperature. The solid and dotted black lines present the longitudinal piezoelectric coefficients in [001] and [111] ferroelectric single crystals, respectively. The arrow presents the polarization direction. Figure 1.2.1 is based on reference [39].

The crystals with domain states have various piezoelectric properties [9, 29]. Single crystals must be poled to introduce a reasonable domain structure and to improve their macroscopic piezoelectric performance.

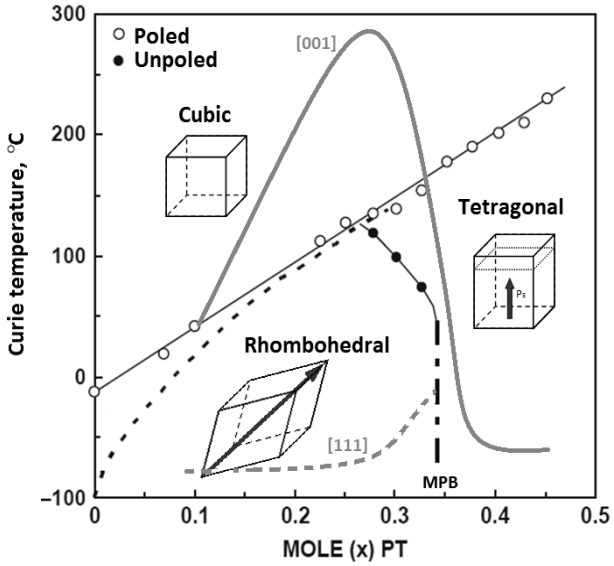

Fig. 1.2.1. Phase diagrams of PMN-PT

Piezoelectric PMN-PT crystals can be domain-engineered into three symmetric states: [001] poling direction, [011] poling direction and [111] poling direction. The domain structures in PMN-PT single crystals have been investigated by using the polarized light microscopy [38-43].

1.2.1. PMN-PT crystals with [001] poling

The PMN-PT single crystal has attracted a lot of attention because this crystal near the morphotropic phase boundary has been found to exhibit extremely high piezoelectric properties. The longitudinal extension mode (LE) with the [001] poling direction of PMN-PT single crystals possesses maximal piezoelectric constant d_{33} and electromechanical coupling coefficient k_{33} (Fig. 1.2.2, *a*). The crystals can work safely under 15kV/cm with pre-pressure to achieve strains up to 0.3% for large signal operation whereas for small signal operation, the crystals can work with d_{33} of 3000 – 3500 pC/N and $k_{33} > 0.92$, multi-domain 4mm symmetry crystals engineered by [001] poling direction. Four out of 8 possible polarizations of such crystals are shown in Fig. 1.2.2, *b* with the grey coloured or black dashed lines. Single PMN-PT crystals with the [001] poling direction domain symmetry crystal are tetragonal (4mm). They are shown in Fig. 1.2.2, *c* [44-49].

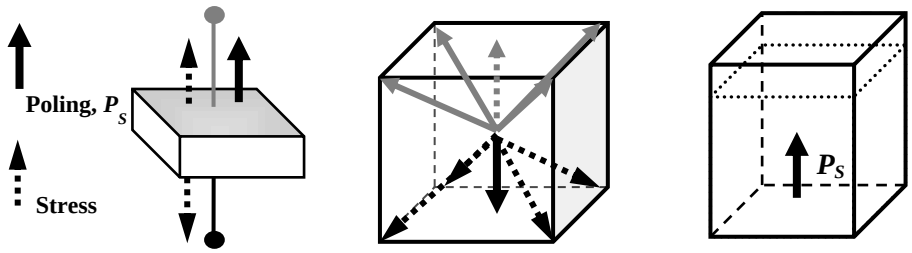

Fig. 1.2.2. PMN-PT domain-engineered crystals with [001] poling direction:
a – longitudinal extension mode; b – domain state with [001] poling direction;
c – tetragonal (4mm) ferroelectric phase

The complete matrices of elastic, piezoelectric, dielectric properties are given by equations 1.2.1, 1.2.2, and 1.2.3 [32].

Elastic coefficient matrices are presented by matrices 1.2.1:

$$c_{ij} = \begin{pmatrix} c_{11} & c_{12} & c_{13} & 0 & 0 & 0 \\ c_{12} & c_{11} & c_{13} & 0 & 0 & 0 \\ c_{13} & c_{13} & c_{33} & 0 & 0 & 0 \\ 0 & 0 & 0 & c_{44} & 0 & 0 \\ 0 & 0 & 0 & 0 & c_{44} & 0 \\ 0 & 0 & 0 & 0 & 0 & c_{66} \end{pmatrix}, \quad s_{ij} = \begin{pmatrix} s_{11} & s_{12} & s_{13} & 0 & 0 & 0 \\ s_{12} & s_{11} & s_{13} & 0 & 0 & 0 \\ s_{13} & s_{13} & s_{33} & 0 & 0 & 0 \\ 0 & 0 & 0 & s_{44} & 0 & 0 \\ 0 & 0 & 0 & 0 & s_{44} & 0 \\ 0 & 0 & 0 & 0 & 0 & s_{66} \end{pmatrix}. \quad (1.2.1)$$

Piezoelectric coefficients can be measured by employing the laser interferometer method, and the obtained matrices are the following:

$$d_{ij} = \begin{pmatrix} 0 & 0 & 0 & 0 & d_{15} & 0 \\ 0 & 0 & 0 & d_{15} & 0 & 0 \\ d_{31} & d_{31} & d_{33} & 0 & 0 & 0 \end{pmatrix}, \quad e_{ij} = \begin{pmatrix} 0 & 0 & 0 & 0 & e_{15} & 0 \\ 0 & 0 & 0 & e_{15} & 0 & 0 \\ e_{31} & e_{31} & e_{33} & 0 & 0 & 0 \end{pmatrix}. \quad (1.2.2)$$

Dielectric coefficients can be measured by the frequency method and presented by the matrix:

$$\varepsilon_{ij} = \begin{pmatrix} \varepsilon_{11} & 0 & 0 \\ 0 & \varepsilon_{11} & 0 \\ 0 & 0 & \varepsilon_{33} \end{pmatrix}. \quad (1.2.3)$$

The tetragonal (4mm) crystals class has three domain-engineered structures: 3T: [001], [010], [100]; 2T: [001], [100] and 1T: [001]. 1T is a monodomain structure [38].

1.2.2. PMN-PT crystals with [011] poling

The transverse extension (TE) mode with the [011] poling direction of PMN-PT single crystals possesses greater d_{31} values. This mode is highly anisotropic. The maximum d_{32} value occurs in the [011] direction. Piezoelectric coefficient d_{31} is negative whereas d_{32} is positive, e. g., $d_{31} = -d_{32}$ (Fig. 1.2.3, *a*).

Multi-domain mm2 symmetry crystals engineered by the [011] poling direction with two out of 8 possible polarizations are shown in Fig. 1.2.3, *b* in light and dark grey or black colours. PMN-PT crystals with [011]-poling direction domain symmetry are of orthorhombic (mm2) phase; they are shown in Fig. 1.2.3, *c* [30, 37].

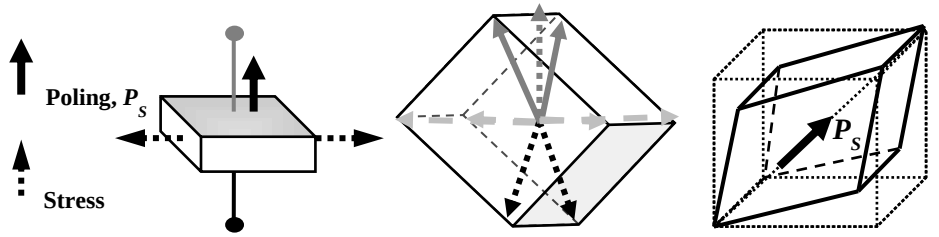

a b

c

Fig. 1.2.3. PMN-PT domain-engineered crystals with the [011] poling direction: a – transverse extension mode; b –domain state with the [011] poling direction; c – orthorhombic (mm2) ferroelectric phase

Piezoelectric constants of the PMN-PT material can be written in the form of simplified matrices by using symmetry. The complete matrices of elastic, piezoelectric, dielectric properties are given in matrices 1.2.4, 1.2.5, and 1.2.6 [32].

The elastic coefficients are given in matrices 1.2.4:

$$c_{ij} = \begin{pmatrix} c_{11} & c_{12} & c_{13} & 0 & 0 & 0 \\ c_{12} & c_{22} & c_{23} & 0 & 0 & 0 \\ c_{13} & c_{23} & c_{33} & 0 & 0 & 0 \\ 0 & 0 & 0 & c_{44} & 0 & 0 \\ 0 & 0 & 0 & 0 & c_{55} & 0 \\ 0 & 0 & 0 & 0 & 0 & c_{66} \end{pmatrix}, \quad s_{ij} = \begin{pmatrix} s_{11} & s_{12} & s_{13} & 0 & 0 & 0 \\ s_{12} & s_{22} & s_{23} & 0 & 0 & 0 \\ s_{13} & s_{23} & s_{33} & 0 & 0 & 0 \\ 0 & 0 & 0 & s_{44} & 0 & 0 \\ 0 & 0 & 0 & 0 & s_{55} & 0 \\ 0 & 0 & 0 & 0 & 0 & s_{66} \end{pmatrix}. \quad (1.2.4)$$

Piezoelectric coefficients can be measured by the laser interferometer method; they are given in the following matrices:

$$d_{ij} = \begin{pmatrix} 0 & 0 & 0 & 0 & d_{15} & 0 \\ 0 & 0 & 0 & d_{24} & 0 & 0 \\ d_{31} & d_{32} & d_{33} & 0 & 0 & 0 \end{pmatrix}, \quad e_{ij} = \begin{pmatrix} 0 & 0 & 0 & 0 & e_{15} & 0 \\ 0 & 0 & 0 & e_{24} & 0 & 0 \\ e_{31} & e_{32} & e_{33} & 0 & 0 & 0 \end{pmatrix}. \quad (1.2.5)$$

Dielectric coefficients can be measured by the frequency method; their matrix looks as follows:

$$\varepsilon_{ij} = \begin{pmatrix} \varepsilon_{11} & 0 & 0 \\ 0 & \varepsilon_{22} & 0 \\ 0 & 0 & \varepsilon_{33} \end{pmatrix}. \quad (1.2.6)$$

The orthorhombic (mm2) crystal class has three domain-engineered structures: 3O: [101], [011], [110]; 1O: [101]; 4O: [101], [011], [-101], [0-11]. 1O is a mono-domain structure [38].

1.2.3. PMN-PT crystals with the [111] poling

The transverse shear (TS) mode with the [111] poling direction of the PMN-PT single crystal possesses a super high shear piezoelectric coefficient d_{15}. This mode has a minimum cross-talk from d_{11} and d_{16} to d_{15} (Fig. 1.2.4, *a*). The single domain 3m symmetry crystals engineered by the [111] poling direction of one out of 8 possible polarizations are shown in Fig. 1.2.4, *b* in grey colour or as a black dashed line. PMN-PT crystals with the [111] poling direction domain symmetry crystals are rhombohedral (3m) (Fig. 1.2.4, *c*) [30, 37].

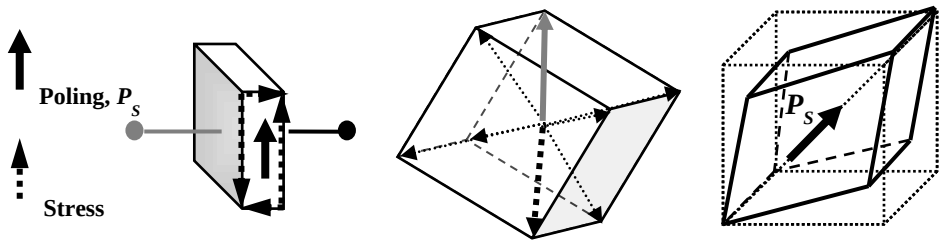

a b c

Fig. 1.2.4. PMN-PT domain-engineered crystals with the [111] poling direction: a – transverse shear mode; b – domain state with the [111] poling direction; c - rhombohedral (3m) ferroelectric phase

The rhombohedral (3m) crystal class has three domain-engineered structures: 1R: [111]; 2R: [1-11], [111]; 4R: [111], [11-1], [1-11], [1-1-1]. 1R is a mono-domain structure [38].

The complete matrices of elastic, piezoelectric and dielectric properties are given in 1.2.7, 1.2.8 and 1.2.9 matrices [32]. The elastic coefficient matrices are shown in matrices 1.2.7:

$$c_{ij}=\begin{pmatrix} c_{11} & c_{12} & c_{13} & c_{14} & 0 & 0 \\ c_{12} & c_{11} & c_{13} & -c_{14} & 0 & 0 \\ c_{13} & c_{13} & c_{33} & 0 & 0 & 0 \\ c_{14} & -c_{14} & 0 & c_{44} & 0 & 0 \\ 0 & 0 & 0 & 0 & c_{44} & c_{14} \\ 0 & 0 & 0 & 0 & c_{14} & \frac{1}{2}(c_{11}-c_{12}) \end{pmatrix}, s_{ij}=\begin{pmatrix} s_{11} & s_{12} & s_{13} & s_{14} & 0 & 0 \\ s_{12} & s_{11} & s_{13} & -s_{14} & 0 & 0 \\ s_{13} & s_{13} & s_{33} & 0 & 0 & 0 \\ s_{14} & -s_{14} & 0 & s_{44} & 0 & 0 \\ 0 & 0 & 0 & 0 & s_{44} & s_{14} \\ 0 & 0 & 0 & 0 & 2s_{14} & 2(s_{11}-s_{12}) \end{pmatrix}. \quad (1.2.7)$$

The piezoelectric coefficients can be measured by the laser interferometer method; the matrices are given in 1.2.8:

$$d_{ij}=\begin{pmatrix} 0 & 0 & 0 & 0 & d_{15} & -2d_{22} \\ -d_{22} & d_{22} & 0 & d_{15} & 0 & 0 \\ d_{31} & d_{31} & d_{33} & 0 & 0 & 0 \end{pmatrix}, e_{ij}=\begin{pmatrix} 0 & 0 & 0 & 0 & e_{15} & -e_{22} \\ -e_{22} & e_{22} & 0 & e_{15} & 0 & 0 \\ e_{31} & e_{31} & e_{33} & 0 & 0 & 0 \end{pmatrix}. \quad (1.2.8)$$

The dielectric coefficients can be measured by employing the frequency method; the matrix is given in 1.2.9 [32]:

$$\varepsilon_{ij}=\begin{pmatrix} \varepsilon_{11} & 0 & 0 \\ 0 & \varepsilon_{11} & 0 \\ 0 & 0 & \varepsilon_{33} \end{pmatrix}. \quad (1.2.9)$$

The piezoelectric, elastic and dielectric matrices of PMN-PT single crystals will be used in finite elements modelling by using ANSYS software.

1.3. Vibration modes in PMN-PT piezoelectric crystals

PMN-PT crystals with different vibration modes may be used for the development of novel high efficiency ultrasonic transducers due to their high piezoelectric properties. The piezoelectric, elastic and dielectric coefficients necessary for the development of such transducers may be determined from the appropriate measurements of the special samples, which had to be manufactured prior to the measurements. The sample dimensions must conform to European Standard EN 50324 – 1:2002 [40] and to World Standard CEI/IEC 60483:1976 [50-51]. As only a few samples are needed for the measurements, the production of such a small number of pieces would be prohibitively costly. Therefore, the plates with dimensions (15 x 15 x 1) mm^3 (HC Materials Corporation) were chosen for the manufacturing of the samples for measurements. The samples of the necessary geometry and dimensions were cut off those PMN-32%PT plates.

1.3.1. Thickness modes of plates

Only a single thickness mode is excited by an electric field in the thickness direction, and measurements in resonators vibrating in this mode are useful for

determining certain piezoelectric constants. For both thickness extensional and thickness shear modes, there are three relevant types of material constants: elastic constant, piezoelectric constant and dielectric constant [52-55].

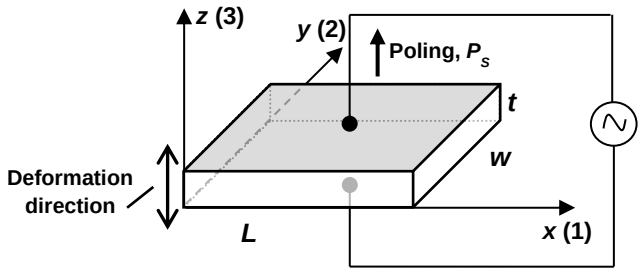

Fig. 1.3.1. A thin plate for thickness mode

What concerns c^E_{33}, c^D_{33}, k_t, ε^T_{33}, ε^S_{33}, s^E_{13}, these coefficients can be measured in *z* poling [001] direction plate as shown in Fig. 1.3.1 [56]. The sample geometry requirements are L, $w > > t$, where L is the length, w is the width and t is the thickness of the plate. The equation related to the electromechanical coupling coefficient k_t for the thickness mode in a thin plate is [52]:

$$k_t^2 = \frac{\pi}{2} \cdot \frac{f_r}{f_a} \cdot \tan\left(\frac{\pi}{2} \cdot \frac{f_a - f_r}{f_a}\right); \tag{1.3.1}$$

where f_r and f_a are the resonance and antiresonance frequencies.

The elastic stiffness constants c^E_{33}, c^D_{33} may be obtained from the following equations [57]:

$$c^D_{33} = \rho(2tf_a)^2, \tag{1.3.2}$$

$$c^E_{33} = c^D_{33}(1-k_t^2); \tag{1.3.3}$$

where ρ is the material density.

The equations for dielectric coefficients ε^T_{33}, ε^S_{33} in the plate are shown below. The entry parameters are the capacitance C_0 and the sample dimensions [58]:

$$C_0 = \frac{\varepsilon_0 \varepsilon^T_{33} A}{t}; \tag{1.3.4}$$

where $A = w \cdot L;$ (1.3.5)

Electromechanical coupling coefficient k_{33} is calculated from the measured free ε^S_{33} and clamped ε^T_{33} dielectric constants [58]:

$$k_{33}^2 = 1 - \frac{\varepsilon_{33}^S}{\varepsilon_{33}^T}. \tag{1.3.6}$$

The measurement results of the prepared PMN-32%PT samples vibrating in the thickness mode when they are poled in the [001] direction are presented in Chapter 3, in Tables 3.3.2 and 3.3.3.

1.3.2. Longitudinal Extension (LE) mode of a rod

s^E_{33}, s^D_{33} and k_{33} coefficients can be measured in *z* poling [001] direction rod as shown in Fig. 1.3.2 [56]. The sample geometry requirements are $w < \frac{L}{2.5}$.

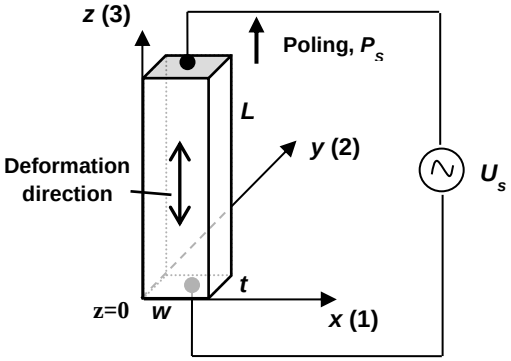

Fig. 1.3.2. The rod vibrating in the longitudinal extension mode

The entry parameters f_r and f_a measured by the electric impedance meter Wayne Kerr 6500B enable to determine elastic coefficients s^D_{33}, s^E_{33} and electromechanical coupling coefficient k_{33}:

$$s_{33}^D = \frac{1}{\rho(2lf_a)^2}, \tag{1.3.7}$$

$$k_{33}^2 = \frac{\pi}{2} \cdot \frac{f_r}{f_a} \cdot \tan\left(\frac{\pi}{2} \cdot \frac{f_a - f_r}{f_a}\right), \tag{1.3.8}$$

$$s_{33}^E = \frac{s_{33}^D}{(1 - k_{33}^2)}. \tag{1.3.9}$$

1.3.3. Transverse Extension (TE) mode of a bar

Electromechanical coupling coefficients k_{31}, k_{32} and elastic coefficient s^E_{11} can be measured in the *z* poling [011] direction of a bar as shown in Fig. 1.3.3 [56].

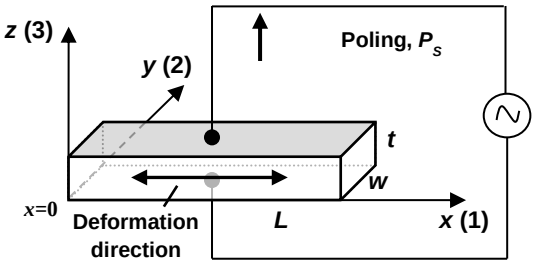

Fig. 1.3.3. The bar vibrating in the transverse extension mode

The sample geometry requirements are $t, w < \frac{L}{5}$.

The frequency f_r and f_a parameters can be measured by the impedance analyser, and electromechanical coupling coefficients k_{31} and k_{32} are calculated according to [52, 56]:

$$\frac{k_{31}^2}{1-k_{31}^2} = \frac{\pi}{2} \cdot \frac{f_a}{f_r} \cdot \tan\left(\frac{\pi}{2} \cdot \frac{f_a - f_r}{f_r}\right), \tag{1.3.10}$$

$$\frac{k_{32}^2}{1-k_{32}^2} = \frac{\pi}{2} \cdot \frac{f_a}{f_r} \cdot \tan\left(\frac{\pi}{2} \cdot \frac{f_a - f_r}{f_r}\right). \tag{1.3.11}$$

Elastic coefficients s^E_{11} and s^D_{11} are found from the expressions:

$$s_{11}^E = \frac{1}{\rho(2Lf_r)^2}, \tag{1.3.12}$$

$$s_{11}^D = s_{11}^E(1-k_{31}^2). \tag{1.3.13}$$

Piezoelectric charge coefficients d_{31} and d_{32} can be measured by employing the laser interferometer method and calculated according to [58-60]:

$$\Delta l = d_{31}U_{in} \Rightarrow d_{31} = \frac{\Delta l}{U_{in}} = \frac{S_t(nm \cdot V^{-1}) \cdot \Delta U(V)}{\frac{U(V)}{t(mm)} \cdot l(mm)}, \tag{1.3.14}$$

$$\Delta l = d_{32}U_{in} \Rightarrow d_{32} = \frac{\Delta l}{U_{in}} = \frac{S_t(nm \cdot V^{-1}) \cdot \Delta U(V)}{\frac{U(V)}{t(mm)} \cdot l(mm)}; \tag{1.3.15}$$

where Δl is the change of the bar length when the power supply is connected, ΔU is the output voltage of the interferometer, U_{in} is the power supply voltage connected to the piezoelectric element, t is the thickness of the piezoelectric element, S_t is the laser interferometer sensitivity.

Piezoelectric charge coefficients d_{31} and d_{32} can be measured by the frequency method and calculated according to [57]:

$$d_{31} = k_{31}\sqrt{\varepsilon_{33}^{T} \cdot s_{11}^{E}}, \tag{1.3.16}$$

$$d_{32} = k_{32}\sqrt{\varepsilon_{33}^{T} \cdot s_{12}^{E}}. \tag{1.3.17}$$

The equation for piezoelectric voltage coefficients g_{31} and g_{32} is given by [58]:

$$g_{31} = \frac{d_{31}}{\varepsilon_{33}^{T}}, \tag{1.3.18}$$

$$g_{32} = \frac{d_{32}}{\varepsilon_{33}^{T}}. \tag{1.3.19}$$

The equation calculations of piezoelectric modulus e_{31}, e_{32}, h_{31} and h_{32} are the following [58, 61, 62]:

$$c_{33}^{D} = \rho \cdot (2hf_a)^2, \tag{1.3.20}$$

$$e_{31} = k_{31}\sqrt{\varepsilon_{33}^{S} \cdot c_{33}^{D}}, \tag{1.3.21}$$

$$e_{32} = k_{32}\sqrt{\varepsilon_{33}^{S} \cdot c_{33}^{D}}, \tag{1.3.22}$$

$$h_{31} = \frac{e_{31}}{\varepsilon_{33}^{S}}, \tag{1.3.23}$$

$$h_{32} = \frac{e_{32}}{\varepsilon_{33}^{S}}. \tag{1.3.24}$$

Measurement and calculation results of PMN-32%PT single crystal plates with the transverse extension mode (TE) when they are poled in the [011] direction are given in Table 3.3.4.

1.3.4. Transverse Shear (TS) mode of a plate

Coefficients s^E_{44}, c^E_{44}, c^D_{44}, k_{15}, ε^S_{11}, ε^T_{11} can be measured in *z* poling [111] direction as shown in Fig. 1.3.4 [56].

The sample geometry requirements are $L > 3.5(t, w)$.

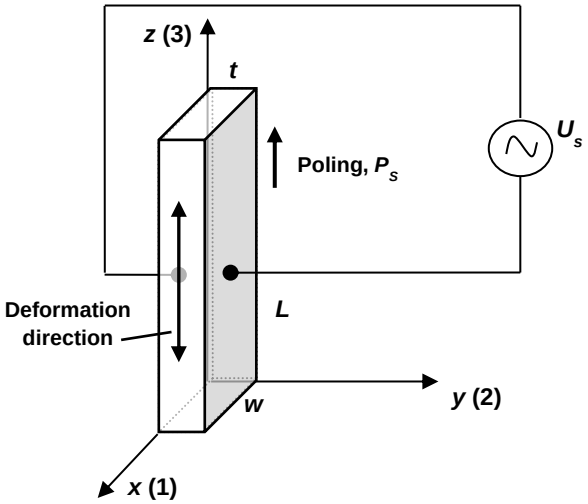

Fig. 1.3.4. The plate vibrating in the transverse shear mode

The entry parameters can be measured by the electric impedance meter Wayne Kerr 6500B. The electromechanical coupling coefficient k_{15} is calculated according to [52, 56]:

$$k_{15}^2 = \frac{\pi}{2} \cdot \frac{f_r}{f_a} \cdot \tan\left(\frac{\pi}{2} \cdot \frac{f_a - f_r}{f_a}\right). \tag{1.3.25}$$

The elastic stiffness constants c^D_{44}, c^E_{44} are obtained as:

$$c_{44}^D = \rho(2tf_a)^2, \tag{1.3.26}$$

$$c_{44}^E = c_{44}^D(1 - k_{15}^2). \tag{1.3.27}$$

Elastic coefficient s^E_{44} is calculated by using stiffness constant c^E_{44}:

$$s_{44}^E = \frac{1}{c_{44}^E}. \tag{1.3.28}$$

Elastic coefficient s^D_{55} is found from the following equation:

$$s^D_{55} = \frac{1}{4 \cdot \rho \cdot f_a^2 \cdot t^2}, \tag{1.3.29}$$

$$s^E_{55} = \frac{s^D_{55}}{1 - k^2_{15}}. \tag{1.3.30}$$

Dielectric coefficients ε^T_{11} and ε^S_{11} can be calculated from piezoelectric element capacitances C^T and C^S measured by the electric impedance meter:

$$\varepsilon^T_{11} = C^T \cdot \frac{t}{A}, \tag{1.3.31}$$

$$\varepsilon^S_{11} = C^S \cdot \frac{t}{A}. \tag{1.3.32}$$

Piezoelectric charge d_{15} coefficient is found from the relation:

$$d_{15} = k_{15}\sqrt{\varepsilon^T_{11} \cdot s^E_{55}}. \tag{1.3.33}$$

Piezoelectric voltage coefficient g_{15} is presented in [56, 58]:

$$g_{15} = \frac{d_{15}}{\varepsilon^T_{11}}. \tag{1.3.34}$$

Piezoelectric moduli e_{15} and h_{15} are obtained from the following equations [57, 58, 62]:

$$e_{15} = d_{15} \cdot c^E_{44}, \tag{1.3.35}$$

$$h_{15} = \frac{e_{15}}{\varepsilon^S_{11}}. \tag{1.3.36}$$

Measurements and calculation results of the PMN-32%PT single crystal plates with the transverse shear mode (TS) when they are poled in the [111] direction are presented in Chapter 3, Table 3.3.5.

The electromechanical coupling coefficients characterizing the piezoelectric activity of the widely used piezoelectric materials and given by manufacturers are presented in Table 1.3.1.

Table 1.3.1. Electromechanical coupling coefficients of different piezoelectric materials

	CTS 19	**PZ-21**	**PZ-23**	**PZ-27**	**PZ-29**	**PMN-28%PT (Type – A)**	**PMN-32%PT (Type – B)**
k_t	0.49	0.47	0.45	0.47	0.52	0.53	**0.54**
k_{33}	0.64	0.69	0.65	0.70	0.75	0.88	**0.92**
k_{3j}	0.28	0.323	0.288	0.327	0.37	0.65	**0.91**

From the presented review, it follows that the poled PMN-32%PT single crystal elements have outstanding piezoelectric properties. The high electromechanical factor k_{32} of transverse extension mode *y* (2) is 3.25 times better than that of the CTS 19 material or 2.5 times than that of PZ-29 material (Table 1.3.1) [29, 63].

1.4. Measurement methods of piezoelectric properties

More measuring methods are used to get the value of the piezoelectric coefficients. Piezoelectric properties common measurement approaches mostly consist of the three measuring methods which are predominantly used [64-73]:

- Frequency method;
- Laser interferometer method;
- Quasi-static method.

All the aforementioned techniques are used very frequently, mainly because they provide high accuracy results. The main disadvantages of these methods is that they require the construction of a complete set of samples, followed by the high price of the laser interferometer and the high demand for isolating the measuring centre from any parasitic vibrations. All the methods can measure the piezoelectric coefficients but there is no measurement technique enabling simultaneous monitoring of structural changes in the crystals and their piezoelectric properties during a poling process.

1.4.1. Frequency measurement method

The frequency measurement method was used for the measurements and the calculation of the material piezoelectric coefficients such as electromechanical coupling coefficients. The frequency measurement method is regularly applied as it ensures high measuring accuracy. The most regularly used type is the impedance analyser. Impedance measurements are carried out at room temperature with the impedance analyser Wayne Kerr 6500B meter (Fig. 1.4.1). The measurement error is ±0.05%; statements apply when the instrument is used under the following measurement conditions [74]:

AC Drive Level: 1V/20mA;

Speed: Slow;
Instrument fully trimmed;
Temperature range: 23±5 °C;
30 minutes warm-up period.

The disadvantage of this method is the required construction of a complete set of samples made up of a disc, a plate and the rod shape of a piezoelectric material of one rank [57, 58].

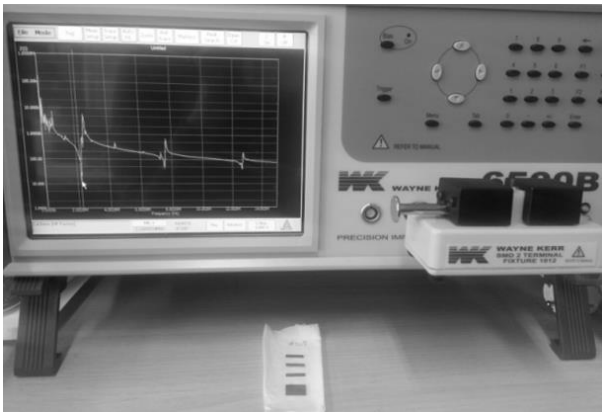

a

b

Fig. 1.4.1. a – electric impedance meter Wayne Kerr 6500B;
b – PMN-32%PT crystal bar

The impedance meter facilitates direct displaying of the impedance and phase characteristics on the device screen. The screen content can be directly saved as an image. Automatic data reading from the device can be used and processed in *Matlab* editor. The entry parameters are resonant frequency f_r, anti-resonant frequency f_a, electric input impedance Z_{IN}, and free capacitances C^T measured at low frequency 1

kHz and C^S at high frequency 2.5 MHz. The remaining properties can be calculated by making use of the relations between piezoelectric constants. The samples resonate in the 100 kHz range for transverse and length extensional modes and in 2.5 MHz range for thickness modes.

The dielectric constants at constant stress ε^T are calculated from capacitance measurements at low frequency 1 kHz and ε^S at 2.5 MHz. The piezoelectric, dielectric and elastic material properties are anisotropic and exhibit various values in different directions relative to the direction of polarization. Tensor components of the material coefficients can be written in a simplified matrix form by using symmetry. The procedure for the calculation of the coefficients is described in detail in the European and world standards [40].

1.4.2. Laser interferometer method

The second method of measuring the piezoelectric charge coefficient is the laser interferometer method. This method is based on measuring the displacement of the sample surface. The laser interferometer method has a high resolution, which should yield measurement in nanometres. The described method is most widely used under laboratory conditions. The disadvantages of this method are the high price of an interferometer and the requirements placed on the insulation of the measuring centre from any parasitic vibrations.

The devices used in this experiment can be divided into several groups: the Polytec OFV-5000 laser interferometer with the OFV-505 measuring head, the VD-09 velocity decoder with the measuring range of 1.000 mm·s/V, signal frequency range 0.5 – 1.5 MHz, the DD-300 displacement decoder with the measuring range of 0.002 mm/V at 25 kHz and the XY scanner and the signal generator AFG 3051 [75 – 78].

The principle of the heterodyne interferometer is to acquire the characteristics of mechanical vibrations or transient motion processes in the experiment. The velocity and amplitude of a vibrating object generate a frequency or phase modulation of the laser light due to the Doppler effect. A schematic layout of both signal paths is shown as a diagram in Fig.1.4.2 [79].

The light source of the vibrometer is a helium neon laser, and the wavelength is 633 nm. The optimal stand-off distances are 0 mm + ($n \cdot l$) mm, where n = 0; 1; 2… and l = 204 mm ± 1 mm for l = 204 mm; the optimal stand-off distances are: 0 mm; 204 mm; 408 mm.

The laser interferometer method is applied for the measurement of the mechanical displacement and calculated as piezoelectric charge coefficients d_{31} and d_{32}.

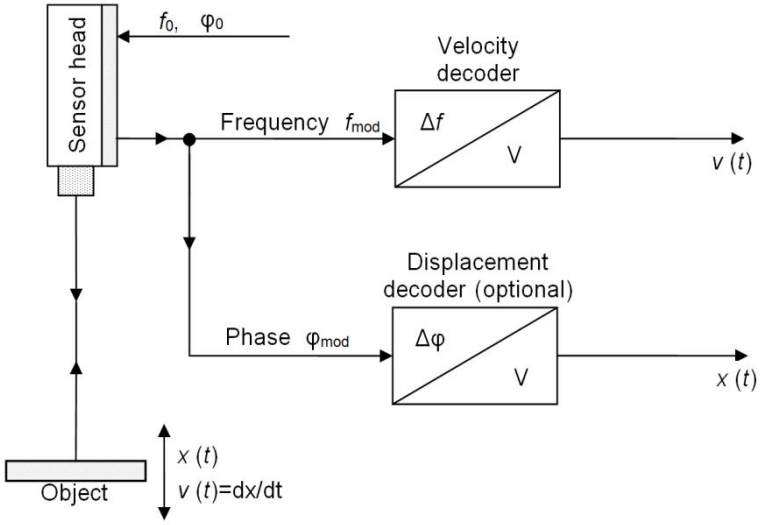

Fig. 1.4.2. Signals in the vibrometer

The experimental setup consists of the laser interferometer POLYTEC OFV-5000, the vibrometer sensor head OFV-505, XY scanner, the signal generator AFG 3051, ADC and a personal computer. The experimental setup and the measurement stand are shown in Fig. 1.4.3 and 1.4.4.

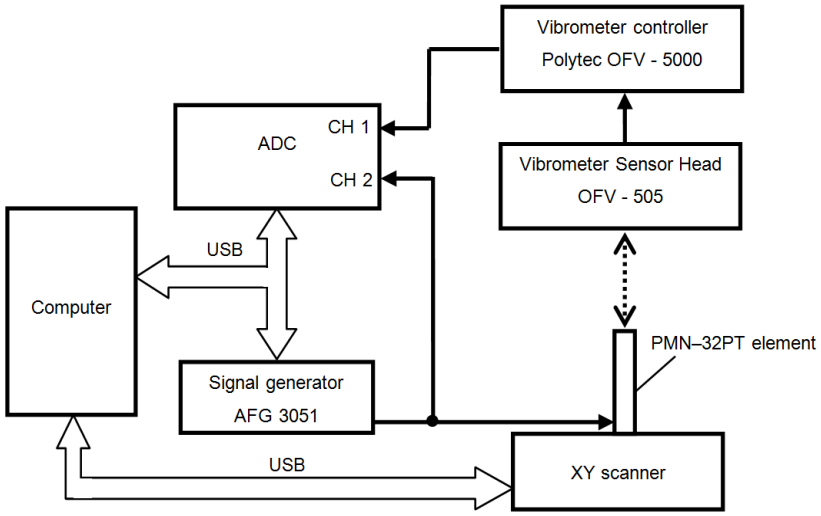

Fig. 1.4.3. The experimental setup investigation for mechanical displacements

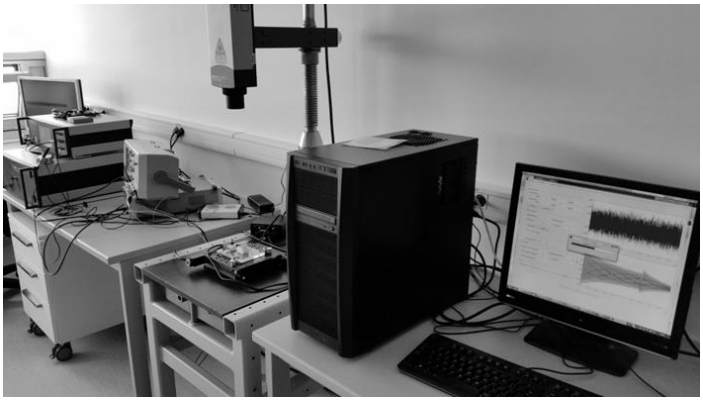

Fig. 1.4.4. The experimental stand

The disadvantage of the laser interferometry method is that any small irregularities or/and vibrations during the measurement significantly affect the accuracy of the obtained values.

1.4.3. Quasi-static method

The final method determines the piezoelectric charge coefficients through the quasi-static approach to measurement. The quasi-static method is used in "d_{31}/d_{33} meter". The devices are made by KCF Technologies (Type PM350), HC Materials Corporation (type ZJ-6B), and Sensor Technology Ltd. (type SS01-01). All the devices can measure both d_{33} and d_{31} coefficients [58].

This method is based on the direct piezoelectric effect. The piezoelectric sample is evenly loaded with force F. The charge is generated when the amount of the force on the electrodes of the piezoelectric sample changes. The value of the piezoelectric charge coefficient is then calculated from force F and voltage U. The connection scheme for the measurement of piezoelectric charge constants d_{33} and d_{31} with the quasi-static and the direct charge measuring methods is presented in Fig. 1.4.5.

Piezoelectric charge constants d_{33} and d_{31} are calculated by employing the following equations:

$$d_{33} = \frac{U_{out}}{F_3 k_q}, \tag{1.4.1}$$

$$d_{31} = \frac{U_{out}}{F_1 k_q}; \tag{1.4.2}$$

where d_{33} and d_{31} are the piezoelectric charge coefficients, U_{out} is the output voltage on the oscilloscope, F is the force on an element in the direction 33 or 31, and k_q is the charge sensitivity of the piezoelectric sample.

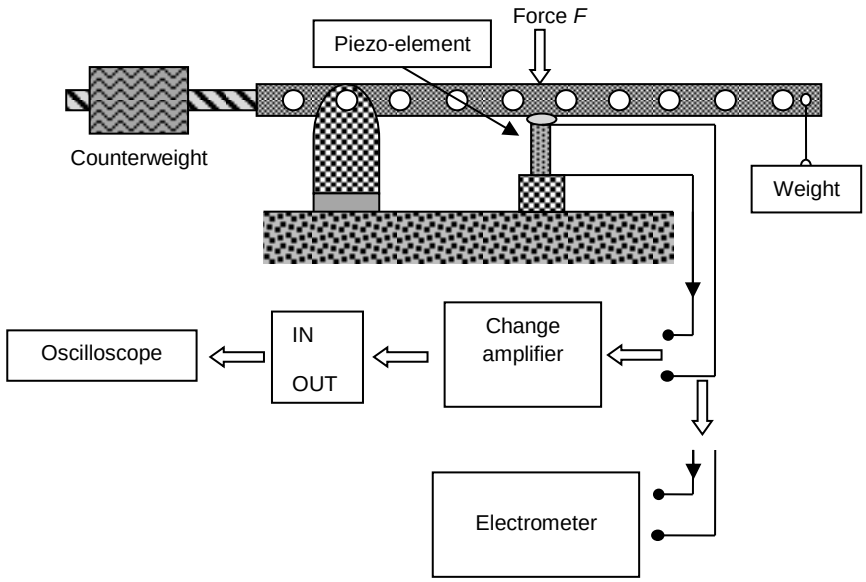

Fig. 1.4.5. The measurement setup

The use of the frequency method is advantageous when we need to measure individual coefficients of the piezoelectric material. The laser interferometry and the quasi-static methods can be applied when the piezoelectric charge is to be determined in a short time.

The advantage of the laser interferometry and the quasi-static methods as compared with the frequency method is the possibility of using piezoelectric samples which do not comply with the requirement for the minimum aspect ratio required by the European and the world standards.

1.5. Conclusions

1. Due to very high piezoelectric properties of PMN-PT crystals, they may significantly improve the performance of air-coupled ultrasonic transducers. For these purposes, the vibrations of PMN-PT rectangular plates and strips must be investigated.
2. In air-coupled ultrasonic applications, the used operation frequency is $f \leq 1$ MHz. In order to obtain such low frequencies, the main transverse extension mode of piezoelectric plates may be selected. For this mode, electromechanical coupling factor k_{32} may reach (0.84 ~ 0.97). The high electromechanical factor of the transverse extension mode allows to achieve good performance of air-coupled transducers.
3. The laser interferometry and the quasi-static methods tend to be used for checking the results obtained via the frequency method with the impedance analyser. The use of the frequency measurement method is advantageous when it is needed to establish individual coefficients or the complete matrix

of the piezoelectric material coefficients. There is no measurement technique enabling simultaneous monitoring of structural changes in the PMN-32%PT crystals and their piezoelectric properties during a poling process.

4. The piezoelectric properties of PMN-PT crystals may be further improved by domain engineering – but for that, proper measuring technique(s) enabling continuous monitoring of piezoelectric properties during the poling process of the crystals should initially be developed.

2. MONITORING OF PMN-32%PT CRYSTALS POLING PROCESS

The discovery of high piezoelectric properties for lead magnesium niobate – lead titanate (PMN - 32%PT) enables to develop ultrasonic transducers with significantly improved performance. The poled lead magnesium niobate – lead titanate (PMN-32%PT) single crystal elements are already being used in ultrasonic transducers for medical applications [80, 81]. This is due to high electromechanical coupling coefficients of the PMN-32%PT crystals which may be enhanced by using domain engineering. The domain engineering technologies could be improved by employing techniques enabling continuous monitoring of the piezoelectric properties during the poling process of single crystals at different times. Therefore, the monitoring of piezoelectric properties and the domain structure of the crystals during the poling process is of major importance [82].

2.1. Monitoring of the poling process

What concerns applications in ultrasonic transducers, especially promising are transverse extension and shear modes of PMN-32%PT crystals electromechanical coupling coefficients which may reach up to 0.90 – 0.96 [83]. Piezoelectric properties of such crystals may be further modified by domain engineering technologies. Efficiency and better physical understanding of these technologies could be improved by proper measurement techniques enabling continuous monitoring of piezoelectric properties during the poling process of the crystals which at the moment is lacking [84].

The objective of this chapter was the development and experimental verification of the measurement technique enabling simultaneous monitoring of structural changes in the PMN-32%PT crystals and their piezoelectric properties during the poling process. The method is based on optical observation of the crystal's domain structure and the simultaneous measurement of the electric impedance of the crystal versus its frequency. The monitoring and measurement are online processes. Piezoelectric coefficients such as d_{31}, d_{32}, d_{15}, e_{31}, e_{32}, e_{15} and electromechanical coupling coefficients k_{31}, k_{32}, k_{15} are calculated from the resonance – antiresonance frequency measurements [85, 86].

As an active element of air-coupled ultrasonic transducers, rectangular PMN-32%PT crystal plates with <011> cut and [011] poling vibrating in the main transverse extension mode may be used [87, 88]. Commercially available are quadratic PMN-32%PT single crystal plates which are anisotropic, e.g. piezoelectric properties in the directions of x (1) and y (2) axes are different (Fig. 2.1.1). Electromechanical coupling coefficients were determined from measured resonance f_r and antiresonance f_a frequencies of the appropriate vibration modes [89 – 92].

The PMN-32%PT single crystals used in our experiments were manufactured by "HC Materials Corporation" (USA). The PMN-32%PT single crystals were with <011> cut orientation and [011] poling direction of (10 x 10 x 0.2) mm^3 dimensions.

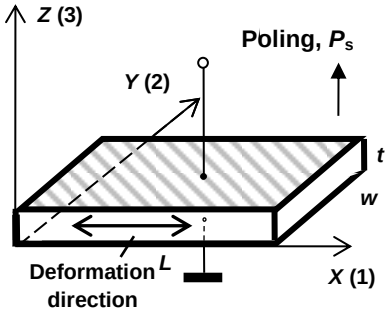

Fig. 2.1.1. Geometry of the <011> cut PMN-32%PT crystal plate

In order to get optical images of the domain structure inside the PMN-32%PT single crystal plates, the samples were coated with optically transparent electrodes based on indium tin oxide (ITO). Indium tin oxide (ITO) is a mixture of indium oxide (In_2O_3) and tin oxide (SnO_2). The sputtering target consisted of 90% In_2O_3 and 10% SnO_2 by weight [93]. The ITO layer electrodes have a resistivity of (R = 59 ÷ 105 Ω/cm) which are of similar resistivity or have lower resistivity than transparent platinum electrodes usually used in the domain engineering. The crystal was cut into 4 segments measuring (5 x 5 x 0.2) mm^3 (Fig. 2.1.2).

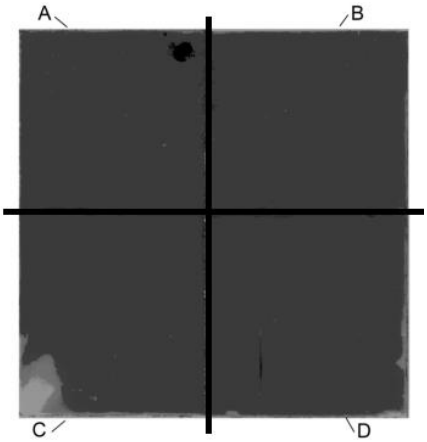

Fig. 2.1.2. The PMN-32%PT crystal: four segments with ITO electrodes

All the segments were poled while their electrical input impedance during the poling process was being monitored simultaneously. The electrical parameters of the tested crystal were measured and used for the calculation of the equivalent circuit parameters.

The poling was performed by using the high voltage power supply SRS PS350. For the measurements of electric impedance (Z_{IN}), the impedance analyser Wayne Kerr 65120B was used. The optical observation of the domain structure was

performed by using polarized light and the optical microscope Olympus SZX16 (Fig. 2.1.3).

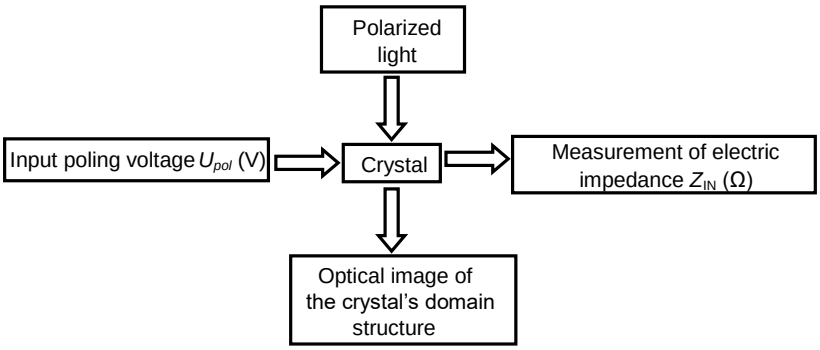

Fig. 2.1.3. PMN-32%PT single crystal poling process

The method is based on the simultaneous measurement of the input electric impedance of the crystal versus the frequency and optical observation of the crystal's domain structure. The experimental setup used for the measurement of the electrical input impedance of a PMN-32%PT single crystal during the poling process is presented in Fig. 2.1.4.

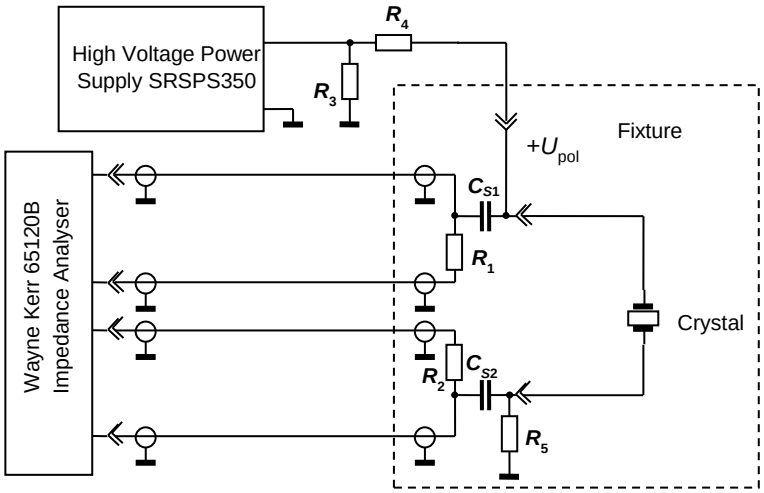

Fig. 2.1.4. Setup for the measurement of the crystal's electrical input impedance during the poling process

The Wayne Kerr impedance meter 65120B is used to measure the dependence of the input impedance Z_{IN} versus frequency within the selected frequency range and to determine resonance f_r and antiresonance f_a frequencies of the selected mode. The aim of the measurements is to calculate electromechanical coupling coefficient k_{3j} of

the measured resonance f_r and antiresonance f_a frequencies. The additional capacitors C_{S1} and C_{S2} are used to protect the input of the impedance meter from the influence of the high poling voltage U_{pol}. The high voltage power supply SRS PS350 allows precise control of poling voltage U_{pol}. The resistance of such electrodes is finite, e.g. $R_e > 0$. Additional elements of the measurement electrical circuit such as C_{S1}, C_{S2} and R_e reduce the measured electromechanical coupling coefficient. For this reason, the measurement results should be corrected in order to obtain the real values of the crystal input impedance and frequencies f_r and f_a.

2.2. Influence of additional capacitors C_{S1} and C_{S2} and resistance of electrodes

The influence of the resistances of ITO electrodes R_{e1} and R_{e2} may be evaluated for the selected vibration mode by using the simplified equivalent circuit (Fig. 2.2.1). The equivalent circuit takes into account the resistance of the ITO electrodes represented by equivalent resistors R_{e1} and R_{e2}.

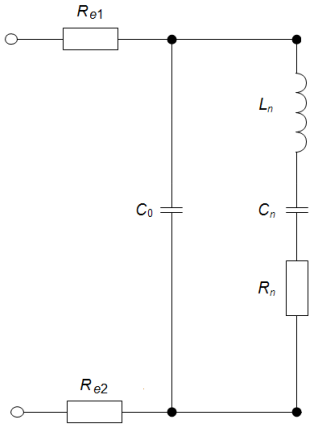

Fig. 2.2.1. The equivalent circuit of the PMN-32%PT plate with ITO electrodes

Input electrical impedance Z_{IN} taking into account resistances R_{e1} and R_{e2} of the ITO electrodes is obtained from Eq. 2.2.1 [78]:

$$Z_{IN}(\omega) = R_{e1} + R_{e2} + \frac{\dfrac{R_n}{R_n^2 + X_n^2}}{\left[\dfrac{R_n}{R_n^2 + X_n^2}\right]^2 + \left[\omega C_0 - \dfrac{X_n}{R_n^2 + X_n^2}\right]^2} - j\frac{\omega C_0 - \dfrac{X_n}{R_n^2 + X_n^2}}{\left[\dfrac{R_n}{R_n^2 + X_n^2}\right]^2 + \left[\omega C_0 - \dfrac{X_n}{R_n^2 + X_n^2}\right]^2}, \quad (2.2.1)$$

$$X_n = \omega L_n - \frac{1}{\omega C_n}; \quad (2.2.2)$$

where $\omega = 2\pi f$ is the angular frequency, resistances $R_{e1} + R_{e2} + R_n$ are measured directly by the impedance meter and index $n = 2$ is the number of the selected mode. The calculated modulus of the input electrical impedance $|Z_{IN}|$ in the vicinity of the 2nd vibration mode is presented in Fig. 2.2.2 as the dashed line. The measured input electrical impedance Z_{INm} is shown as the solid line. The measured frequencies are f_r = 240 kHz, f_a = 301 kHz, and the calculated electromechanical coupling coefficient is k_{32} = 0.67.

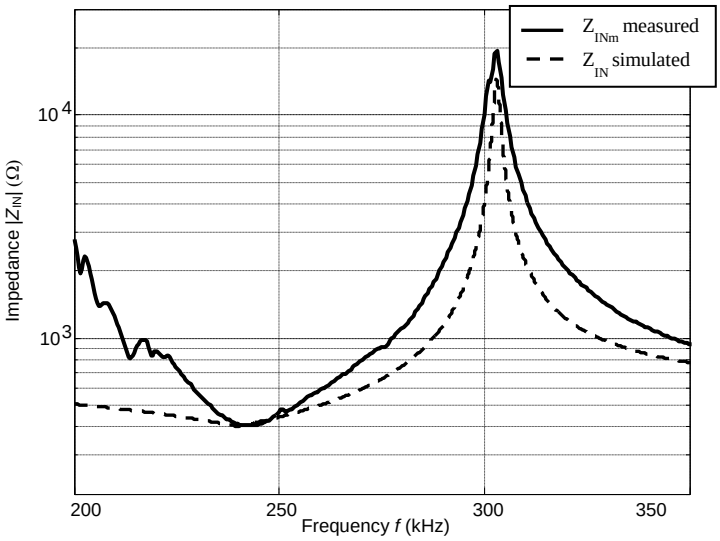

Fig. 2.2.2. The measured Z_{INm} (solid line) and simulated (dashed line) input impedances Z_{IN} of the 2nd vibration mode

Additional elements of the measurement of an electrical circuit may cause measurement errors. Therefore, the results of measurements should be corrected in order to represent the real values of the crystal input impedance. The influence of capacitors C_{S1} and C_{S2} on the measurement results may be estimated by using the equivalent circuit for one selected single mode.

Capacitors C_{S1} and C_{S2} are connected in series to the poled crystal in order to protect the input of the impedance meter from the influence of high-poling voltage U_{pol}. The advantage of the additional capacitors is their high temperature stability. The measured capacitances of the employed capacitors C_{S1} and C_{S2} were C_{S1} = 1502 pF, C_{S2} = 982 pF, and the resistance of the electrodes $R_{e1} = R_{e2}$ = 200 Ω was selected. This equivalent circuit with the additional capacitors and resistances of the electrodes is shown in Fig. 2.2.3.

In this case, the measured impedance consists of the three impedances connected serially:

$$Z_{INm} = Z_{CS1} + Z_{CS2} + Z_{IN}; \qquad (2.2.3)$$

where Z_{CS1} and Z_{CS2} are impedances of capacitances C_{S1} and C_{S2}, Z_{IN} is the electric input impedance of the crystal plate.

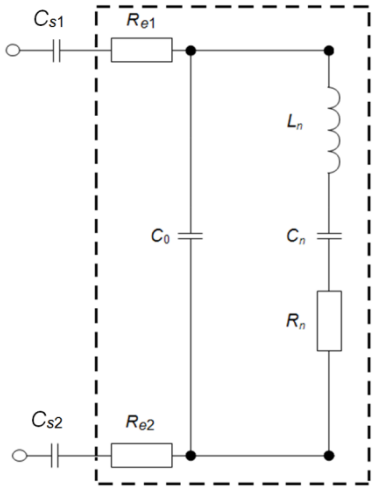

Fig. 2.2.3. The equivalent circuit of the PMN-32%PT plate (inside the rectangular box) with C_{S1} and C_{S2} additional capacitors

Additional capacitors C_{S1} and C_{S2} are connected in series. The equivalent capacitance of C_S is obtained from:

$$C_S = \frac{C_{S1}C_{S2}}{C_{S1} + C_{S2}}. \tag{2.2.4}$$

The capacitances of capacitors C_{S1} and C_{S2} were measured, and the equivalent capacitance is C_S = 584 pF. The frequency dependence of the capacitance reactance X_{CS} was used for the correction of the measured input impedance $Z^*_{IN}(j\omega)$ of the PMN-32%PT crystal:

$$Z^*_{IN}(j\omega) = Z_{INm}(j\omega) - X_{CS}(j\omega), \tag{2.2.5}$$

$$X_{CS} = \frac{1}{j\omega C_S}\ ; \tag{2.2.6}$$

where Z_{INm} is the measured input impedance of the PMN-32%PT crystal with additional capacitors C_{S1} and C_{S2}; here, $\omega = 2\pi f$ is the angular frequency. From electric input impedance Z_{INm}, frequencies f^*_r and f^*_a were determined.

The measured and the corrected frequency dependences of input impedance Z_{IN} of the <011> – cut and [011] – poled in the directions of *y* (2) of the PMN-32%PT crystal of the dimensions of (13 x 8 x 1) mm^3 are shown in Fig. 2.2.4.

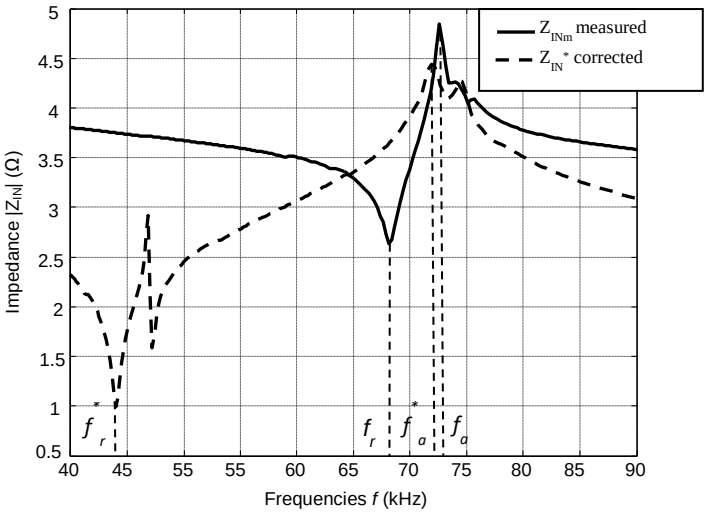

Fig. 2.2.4. Electrical input impedance Z_{INm} (solid line) measured during the poling process and corrected impedance Z_{IN}^* (dashed line); f_r^* – resonant frequency with correction; f_r – resonant frequency without correction; f_a, f_a^* – antiresonant frequency

The electromechanical coupling coefficient k_{32} was calculated according to Eq. 1.3.11 [52]. Frequencies f_r = 68.19 kHz and f_a = 72.67 kHz were measured after the polarization process. The electromechanical coupling coefficient calculated from uncorrected resonances and antiresonance frequencies is k_{32} = 0.38. The resonance frequency after correction is f^*_r = 43.91 kHz, antiresonance is f^*_a = 71.79 kHz and electromechanical coupling factor is k^*_{32} = 0.89. After the correction, the electromechanical coupling coefficient acquires a 57.05 % bigger value than the initial value without correction. Capacitors C_{S1} and C_{S2} affect the accuracy of the impedance measurements; therefore, their influence was investigated as well. The effects of capacitors C_{S1} and C_{S2} on measurement results were evaluated by using the equivalent circuit of the crystal with the <011> – cut and [011] – poled PMN-32%PT crystal of the dimensions of (15 x 15 x 1) mm^3. These crystals featuring dimensions (15 x 15 x 1) mm^3 are standard; they were manufactured by "HC Materials Corporation" (USA). First of all, the four modes were measured and calculated. The equivalent circuit is presented in Fig. 2.2.5.

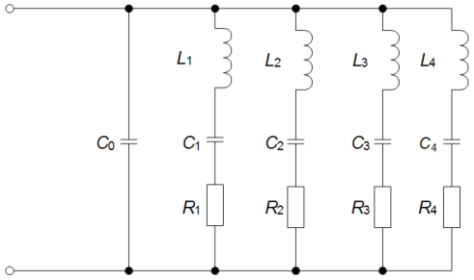

Fig. 2.2.5. The equivalent circuit of the piezoelectric element

The input electrical impedance of the equivalent circuit Z_{IN} was calculated, where the input parameters are resistance R_{IN} and reactance X_{IN} [94]:

$$Z_{IN} = R_{IN} + jX_{IN}, \tag{2.2.7}$$

$$R_{IN} = \frac{\sum_{n=1}^{m} \frac{R_n}{R_n^2 + X_n^2}}{\left[\sum_{n=1}^{m} \frac{R_n}{R_n^2 + X_n^2}\right]^2 + \left[\omega C_0 - \sum_{n=1}^{m} \frac{X_n}{R_n^2 + X_n^2}\right]^2}, \tag{2.2.8}$$

$$X_{IN} = -\frac{\omega C_0 - \sum_{n=1}^{m} \frac{X_n}{R_n^2 + X_n^2}}{\left[\sum_{n=1}^{m} \frac{R_n}{R_n^2 + X_n^2}\right]^2 + \left[\omega C_0 - \sum_{n=1}^{m} \frac{X_n}{R_n^2 + X_n^2}\right]^2}, \tag{2.2.9}$$

$$X_n = \omega L_n - \frac{1}{\omega C_n}. \tag{2.2.10}$$

Resistance R_n is measured directly by the impedance meter, and index n is the number of vibration modes represented by resonant circuits L_n, C_n and R_n.

Capacitance C_0 can be calculated by using Eq. 2.2.11 where C_{stat} is measured with the electric impedance meter Wayne Kerr B6500 at a very low frequency:

$$C_{stat} = C_0 + \sum_{n=1}^{m} C_n. \tag{2.2.11}$$

The elements of the equivalent circuit C_n and L_n were calculated according to the following formulae:

$$C_n = C_0\left[\left(\frac{\omega_a^{(n)}}{\omega_r^{(n)}}\right)^2 - 1\right], \tag{2.2.12}$$

$$L_n = \frac{1}{\left[\omega_r^{(n)}\right]^2 C_n}; \tag{2.2.13}$$

where n is the mode number, C_n is the capacitance, L_n is the inductance and R_n is the resistance.

The modelling results of the PMN-32%PT single crystal are given in Table 2.2.1.

Table 2.2.1. The modelling results of PMN-32%PT single crystal plate

Mode number n	C_n (pF)	L_n (mH)	R_n (Ω)
1	3636	5.1	10.4
2	2596	2.1	12.6
3	148.2	8.8	32.8
4	265.1	2.9	26.5
C_{stat} = 9564 pF	C_0 = 2918 pF		

The input electric impedance measured by the impedance meter in the frequency range covering a few vibration modes of the PMN-32%PT plate is presented in Fig. 2.2.6 as the solid line. The simulated input impedance is presented as the dashed line.

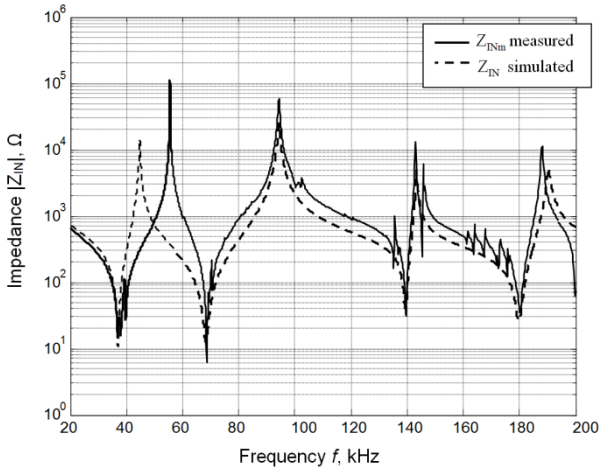

Fig. 2.2.6. Input electric impedance of the piezoelectric element (the solid line represents measurement, the dashed line depicts simulation)

From the obtained results, it follows that due to a very strong piezoelectric effect, the multimode equivalent circuit in the vicinity of the lowest fundamental modes does not describe the PMN-32%PT crystal with sufficient accuracy.

The equivalent circuit with additional capacitors C_{S1} = 1502 pF and C_{S2} =984 pF which was used in this case is shown in Fig. 2.2.7.

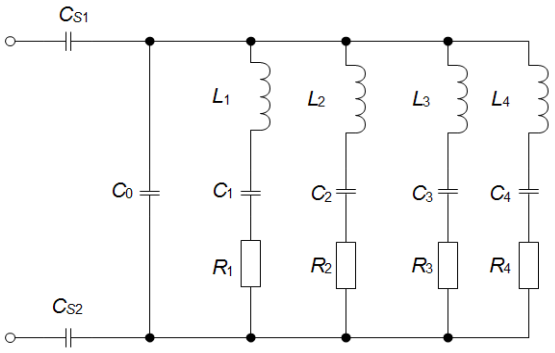

Fig. 2.2.7. The equivalent circuit of the piezoelectric element with C_{S1} and C_{S2} capacitors

The measured and calculated input electrical impedances of a few lowest modes with capacitors C_{S1} and C_{S2} are shown in Fig. 2.2.8.

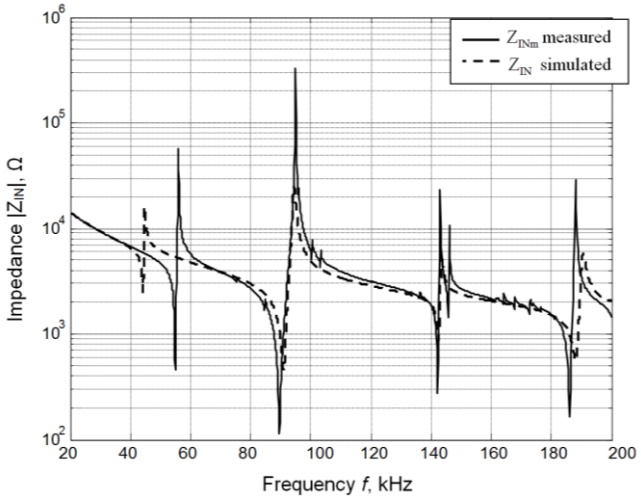

Fig. 2.2.8. Input electric impedance of the piezoelectric element with C_{S1} and C_{S2} capacitors (the solid line represents measurement, the dashed line visualizes simulation)

Additional capacitors of the measurement electrical circuit may cause measurement errors. Therefore, the influence of capacitors C_{S1} and C_{S2} on the measurement accuracy was estimated by using the equivalent circuit for one isolated mode (Fig. 2.2.9). The simulated input impedance $|Z_{IN}|$ shown in Fig. 2.2.9 as the solid line actually is without additional capacitors.

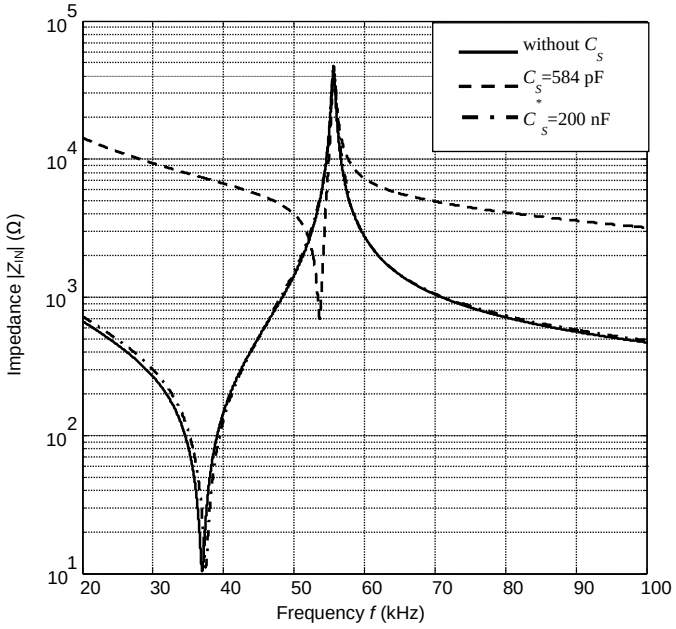

Fig. 2.2.9. Simulated input impedances $|Z_{IN}|$ taking into account only the 1st vibrational mode (the solid line provides values without C_s, the dashed line includes C_s = 584 pF, and the dot–and-dash line takes into consideration C^*_S = 200 nF)

The measured resonance frequency is f_r = 37.0 kHz whereas antiresonance frequency is f_a = 55.6 kHz, and the electromechanical coupling coefficient is k_{32} = 0.84.

Electromechanical coupling coefficient k_{32} is calculated by Eq. 2.2.14; the frequencies were measured by the impedance meter Wayne Kerr 6500B:

$$k_{32} = \sqrt{\frac{\frac{\pi}{2}\left(1+\frac{f_a - f_r}{f_r}\right)\tan\frac{\pi}{2}\frac{f_a - f_r}{f_r}}{1+\frac{\pi}{2}\left(1+\frac{f_a - f_r}{f_r}\right)\tan\frac{\pi}{2}\frac{f_a - f_r}{f_r}}}. \qquad (2.2.14)$$

When we used additional capacitors (C_s = 584 pF), the measured frequencies are f_r = 53.6 kHz and f_a = 55.6 kHz, and the obtained electromechanical coupling coefficient is only k_{32} = 0.30. The correct value of electromechanical coupling coefficient k_{32} may be obtained when the capacitances of capacitors C_{S1} and C_{S2} are the selected capacitors (C^*_S = 200 nF). Then the measured electromechanical coupling coefficient is k^*_{32} = 0.84.

Dependence of the calculated electromechanical coupling coefficient $k_{32}^*(C_S/C_0)$ on normalized equivalent capacitance C_S/C_0 is calculated according to:

$$k_{32}^*(C_S/C_0) = \sqrt{\frac{\frac{\pi}{2}(1+\frac{f_a^*-f_r^*}{f_r^*})\tan\frac{\pi}{2}\frac{f_a^*-f_r^*}{f_r^*}}{1+\frac{\pi}{2}(1+\frac{f_a^*-f_r^*}{f_r^*})\tan\frac{\pi}{2}\frac{f_a^*-f_r^*}{f_r^*}}}; \qquad (2.2.15)$$

where capacitance C_S was changed in the range from 584 pF to 200 nF. Resonance f^*_r and antiresonance f^*_a frequencies are found from minimum and maximum $|Z_{IN}|$ values with additional capacitors.

Dependence of calculated electromechanical coupling coefficient k_{32}^* versus the normalized capacitance C_S/C_0 is presented in Fig. 2.2.10.

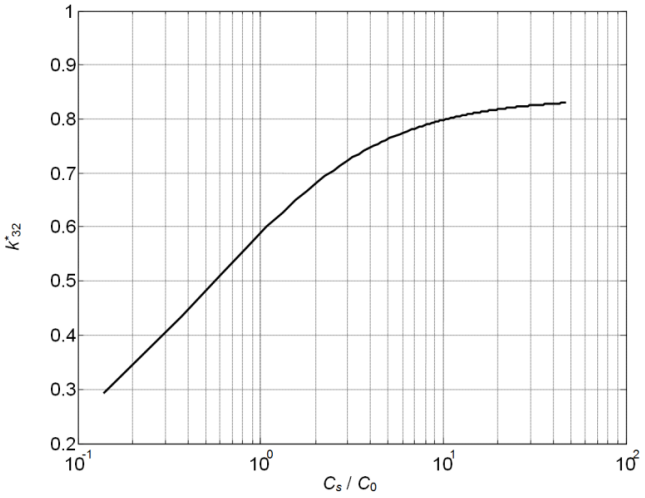

Fig. 2.2.10. Electromechanical coupling coefficient k^*_{32} versus C_S/C_0

The measurement error due to additional capacitances is obtained from:

$$\Delta k_{32}^*(C_S/C_0) = \frac{k_{32} - k_{32}^*(C_S/C_0)}{k_{32}} * 100\% . \qquad (2.2.16)$$

The dependence of the measurement error of the electromechanical coupling coefficient $\Delta k^*_{32}(C_S/C_0)$ on normalized capacitance C_S/C_0 is presented in Fig. 2.2.11.

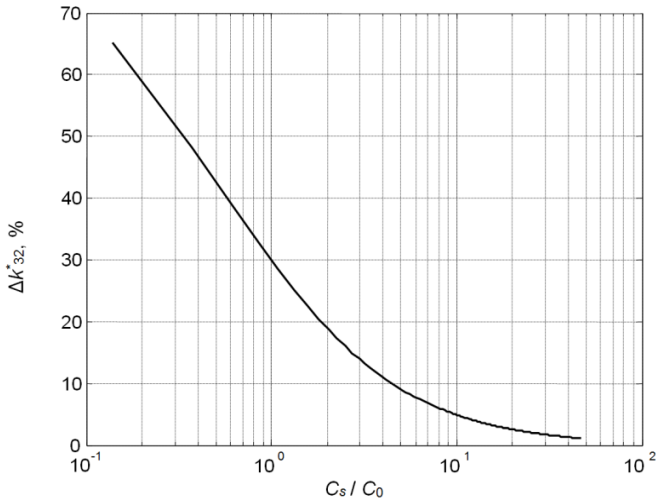

Fig. 2.2.11. Measurement error of electromechanical coupling coefficient Δk^*_{32} versus C_s/C_0

From the results presented in Fig. 2.2.11, it follows that the measurement error due to capacitors C_{S1} and C_{S2} may be significant and the values of the electromechanical coupling coefficient obtained in such a way should be corrected by using the previously described procedure.

2.3. Monitoring results of the poling process

The non-poled PMN-32%PT crystal plate with ITO transparent electrodes of the dimensions of (5 x 5 x 0.2) mm with the <011> – orientation was poled, and the impedance was measured with the Wayne Kerr 65120B impedance analyser. The optical images of crystals during the poling process were simultaneously recorded with the optical microscope's camera and transferred to a personal computer. It enables us to control the domain engineering process. Poling voltage U_{pol} was supplied by the high voltage power supply SRS PS350. The domain structure is transformed, and piezoelectric properties of the PMN-32%PT crystals are developed online during the poling process.

Variations of electromechanical coupling coefficient k_{3j} were obtained from the measured electrical input impedance at different poling voltages. The algorithm of the measurement method is presented in Fig. 2.3.1, where i is the measurement number. The PMN-32%PT crystal plate of the dimensions of (5 x 5 x 0.2) mm with the <011> – orientation is poled along the [011] – direction. The electromechanical coupling coefficient k^*_{3j} was obtained from the corrected resonance and antiresonance frequencies.

The modulus of the input electric impedance without correction $|Z_{IN}|$ versus the frequency and optical images of the crystal's domain structure at different time instants of the poling process is shown in Fig. 2.3.2.

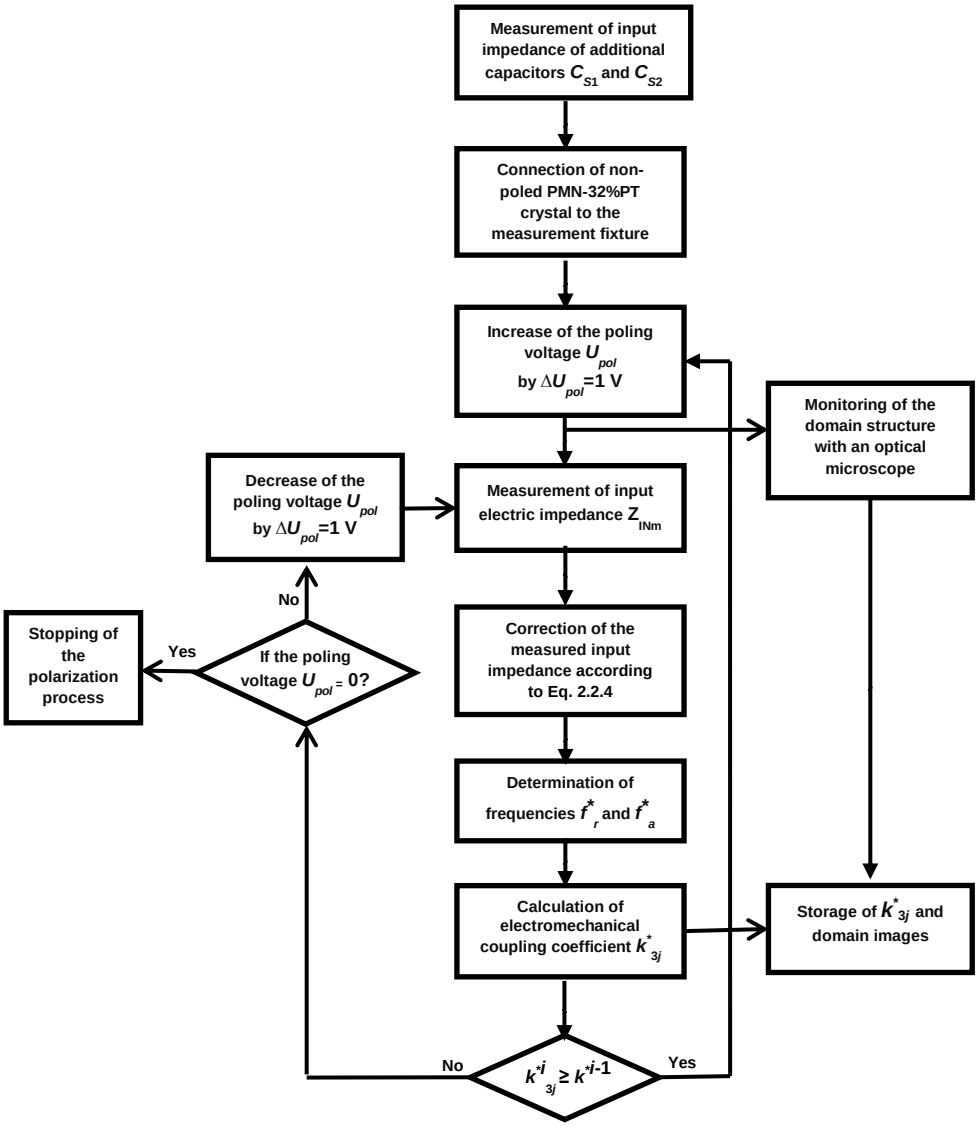

Fig. 2.3.1. The algorithm of the measurement method

First of all, poling voltage U_{pol} was set at 0 V (recorded the signal) and increased by ΔU_{pol} = 1 V until the domain structure started to change its structure (Fig. 2.3.2, *a*). It enabled the start of the polarization process. Every time, the signals were recorded. Poling voltage U_{pol} was stopped and was not altered anymore; the monitoring of the optical images of the crystal's domain structure at the different time instants are presented in Fig. 2.3.2 *b*, *c*, and *d*. They clearly demonstrate how the domain structure and the piezoelectric properties transform the crystal during the poling process. The next important step, the correction of the measured electric input impedance and the calculation of the electromechanical coupling coefficient

was then performed. When electric input impedance $|Z_{IN}|$ did not change anymore, poling voltage U_{pol} was increased by ΔU_{pol} = 1 V until the electromechanical coupling coefficient became equal to $k^{*}i_{3j} \geq k^{*i-1}$. Then, the poling voltage was decreased by ΔU_{pol} = 1 V until the starting position U_{pol} = 0 V (Fig. 2.3.2, *f*).

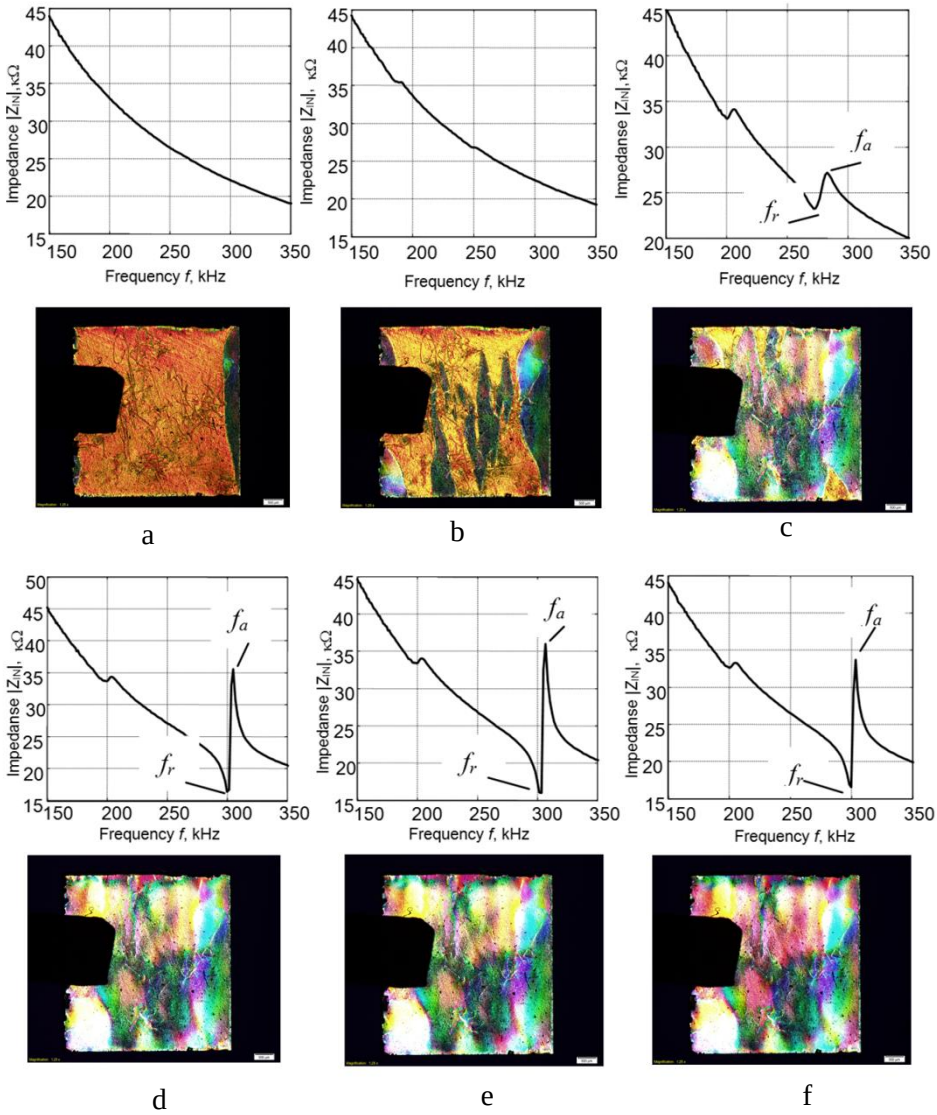

Fig. 2.3.2. Dependence of the input electrical impedance and domain structure on the poling voltage at different instances of time: a – U_{pol} = 44 V, Δt = 0 min; b – U_{pol} = 44 V, Δt = 2 min; c – U_{pol} = 44 V, Δt = 6 min (f_r = 271.8 kHz, f_a = 283.0 kHz); d – U_{pol} = 44 V, Δt = 8 min (f_r = 299.8 kHz, f_a = 305.0 kHz); e – U_{pol} = 50 V, Δt = 0 min (f_r = 303.3 kHz, f_a = 306.8 kHz); f – U_{pol} = 0 V, Δt = 0 min (f_r = 299.8 kHz, f_a = 303.3 kHz)

The poling process demonstrates how the domain structure transforms and how the piezoelectric properties of the PMN-32%PT crystals develop during the poling process.

From the experiments, it follows that charged domain walls are not allowed in regular ferroelectric materials. The reason of the existence of charged walls in PMN-32%PT single crystals is the presence of a large amount of charged defects. These charged defects stabilize the charged walls. The change of neutrality may also be accomplished through the injection of free charges into the walls during the poling process.

Electromechanical coupling coefficient k^*_{31} was calculated from corrected frequencies f^*_r and f^*_a by employing Eq. 2.2.4. The dependency of electromechanical coupling coefficient k^*_{31} versus poling voltage U_{pol} is presented in Fig. 2.3.3.

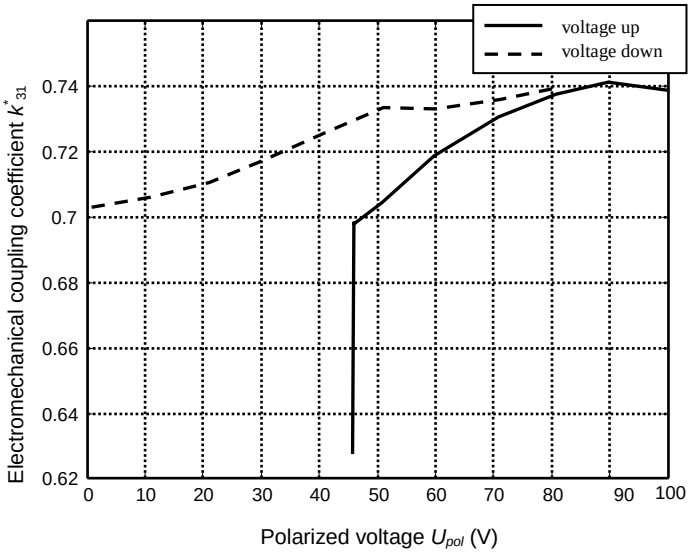

Fig. 2.3.3. The dependency of electromechanical coupling coefficient k^*_{31} versus poling voltage U_{pol}: the solid line represents voltage going up; the dashed line shows voltage going down

It is essential to note that electromechanical coupling coefficient k_{31} presented in Fig. 2.3.2 – 2.3.3 is in x (1) direction.

2.4. Metrological evaluation of the measurement method

The case of interest is where quantity Y is actually measured or virtually measured (i.e. it is not measured directly but is indirectly determined from N of other quantities X_1, X_2, X_3, . . , X_N through functional relation f which is also frequently referred to as the measurement equation:

$$Y = f(X_1, X_2, X_3, ...X_N). \quad (2.4.1)$$

Included among quantities X_i are the corrections (or correction factors) as well as quantities taking into account other sources of variability, such as different observers, instruments, samples, laboratories, and times at which the observations were made (e.g. different days). Thus function *f* of Equation (2.2.15) should express not simply a physical law but a measurement process, and, in particular, it should contain all the quantities which can potentially contribute significant uncertainty to the measurement result. An estimate of measured or output quantity *Y* denoted by *y* is obtained from Equation (2.2.15) by using input estimates x_1, x_2, x_3, . . , x_N for the values of *N* input quantities X_1, X_2, X_3, . . , X_N. Thus output estimate *y* which actually is the result of the measurement is given by [95]:

$$y = f(x_1, x_2, x_3, ...x_N). \tag{2.4.2}$$

This procedure covers the evaluation of uncertainty in the investigation of electromechanical coupling coefficient k_{32} and additional capacitors C_{S1} and C_{S2}.

Measurement uncertainty of the electromechanical coupling factor

Measurement uncertainty of the electromechanical coupling factor stems from uncertainties of the measurements of environmental temperature *u* (*T*), the elements of measurement stand, for example, capacity between the cables, inductance cables. In this case, we investigated the PMN-32%PT crystals in low frequency > 1 MHz, and the measurement components are not evaluated at all. The measurement uncertainty of the electromechanical coupling factor is mainly due to uncertainties of the measurements of frequencies and the capacities of the correction capacitances.

As it has been noted before, additional capacitors C_{S1} and C_{S2} of the measurement electrical circuit may cause measurement errors. Therefore, the results of measurements should be corrected in order to have the real values of crystal input impedance Z_{IN} and the corresponding resonance f_r and antiresonance f_a frequencies. The frequency dependence of capacitance reactance X_{CS} was used for the correction of measured input impedance $Z^*_{IN}(j\omega)$ of the PMN-32%PT crystal (Eq. 2.2.6).

The additional capacitors are connected in series. The capacitances of capacitors C_{S1} and C_{S2} were measured, and the equivalent capacitance is C_S = 584 pF. The equivalent capacitance of C_S is obtained from Eq. 2.2.4. The measurement error of the impedance meter Wayne Kerr is ±0.05%.

The standard uncertainty of the additional capacitors is *u* (C_S); it is calculated according to the following formulae:

$$S(C_S) = \sqrt{\frac{1}{n(n-1)}\sum_{i=1}^{n}(C_S^i)}, \tag{2.4.3}$$

$$u(C_S) = S(C_S); \tag{2.4.4}$$

where $i = 1 \ldots n$; here, *n* is the number of measurements. The standard measurement uncertainty of additional capacitors is *u* (C_S) = 584 ± 2.92 pF (0.5 %).

The corrected frequency dependences of input impedance Z_{IN} of the <011> – cut and [011] – poled in the directions of y (2) of the PMN-32%PT crystal possessing the dimensions of (13 x 8 x 1) mm^3 are shown in Fig. 2.4.1. From the electric input impedance Z_{IN}, frequencies f^*_r and f^*_a were determined.

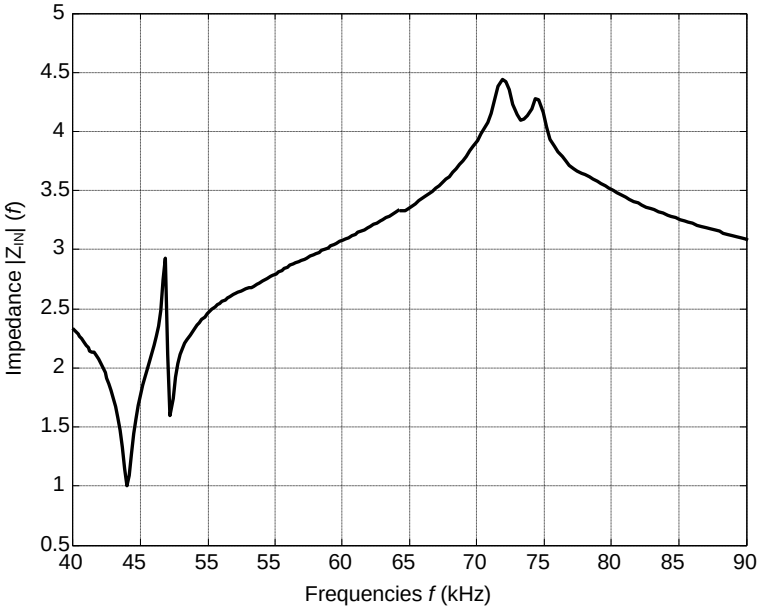

Fig. 2.4.1. Corrected electrical input impedance Z_{IN}

Frequencies f^*_r and f^*_a are obtained by using the derivative of corrected input impedance $Z_{IN}(f)$, e.g.

$$F_Z(f) = \frac{dZ_{IN}[\Omega]}{df[\mathrm{Hz}]}; \qquad (2.4.5)$$

where Z_{IN} is the measured input impedance of the PMN-32%PT crystal with additional capacitors C_{S1} and C_{S2}.

This function is presented in Fig. 2.4.2, *a*. The steps between the neighbouring measurement points in frequency domain Δf_r and Δf_a are defined with the impedance meter Wayne Kerr and vary between Δf_r = 164.5 Hz and Δf_a = 269 Hz. In order to achieve higher accuracy of frequencies f^*_r and f^*_a measurements, we are using linear interpolation between the adjacent points. The aim of interpolation is to get more data points. The interpolation step is 1 Hz. Resonance f^*_r and antiresonance f^*_a frequencies are discovered as the interpolation curve intersects with the selected threshold. The threshold of $0.2 \cdot 10^{-3}$ [Ω/Hz] was used.

The resonance frequency measured after the correction is f^*_r = 43.9127 kHz (Fig. 2.4.2, *b*), the antiresonance is f^*_a = 71.7917 kHz (Fig. 2.4.2, *c*). The electromechanical coupling factor after the correction procedure is calculated by employing Eq. 2.2.15. The electromechanical coupling factor is k^*_{32} = 0.89. The

correction of the electromechanical coupling coefficient gives a 57.05% bigger value than the value obtained without correction.

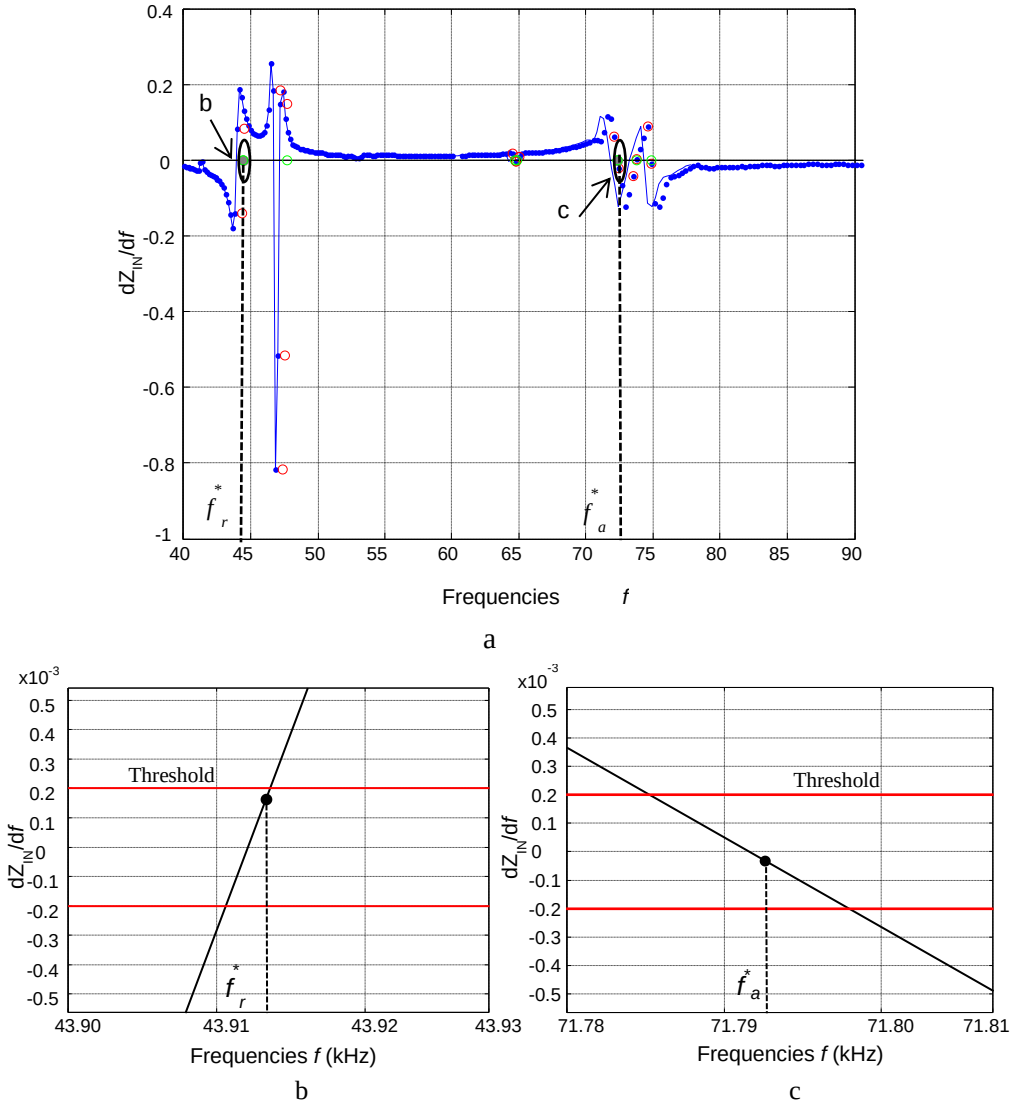

Fig. 2.4.2. a – the function of the frequency derivation; b – the zoom zone of the resonance frequency f^*_r; c – the zoom zone of the antiresonance frequency f^*_a

The standard uncertainty of the electromechanical coupling factor will be discovered by using the random number generator in the *Matlab* software. This function generates uniformly distributed random numbers in the interval (0, 1). In general, we generate n random numbers in the intervals (Δf_{r1}, Δf_{r2}), (Δf_{a1}, Δf_{a2}), and the frequencies are calculated according to:

$$r_r = \Delta f_{r1} + (\Delta f_{r2} - \Delta f_{r1})\text{rand}(n,1), \quad (2.4.6)$$

$$r_a = \Delta f_{a1} + (\Delta f_{a2} - \Delta f_{a1})\text{rand}(n,1); \quad (2.4.7)$$

where n is the numbers of modelled measurement, Δf_{r1}, Δf_{r2} or Δf_{a1}, Δf_{a2} are the intervals between the measurements points (shown in red colour), in which n random numbers are generated. The numbers of modelled measurement is 1000. The intervals of frequencies are shown in Fig. 2.4.3.

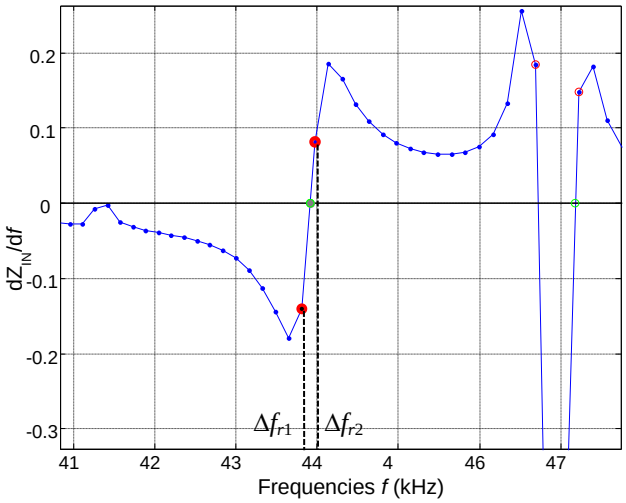

a

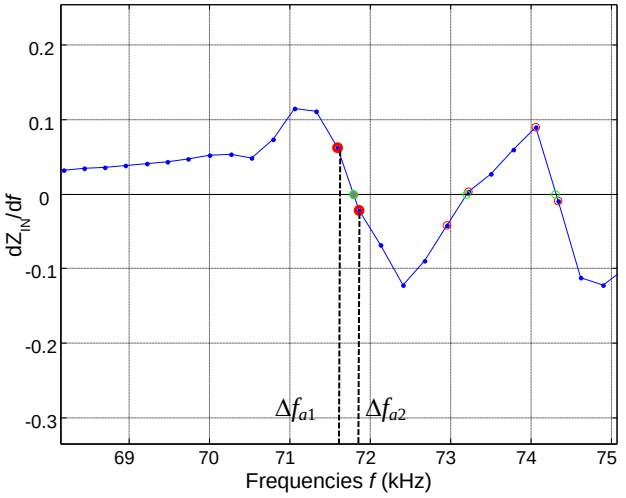

b

Fig. 2.4.3. a – resonance frequency (Δf_{r1}, Δf_{r2}) interval;
b – antiresonance frequency (Δf_{a1}, Δf_{a2}) interval

The distribution of simulated resonance Δf_r=164.5 Hz (Fig. 2.4.4, *a*) and antiresonance Δf_a=269 Hz (Fig. 2.4.4, *b*) frequencies versus the numbers of modelled measurement *i* is presented in Fig. 2.4.4.

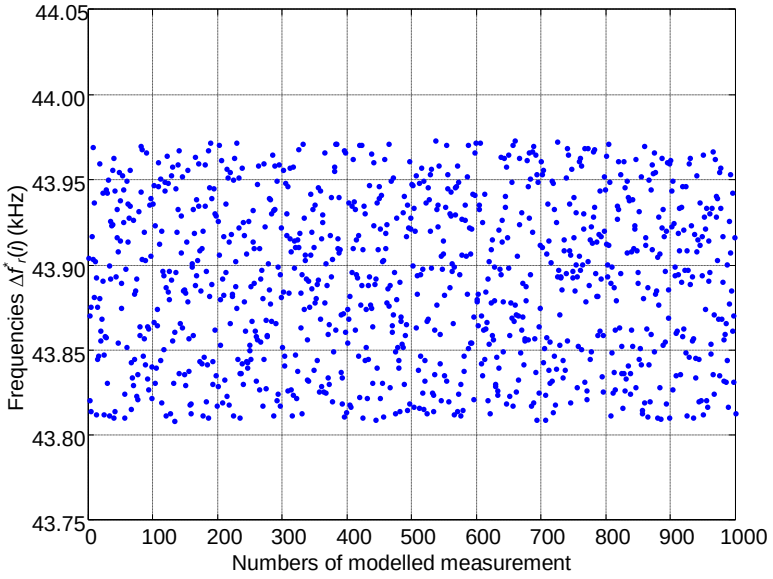

a

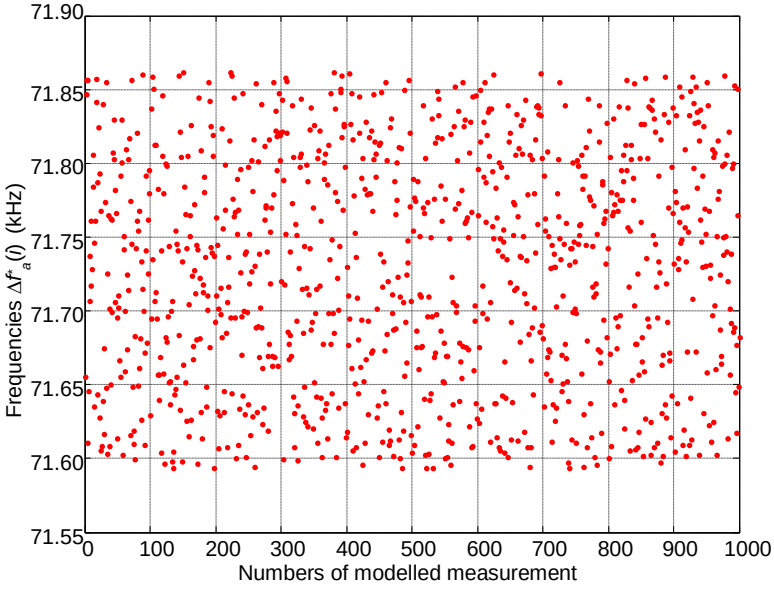

b

Fig. 2.4.4. Distribution of simulated resonance Δf_r=164.5 Hz (a) and antiresonance Δf_a=269 Hz (b); frequencies versus the numbers of modelled measurement

The electromechanical coupling factor was calculated by using simulated random resonance frequencies $\Delta f^*_r(i)$ and antiresonance frequencies $\Delta f^*_a(i)$ in the sampling frequencies interval:

$$k^*_{32}(i) = \sqrt{\frac{\frac{\pi}{2}(1+\frac{\Delta f^*_a(i)-\Delta f^*_r(i)}{\Delta f^*_r(i)})\tan\frac{\pi}{2}\frac{\Delta f^*_a(i)-\Delta f^*_r(i)}{\Delta f^*_r(i)}}{1+\frac{\pi}{2}(1+\frac{\Delta f^*_a(i)-\Delta f^*_r(i)}{\Delta f^*_r(i)})\tan\frac{\pi}{2}\frac{\Delta f^*_a(i)-\Delta f^*_r(i)}{\Delta f^*_r(i)}}}. \qquad (2.4.8)$$

The electromechanical coupling factor $k^*_{32}(i)$ versus the numbers of modelled measurement is presented in Fig. 2.4.5. The red line corresponds to the value of the measured electromechanical coupling factor, specifically, $k^*_{32} = 0.89$. The standard uncertainty of the electromechanical coupling factor is $u(k^*_{32})$, which is calculated according to:

$$S(k^*_{32}) = \sqrt{\frac{1}{n(n-1)}\sum_{i=1}^{n}(k^*_{32}(i))}\,, \qquad (2.4.9)$$

$$u(k^*_{32}) = S(k^*_{32})\,. \qquad (2.4.10)$$

The standard uncertainty of the electromechanical coupling factor is $u(k^*_{32}) = 0.89 \pm 0.0021$ (0.24%).

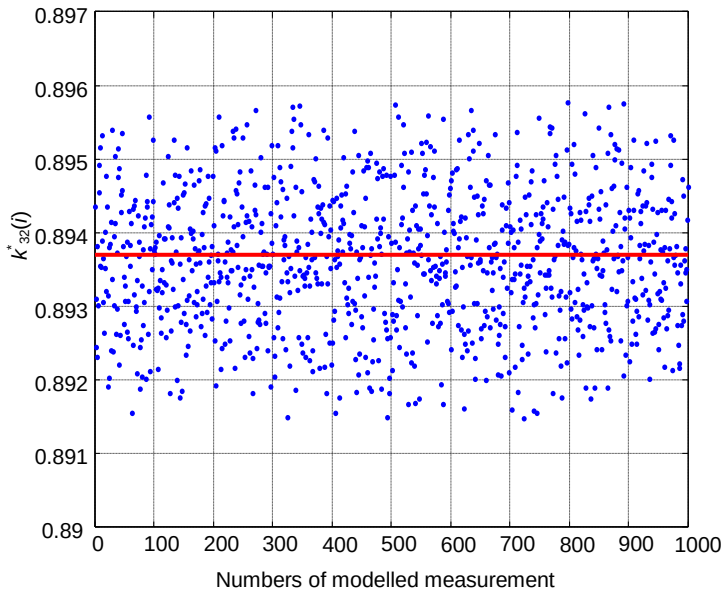

Fig. 2.4.5. The electromechanical coupling factor $k^*_{32}(i)$ versus the numbers of modelled measurement

The combined calculation of the uncertainty of electromechanical coupling coefficient k_{32} taking into account the influence of C_{S1} and C_{S2} capacitors and the uncertainty of frequency measurements is performed. If there is no correlate input of estimates and when influence factors are W_Q=W_S=W_T=W_D=1, the combined uncertainty of the input values is calculated according to:

$$u_{\sum k32} = \sqrt{u(k_{32}^*)^2 + u(C_S)^2}\ ; \tag{2.4.11}$$

where $u(k^*_{32})$ and $u(C_S)$ are standard uncertainties of type *B*.

The combined uncertainty is $u_{\sum k32}$ = 0.55%. The expanded measurement uncertainty U_k is obtained from:

$$U_k = k_r u_{\sum k}\,, \tag{2.4.12}$$

where coverage factor is k_r = 2. It is a case of normal distribution. The probability density function is presented in Fig. 2.4.6.

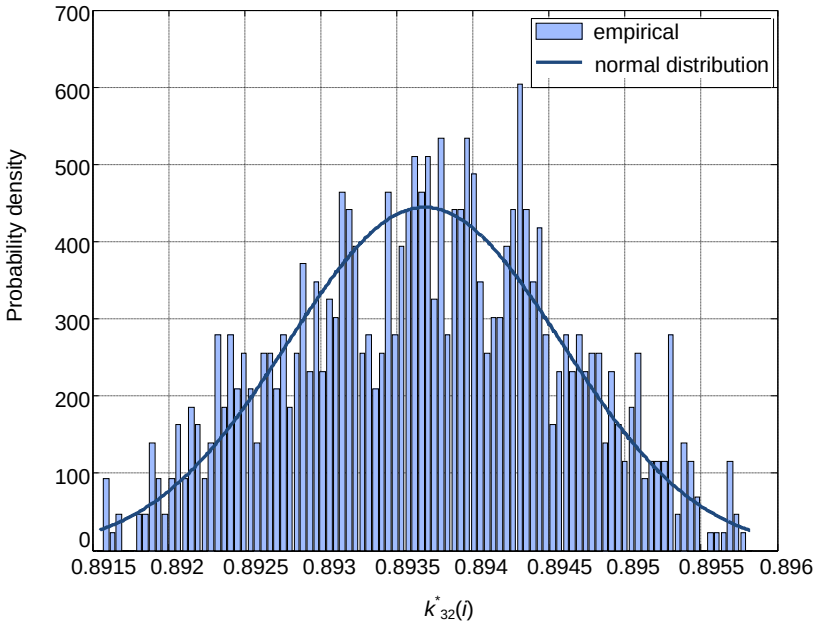

Fig. 2.4.6. The probability density

Then, the expanded measurement uncertainty is U_k = 1.1%.

2.5. Conclusions

1. Electromechanical coupling coefficients of the PMN-32%PT crystals can be enhanced by using domain engineering.

2. For the monitoring of piezoelectric properties and structural changes during the poling process, an innovative method was proposed which is based on the optical observation of the crystal's domain structure by using polarized light and employing simultaneous measurement of the electric impedance of the crystal versus its frequency.
3. Additional elements of the measurement of the electrical circuit may cause measurement errors. Therefore, the results of the measurements have been corrected in order to obtain the real values of the crystal input impedance. The standard uncertainty of additional capacitors is u (C_S) = ±0.5%. The standard uncertainty of the electromechanical coupling coefficient is u (k^*_{32}) = ±0.24%. The expanded measurement uncertainty is U_k = 1.1%.

3. INVESTIGATION OF AIR-COUPLED TRANSDUCER WITH PMN-32%PT PIEZOELECTRIC ELEMENTS

Ultrasonic transducers are widely used for detection, characterization and measurements. For air-coupled applications, usually relatively low frequencies in the range of ($f \leq 1$ MHz) are used. In order to obtain such frequencies, PMN-32%PT crystals of <011> cut and [011] poling direction with the dimensions of (15 x 15 x 1.0) mm^3 operating in the transverse extension mode were selected. When designing piezoelectric ultrasonic transducers and arrays, it is essential to consider the catalogue values of the consumed material. The most common measurement approaches consist of the following three methods:

- Frequency method;
- Laser interferometer method;
- Ultrasonic fields in air.

The Finite Element Model (FEM) of the piezoelectric transducer was performed by using the ANSYS finite element code. In this chapter, the influence of electric input impedances and mechanical as well as geometrical characteristics of the matching layers are examined.

3.1. Finite Element Model (FEM) by the ANSYS

3D finite element modelling was performed in order to achieve better understanding of the spatial distributions of mechanical displacements in PMN-32% PT crystal elements. Before proceeding to conversion routines, the basic constitutive relationship of piezoelectric materials will be outlined. The stress, strain and electric displacement vectors are presented in the following form [96, 97]:

$$\{S\} = [s^E]\{T\} + [d]\{E\}, \tag{3.1.1}$$

$$\{D\} = [d]^t\{T\} + [\varepsilon^T]\{E\}, \tag{3.1.2}$$

$$\{T\} = [c^E]\{S\} - [e]\{E\}; \tag{3.1.3}$$

where $\{T\}$ is the stress vector consisting of six components (x, y, z, yz, xz, xy), $\{S\}$ is the strain vector consisting of six components (x, y, z, yz, xz, xy), $\{D\}$ is the electric displacement vector consisting of three components (x, y, z), $\{E\}$ is the electric field vector consisting of three components (x, y, z), $[s^E]$ is the compliance matrix evaluated at the constant electric field, $[d]$ is the piezoelectric matrix relating to the strain/electric field, $[d]^t$ is the piezoelectric matrix relating to the strain/electric field (transposed), $[\varepsilon^T]$ is the dielectric matrix evaluated at constant stress, $[c^E]$ is the stiffness matrix evaluated at the constant electric field, $[e]$ is the piezoelectric matrix relating to the stress/electric field.

There are several ways in which a user can input the stress – strain data [98]. Assuming that polarization is shown in the 3rd (z) axis, one can manufacture data to ANSYS data resulting in the generation of a compliance matrix:

$$\left[s^E\right]=\left[c^E\right]^{-1}=\begin{pmatrix} s_{11}^E & s_{12}^E & s_{13}^E & 0 & 0 & 0 \\ & s_{22}^E & s_{23}^E & 0 & 0 & 0 \\ & & s_{33}^E & 0 & 0 & 0 \\ & & & s_{44}^E & 0 & 0 \\ & & & & s_{55}^E & 0 \\ & & & & & s_{66}^E \end{pmatrix}. \tag{3.1.4}$$

As noted in Equation 3.1.5, one can calculate the dielectric constants based on the constant strain from the following relationship:

$$\left[\varepsilon^S\right]=\left[\varepsilon^T\right]-\left[d\right]^t\left[s^E\right]^{-1}\left[d\right]. \tag{3.1.5}$$

The permittivity matrix has only diagonal terms:

$$\left[\varepsilon^S\right]=\begin{pmatrix} \varepsilon_{11}^S & 0 & 0 \\ & \varepsilon_{22}^S & 0 \\ & & \varepsilon_{33}^S \end{pmatrix}=\varepsilon_0\begin{bmatrix} K_{11}^S & 0 & 0 \\ & K_{22}^S & 0 \\ & & K_{33}^S \end{bmatrix}; \tag{3.1.6}$$

where $K_{11}^S=\dfrac{\varepsilon_{11}^S}{\varepsilon_0}$ is the relative permittivity. Usually, the manufacturer-provided data contains [d] relating the mechanical strain to the electric field. Meanwhile, ANSYS requires [e] relating the mechanical stress to the electric field; thus conversion is necessary. The relationship between [e] and [d] is established as follows:

$$\left[e\right]=\left[s^E\right]^{-1}\left[d\right]=\left[d\right]^t\left[s^E\right]^{-1}, \tag{3.1.7}$$

$$\left[d\right]^t=\begin{pmatrix} 0 & 0 & 0 & 0 & d_{15} & 0 \\ 0 & 0 & 0 & d_{24} & 0 & 0 \\ d_{31} & d_{32} & d_{33} & 0 & 0 & 0 \end{pmatrix}. \tag{3.1.8}$$

The mechanical vectors (x, y, z, yz, xz, xy) correspond to {1, 2, 3, 4, 5, 6} indices. Row 4 needs to be shifted to row 5, and, similarly, row 5 to row 6, and

ultimately, row 6 to row 4. This matrix involves $[s^E]^{-1} = [c^E]$ in order to evaluate $[e]$ with the properly modified rows 4, 5, 6. Ultimately, the matrix acquires the following shape [99]:

$$[e] = \begin{pmatrix} 0 & 0 & e_{31} \\ 0 & 0 & e_{32} \\ 0 & 0 & e_{33} \\ 0 & 0 & 0 \\ 0 & e_{24} & 0 \\ e_{15} & 0 & 0 \end{pmatrix}. \tag{3.1.9}$$

Harmonic analysis is used to determine the response of the structure under steady-state sinusoidal (harmonic) loading at a given frequency.

A harmonic, or frequency-response, analysis considers loading at one frequency only. Loads may be out of phase with one another, but the excitation is at a known frequency. This procedure is not used for an arbitrary transient load. One should always run free vibration analysis prior to harmonic analysis in order to obtain understanding of the dynamic characteristics of the model.

A piezoelectric element taking up volume V and surface S can be formulated by the finite elements modelling equations [100, 101].

In order to better understand harmonic analysis, the general equation of motion is provided first:

$$[M]\left\{\ddot{\xi}\right\} + [C]\left\{\dot{\xi}\right\} + [K]\left\{\xi\right\} = \{F_N\}; \tag{3.1.10}$$

where $[M]$ is the mass of matrices, $[C]$ denotes damping, $[K]$ stands for the stiffness of matrices and F_N defines the nodal vector force . $\{\xi\}$ is the vector of displacement which is obtained as follows:

$$\{\xi\} = [N_\xi]\{\xi^e\}. \tag{3.1.11}$$

The mass and damping of matrices are the following:

$$[M] = \rho \int_V [N_\xi]^T [N_\xi] dV, \tag{3.1.12}$$

$$[C] = \gamma[M] + \delta[K], \tag{3.1.13}$$

where ρ is the density of a material, γ and δ are the proportionality coefficients. If only real F_1 and imaginary F_2 components of the load are known, magnitude F_0 and phase φ can be calculated as follows:

$$F_0 = \sqrt{F_1^2 + F_2^2}, \tag{3.1.14}$$

$$\varphi = \tan^{-1}(\frac{F_2}{F_1}) . \quad (3.1.15)$$

The modelling procedure by employing the ANSYS software is the following:

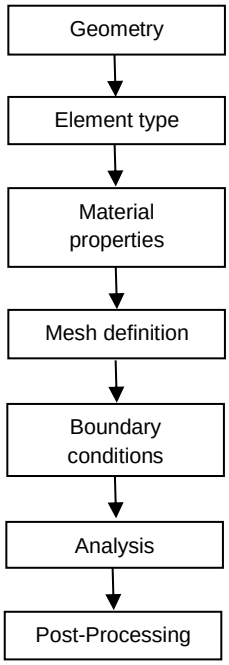

Fig. 3.1.1. Modelling procedure

Single piezoelectric elements were 3D-modelled by using the ANSYS code by SOLID5 elements with the piezoelectric e_{ij} (C/m^2), elastic c_{ij} (N/m^2) and dielectric ε_{ij} ($\varepsilon(\varepsilon_0)$) matrices of the PMN-32% PT crystal by adhering to the HC Materials Corporation database [29].

The piezoelectric element of PMN-32%PT is an anisotropic material which has 8 nodes with four nodal degrees of freedom *x* (1), *y* (2), *z* (3) directions and electric voltage *U*. In our research, the electric excitation voltage was U_{pp} = 1V. The simulation takes into account free boundary conditions and coupling between electric and mechanic fields.

The properties of the PMN-32%PT piezo-element are provided by 3.1.16, 3.1.17 and 3.1.18 matrices. The elastic c_{ij} coefficients are thus obtained:

$$c_{ij}=\begin{pmatrix} 19.95^{10} & 9.02^{10} & 2.55^{10} & 0 & 0 & 0 \\ 9.02^{10} & 11.22^{10} & 10.29^{10} & 0 & 0 & 0 \\ 2.55^{10} & 10.29^{10} & 14.57^{10} & 0 & 0 & 0 \\ 0 & 0 & 0 & 6.39^{10} & 0 & 0 \\ 0 & 0 & 0 & 0 & 0.55^{10} & 0 \\ 0 & 0 & 0 & 0 & 0 & 3.74^{10} \end{pmatrix}. \quad (3.1.16)$$

The piezoelectric e_{ij} coefficients are based on:

$$e_{ij}=\begin{pmatrix} 0 & 0 & 0 & 0 & 15.95 & 0 \\ 0 & 0 & 0 & 12.91 & 0 & 0 \\ 2.58 & -9.99 & 19.23 & 0 & 0 & 0 \end{pmatrix}, \quad (3.1.17)$$

The dielectric permittivity matrix ε (ε_0) is calculated according to:

$$\varepsilon\ (\varepsilon_0)=\begin{pmatrix} 673 & 0 & 0 \\ 0 & 1385 & 0 \\ 0 & 0 & 695 \end{pmatrix}. \quad (3.1.18)$$

The graphical representation of the finite element model is presented in Fig. 3.1.2.

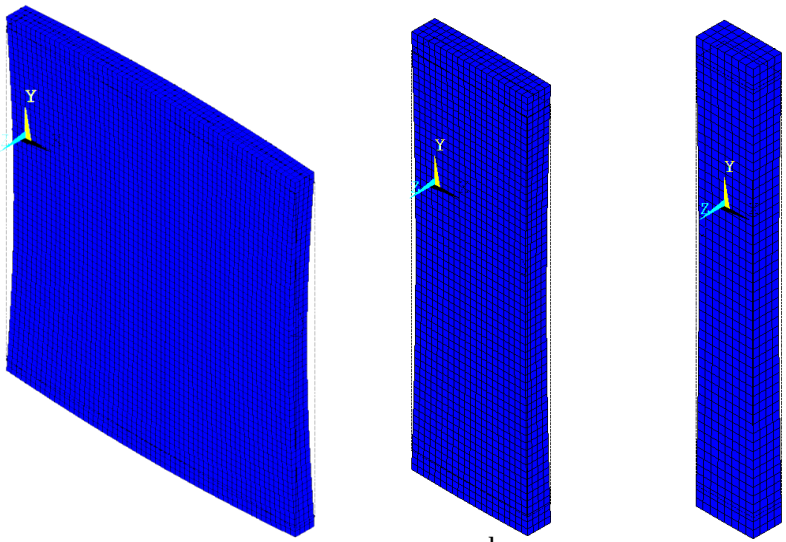

Fig. 3.1.2. The deformed shape (with its undeformed edge solid line) of PMN-32%PT elements: a – 15 x 15 x 1 mm^3; b – 15 x 5 x 1 mm^3; c – 13 x 2 x 1 mm^3

Electric input impedances Z_{IN} of three different geometries were simulated. The PMN-32%PT single crystals with the dimensions of (15 x 15 x 1) mm^3, (15 x 5 x 1) mm^3 and (13 x 2 x 1) mm^3 were investigated and are shown in Fig. 3.1.3.

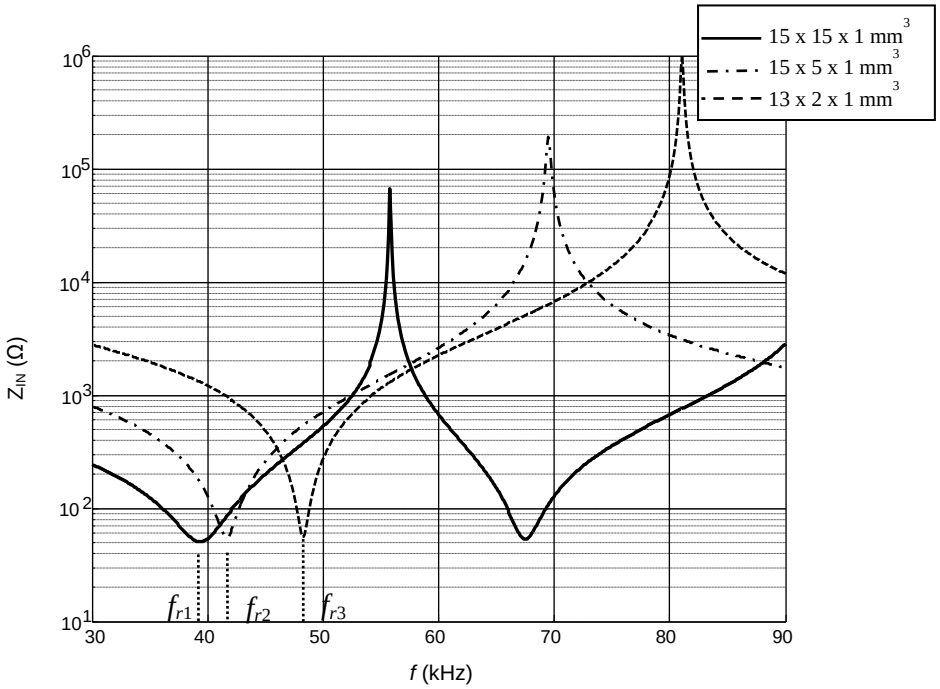

Fig. 3.1.3. Simulated electric input impedances of the single PMN-32%PT crystals with different geometry: (15 x 15 x 1) mm^3, f_{r1} = 39.3 kHz – the solid line; (15 x 5 x 1) mm^3, f_{r2} = 41.6 kHz – the dot-dashed line; (13 x 2 x 1) mm^3, f_{r3} = 48.3 kHz – the dashed line

The spatial distributions of the mechanical displacements modulus in direction *y* (2) are shown in Fig. 3.1.4. The colour scales depict the amplitude of spatial distributions of mechanical displacements in PMN-32% PT crystal elements. The red and blue colours correspond to the maximal values of mechanical displacements.

The spatial distributions of displacements of the crystal plate (15 x 15 x 1) mm^3 at the resonance frequency are more non-uniform than the distributions of the displacements of the (15 x 5 x 1) mm^3 and (13 x 2 x 1) mm^3 crystal strip and bar. We should note that for enhanced clarity the displacements in Fig. 3.1.4 are shown not to scale; they are increased by 6 x 10^4 times.

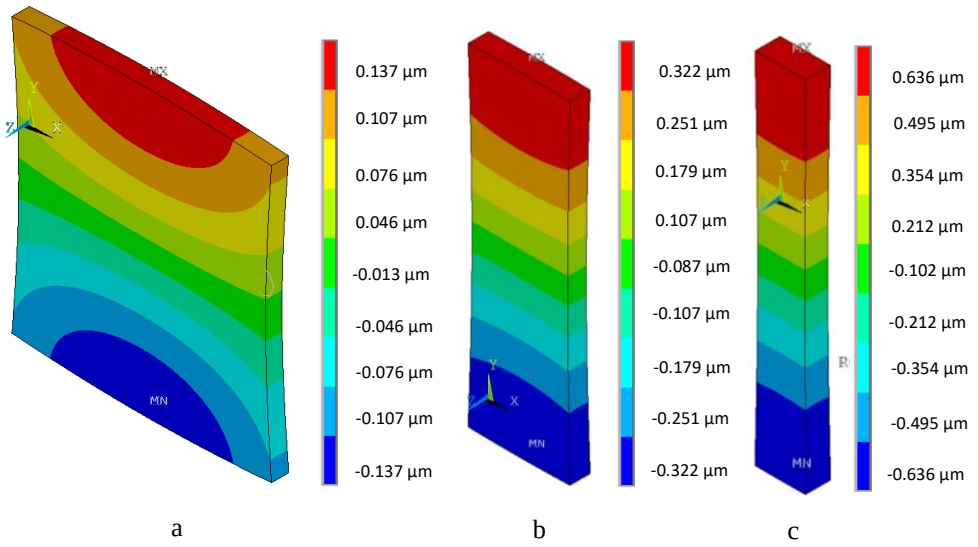

Fig. 3.1.4. Spatial distributions of the mechanical *y* (2) displacements modulus on the surface of PMN-32%PT elements: a – (15 x 15 x 1) mm^3; b – (15 x 5 x 1) mm^3; c – (13 x 2 x 1) mm^3

A 3D model of the piezo-element with the matching strip is shown in Fig. 3.1.5.

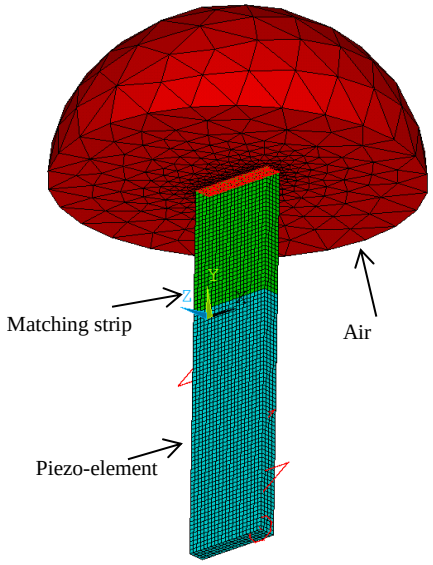

Fig. 3.1.5. A 3D model of a piezo-element with the matching strip

The frequency response of the piezo-element with different attenuation factor β according to [101] is the following:

$$\beta = \frac{1}{2\pi(f_{bd} + f_{ed})Q_m}; \qquad (3.1.19)$$

where f_{bd} = 32 kHz and f_{ed} = 48 kHz represent the frequencies interval which is shown in Fig. 3.1.6. The mechanical quality factor possesses the value equal to Q_m = 100, damping β is provided by equation 3.1.19, density is ρ = 8100 kg·m^{-3}, the dielectric constant equals ε_0 = 8.85x10^{-12} C/N·m^2.

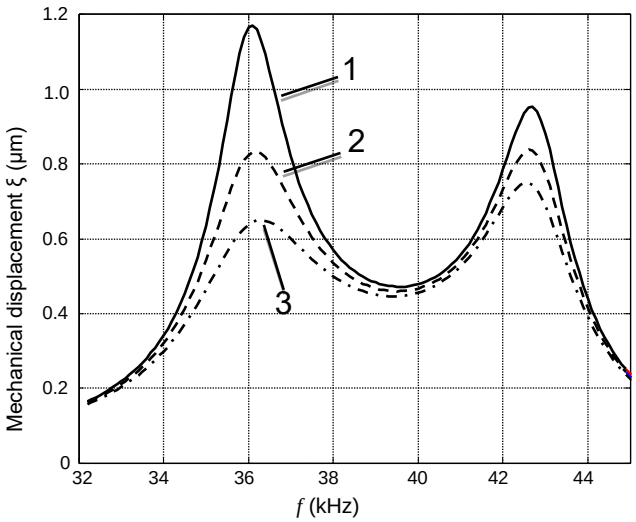

Fig. 3.1.6.Attenuation β (simulated by FEM) in the matching strip:
1 – 2*10^{-7}; 2 – 3*10^{-7}; 3 – 4*10^{-7}

From the simulated results, it follows that the best performance of attenuation β in the matching strip is 3*10^{-7}. As a result, 3D spatial distributions of mechanical displacements in piezoelectric single crystal elements were obtained.

3.2. Experimental investigation of the electric input impedance

The frequency measurement method was used for the measurements and for the calculation of all the material piezoelectric coefficients. Resonance frequencies f_r, f_a of PMN-32%PT single crystal elements of the transverse extension mode were measured. Electric input impedances Z_{IN} of PMN-32%PT crystals with different dimensions (15 x 15 x 1) mm^3, (15 x 5 x 1) mm^3 and (13 x 2 x 1) mm^3 were investigated and are shown in Fig. 3.2.1.

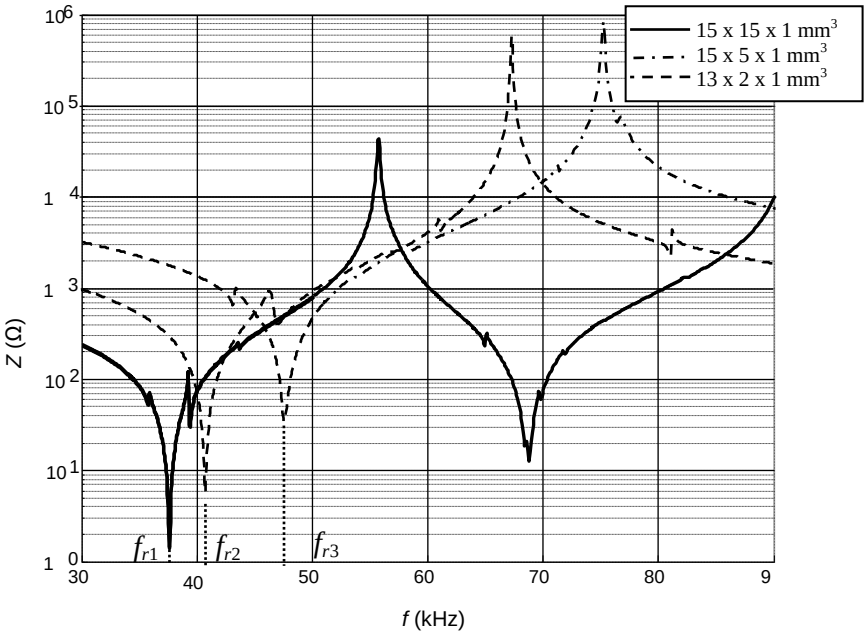

Fig. 3.2.1. Measurement of the electric input impedances Z_{IN}: (15 x 15 x 1) mm^3, f_{r1} = 37.5 kHz – the solid line, (15 x 5 x 1) mm^3, f_{r2} = 40.7 kHz – the dashed line, (13 x 2 x 1) mm^3, f_{r3} = 47.5 kHz – the dot-dashed line

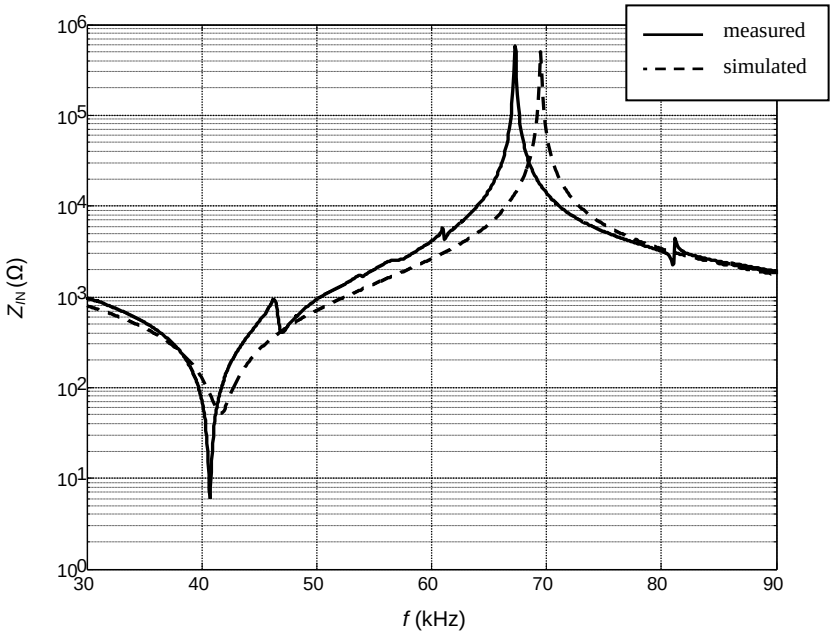

Fig. 3.2.2. Electric input impedances Z_{IN} (15 x 5 x 1) mm^3: the solid line – measured with the Wayne Kerr B6500 meter, the dashed line – simulated by FEM

Electrical input impedance obtained with the Wayne Kerr B6500 of PMN-32%PT (15 x 5 x 1) mm^3 is compared with the simulated curves calculated by ANSYS in the same frequency range considering the damping of the piezo-element (Fig. 3.2.2).

Good agreement between the finite element simulation and the measurement results was observed.

3.3. Experimental investigation of vibrations of PMN-32%PT crystals

The second method of measuring the piezoelectric charge coefficient is the laser interferometer method. This method is based on measuring the displacement of the sample surface.

For air-coupled applications, usually ultrasonic waves with the frequencies of $f < 1$ MHz are used. In order to generate and pick up such relatively low frequency waves, a suitable vibration mode of PMN-32%PT crystals must be selected. Experimental validation of the proposed technique was performed on the PMN-32%PT single crystal produced by "HC Materials Corporation". The bracket for the measurement of PMN-32%PT single crystal is shown in Fig. 3.3.1, *a* and *b*.

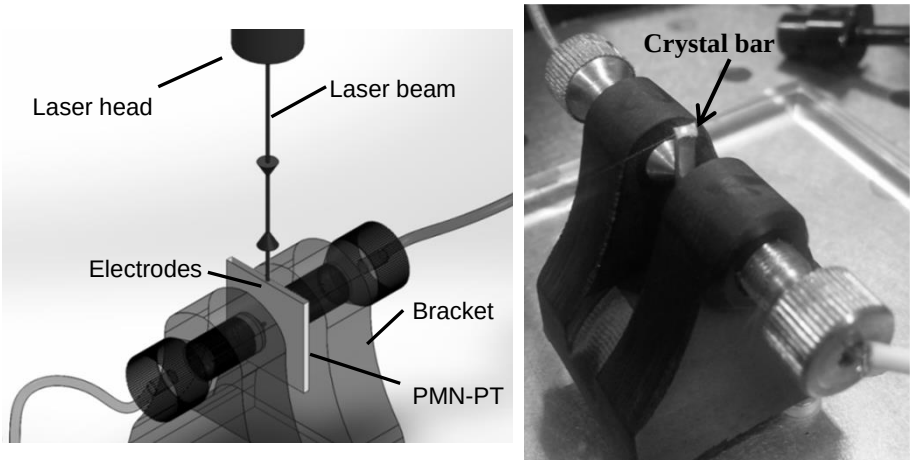

a b

Fig. 3.3.1. The bracket for the measurement of PMN-32%PT crystal displacements: a – the plate; b – the bar

The measurement samples of PMN-32%PT crystal plates are outlined in Table 3.3.1. The single crystal plates are with gold electrodes produced by HC Materials Corporation.

Table 3.3.1. The geometries of the measured samples

No.	Mode	Poling direction	Geometry L x w x t mm^3	Sample shape	Units
1.	Thickness	[001]	15 x 15 x 1	plate	7
2.	Transverse Extension	[011]	15 x 15 x 1	plate	6
3.	Transverse Shear	[111]	15 x 15 x 1	plate	7

The measurement results of PMN-32%PT crystal plates in the thickness mode when they are poled in [001] direction are shown in Tables 3.3.2 and 3.3.3 focusing on different geometries: (15 x 5 x 1) mm^3 and (5 x 5 x 0.2) mm^3.

Table 3.3.2. PMN-32%PT crystal plates (15 x 15 x 1) mm^3, [001]-poled; thickness mode

Excitation voltage 1 V							
$\varepsilon_0 = 8.85*10^{-12}$ C^2/Nm^2							
ϱ = 8,100 kg/m^3							
	Plate No. 1	**Plate No. 2**	**Plate No. 3**	**Plate No. 4**	**Plate No. 5**	**Plate No. 6**	**HC Materials datasheet**
C^T(1kHz), nF	9.5	9.5	9.6	10.3	10.2	10.2	-
C^S(4 MHz), nF	1.7	1.7	1.7	1.8	1.8	1.8	
Frequencies f_a, f_r (MHz)	f_a=2.2632 f_r=1.9474	f_a=2.2941 f_r=1.9374	f_a=2.2734 f_r=1.9387	f_a=2.2645 f_r=1.9374	f_a=2.261 f_r=1.937	f_a=2.2634 f_r=1.9401	
ε^S_{33}	883	888	888	915	915	917	700
ε^T_{33}	4773	4808	4835	5203	5169	5133	7000
k_t	0.56	0.57	0.56	0.56	0.55	0.55	0.62
$\boldsymbol{k_{33}}$	**0.90**	**0.90**	**0.90**	**0.91**	**0.91**	**0.91**	**0.93**
e_{33} (C/m^2)	20.28	20.04	20.36	20.42	20.38	20.33	19.42
h_{33}, 10^8 (V/m)	25.95	26.76	25.91	25.21	25.08	25.05	31.34
c^D_{33}, 10^{10} (N/m^2)	16.76	17.05	16.74	16.61	16.56	16.60	15.77
c^E_{33}, 10^{10} (N/m^2)	11.50	11.42	11.47	11.46	11.46	11.50	9.04

Table 3.3.3. PMN-PT crystal plates (5 x 5 x 0.2) mm^3, [001]-poled; thickness mode

Excitation voltage 1 V		
$\varepsilon_0 = 8.85*10^{-12}$ (C^2/Nm^2)		
	No. 1	**No. 2**
C^T (1kHz), nF	5.1	5.7
C^S (20MHz), pF	249.4	251.7
Frequencies f_a, f_r, MHz	f_a=11.405 f_r=9.6904	f_a=11.210 f_r=9.9193
ε^S_{33}	225	227
ε^T_{33}	4585	5154
k_t	0.57	0.50
$\boldsymbol{k_{33}}$	**0.98**	**0.98**
e_{33} (C/m^2)	10.39	9.13
h_{33} 10^8 (V/m)	52.07	45.31
c^E_{33}, 10^{10} (N/m^2)	11.45	12.15

Results of the transverse extension mode when poling takes place in [011] direction are shown in Table 3.3.4.

Table 3.3.4. PMN-32%PT crystal plates (15 x 15 x 1) mm^3, [011]-poled; transverse extension mode

Excitation voltage 1 V							
$\varepsilon_0 = 8.85*10^{-12}$ C^2/Nm^2							
	Plate No. 1	**Plate No. 2**	**Plate No. 3**	**Plate No. 4**	**Plate No. 5**	**Plate No. 6**	**HC Materials datasheet**
C^T(1 kHz), nF	10.0	10.2	10.1	10.1	10.3	9.9	-
C^S(5 MHz), nF	1.3	1.3	1.3	1.3	1.3	1.3	
Frequencies f_a, f_r, MHz	f_a=2.5445 f_r=2.2463	f_a=2.5445 f_r=2.2463	f_a=2.5094 f_r=2.2463	f_a=2.5094 f_r=2.2463	f_a=2.5094 f_r=2.2463	f_a=2.5094 f_r=2.2463	-
ε^S_{33}	667	667	672	661	663	667	-
ε^T_{33}	5043	5154	5071	5073	5174	4973	-
k_t	0.51	0.51	0.48	0.48	0.48	0.48	0.54
$\boldsymbol{k_{31}}$	**0.78**	**0.77**	**0.77**	**0.77**	**0.77**	**0.77**	**0.74**
$\boldsymbol{k_{32}}$	**0.82**	**0.81**	**0.81**	**0.82**	**0.82**	**0.84**	**0.91**
s^E_{11}, 10^{-12} (m^2/N)	29.27	29.38	28.85	29.17	29.70	29.06	15.85
s^E_{22}, 10^{-12} (m^2/N)	93.95	93.31	92.16	95.80	96.51	98.38	78.18

	Plate No. 1	**Plate No. 2**	**Plate No. 3**	**Plate No. 4**	**Plate No. 5**	**Plate No. 6**	**HC Materials datasheet**
c^D_{33}, 10^{10} (N/m^2)	20.97	20.97	20.40	20.40	20.40	20.40	20.58
d_{31}, 10^{-12} (C/N)	879	888	868	877	900	866	670
d_{32}, 10^{-12} (C/N)	–1670	–1670	–1647	–1700	–1718	–1740	–1820
g_{31}, 10^{-3} (Vm/N)	19.7	19.5	19.3	19.5	19.7	19.7	13.12
g_{32}, 10^{-3} (Vm/N)	–37.4	–36.6	–36.7	–37.9	–37.5	–39.5	–35.64
32 mode							
Frequencies f_a, f_r (kHz)	f_a=55.63 f_r=38.21	f_a=55.39 f_r=38.34	f_a=55.76 f_r=38.58	f_a=55.39 f_r=37.84	f_a=55.01 f_r=37.7	f_a=55.88 f_r=37.34	-
Velocities c_a,(m/s)	1669	1662	1673	1662	1650	1676	-
Z_a, (MRayl)	13.51	13.46	13.55	13.46	13.36	13.57	-
31 mode							
Frequencies f_a, f_r (kHz)	f_a=94.22 f_r=68.45	f_a=93.84 f_r=68.33	f_a=94.22 f_r=68.95	f_a=94.09 f_r=68.58	f_a=93.84 f_r=67.96	f_a=94.22 f_r=68.7	-
Ultrasound velocities c_a, (m/s)	2827	2815	2826	2823	2815	2827	-
Acoustic impedance Z_a (MRayl)	22.90	22.80	22.89	22.87	22.80	22.90	-

The results of the transverse shear mode with the poled [111] direction are shown in Table 3.3.5.

Table 3.3.5. PMN-32%PT crystal plates (15 x 15 x 1) mm^3, [111]-poled; transverse shear 15 mode

Excitation voltage 1 (V)						
$\varepsilon_0 = 8.85*10^{-12}$ (C^2/Nm^2)						
Ϙ = 8,100 (kg/m^3)						
	Plate No. 1	**Plate No. 2**	**Plate No. 3**	**Plate No. 4**	**Plate No. 5**	**Plate No. 6**
C^T(1kHz), nF	20.6	18.0	20.1	19.2	24.2	17.5
C^S(2.3 MHz), nF	1.9	1.9	1.9	1.9	1.9	1.9
Frequencies f_a, f_r (MHz)	f_a=1.1524 f_r=0.3919	f_a=1.1487 f_r=0.4188	f_a=1.1499 f_r=0.3769	f_a=1.1218 f_r=0.3775	f_a=1.1637 f_r=0.3475	f_a=1.1418 f_r=0.4013
ε^S_{11}	979	972	988	999	1002	986

	Plate No. 1	**Plate No. 2**	**Plate No. 3**	**Plate No. 4**	**Plate No. 5**	**Plate No. 6**
ε^T_{11}	10329	9050	10140	9667	12141	8789
k_{15}	0.95	0.94	0.95	0.95	0.96	0.95
e_{15}, (C/m^2)	18.56	18.44	17.74	17.31	18.02	17.48
h_{15}, 10^8 (V/m)	21.42	21.43	20.29	19.57	20.32	20.01
c^E_{44}, 10^{10} (N/m^2)	41.72	47.79	38.54	38.70	32.66	41.83
s^E_{44}, 10^{-12} (m^2/N)	239.65	209.23	259.47	258.39	306.17	228.25
s^E_{55}, 10^{-12} (m^2/N)	239.65	209.23	259.47	258.39	306.17	228.25
s^D_{44}, 10^{-12} (m^2/N)	23.24	23.39	23.34	24.52	22.79	23.67
d_{15}, 10^{-12} (C/N)	4447	3858	4603	4473	5518	3989
g_{15}, 10^{-3} (Vm/N)	48.7	48.2	51.3	52.3	51.4	51.3

The piezoelectric properties of the crystals after the poling procedure were additionally evaluated with the laser interferometer. The laser interferometer method was applied for the measurement of the crystal displacements which were used for the estimation of the piezoelectric charge coefficients d_{31} and d_{32}.

Measurements were performed at a low frequency, specifically, 3 Hz. The interferometer sensitivity was set to 0.0625 V/μm. Measurements were performed at five excitation voltages: U = 40 V, U = 80 V, U = 120 V, U = 160 V, U = 200 V, and no non-linearity of piezoelectric properties was observed (Fig. 3.3.2).

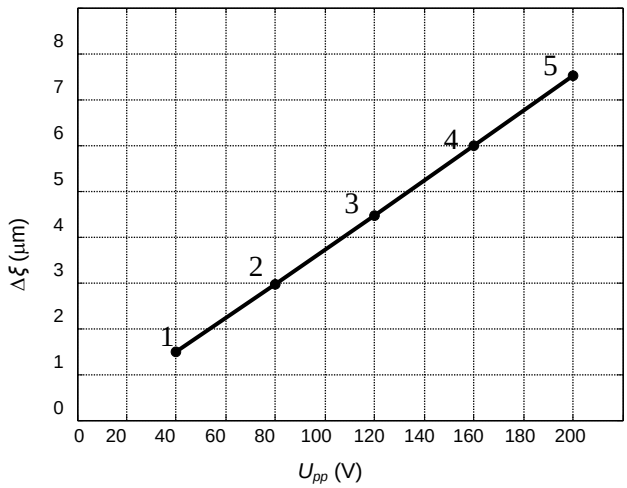

Fig. 3.3.2. The measured mechanical displacement versus the applied voltage

The mechanical displacements of the PMN-32%PT single crystal plate measured in two orthogonal x (1) and y (2) directions are presented in Fig. 3.3.3.

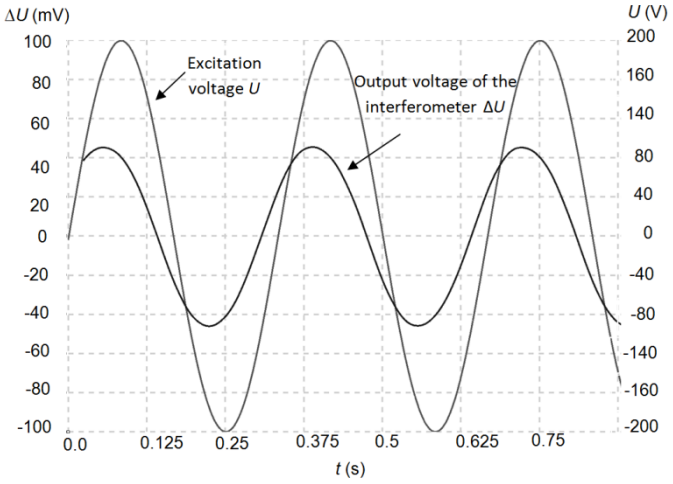

a

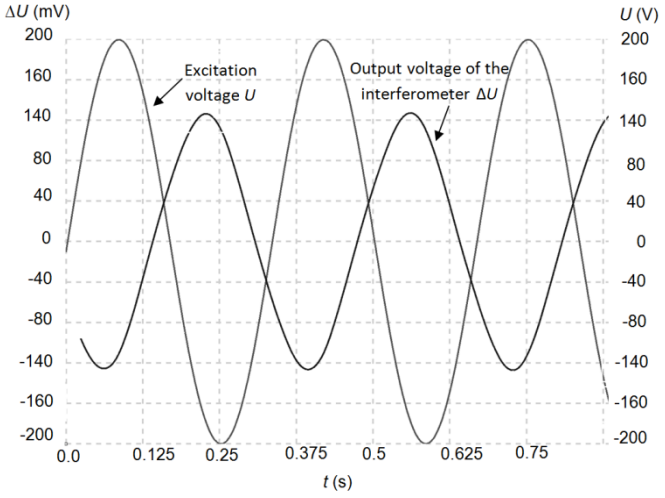

b

Fig. 3.3.3. Normal displacements of the PMN-32%PT plate edges:
a – *x* (1) direction; b – orthogonal *y* (2) direction

The piezoelectric charge d_{3i} coefficients were measured by employing the laser interferometer method and calculated according to [4]:

$$d_{3i} = \frac{\Delta l}{U} = \frac{S_t \Delta U}{\frac{U}{T} l}; \tag{3.3.1}$$

where d_{3i} (pC/N); i = 1, 2; S_t (μm·V^{-1}) is the interferometer sensitivity; ΔU (V) is the output voltage of the interferometer, which is proportional to displacement ξ_{3j}; U (V) is the excitation voltage; T (mm) is the thickness of the crystal plate; l (mm) is the

distance to the fixing point. The measured electromechanical coupling coefficients are d_{31} (487 ÷ 577 pC/N) and d_{32} (–1317 ÷ –1626 pC/N).

The PMN-32% PT crystals are an anisotropic material; therefore, elastic and piezoelectric properties in the directions of *x* (1) axis and *y* (2) axis are different (Fig. 3.3.4). The main transverse extension mode resonant frequencies in the two orthogonal directions were investigated for the set of single crystals of <011> cut and [011]-poling directions with different dimensions. If we take into account that electromechanical coupling coefficient k_{32} possesses the highest value in direction *y* (2), it was naturally selected for the radiation of ultrasonic waves into air. In this case, the edge of the piezoelectric plate perpendicular to the direction *y* (2) for radiation and reception of ultrasonic waves is used.

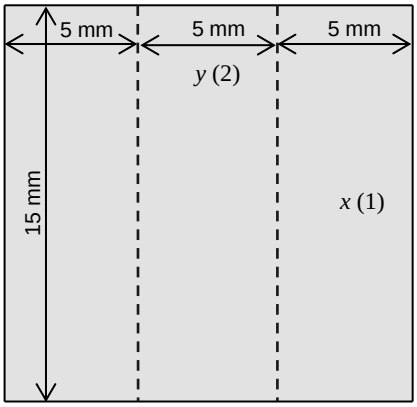

Fig. 3.3.4. Geometry of PMN-32%PT elements

In order to estimate the spatial distribution of the normal displacements of the PMN-32%PT, crystal plate measurements with the laser vibrometer POLYTEC OFV-5000 were carried out. The experimental setup used for the measurement of crystal displacements is shown in Fig. 1.4.3.

The six piezoelectric crystal plates with the dimensions of (15 x 15 x 1) mm^3 were measured. During the measurements, the electric excitation voltage was U_{pp} = 1V, and the sensitivity of the interferometer was set to S_t = 0.0625 V/μm. The measurements were performed at two main resonance frequencies f_{r1} = 37.5 kHz and f_{r2} = 69.2 kHz corresponding respectively to the directions *y* (2) and *x* (1). From the measured normal mechanical displacements, piezoelectric charge coefficients d_{ij} were calculated. The results of measurements of displacements ξ_{31} and ξ_{32} at the first resonance frequency f_{r1}=37.5 kHz and the second resonance frequency f_{r2} = 69.2 kHz are presented respectively in Fig. 3.3.5, *a* and 3.3.5, *b*. For superior understanding, the displacements are shown in the enlarged scale at 2 μm/ division. The mechanical displacements in direction *y* (2) are significantly more prominent than in direction *x* (1); therefore, frequency f_{r1} = 37.5 kHz and direction *y* (2) were selected for the radiation of ultrasonic waves. We should note that due to the resonance phenomenon and mode coupling, spatial distributions of normal displacements are rather non-uniform.

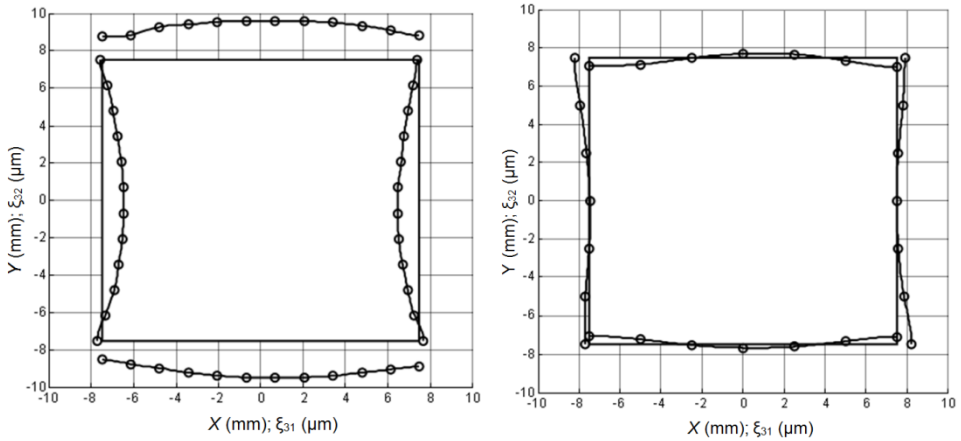

a b

Fig. 3.3.5. Normal mechanical displacements $\xi_{31}$and ξ_{32} of the edges of the PMN-32% PT crystal plates at two main resonance frequencies: a – the first resonance, f_{r1} = 37.5 kHz; b – the second resonance, f_{r2} = 69.2 kHz

The spatial distribution of normal displacements was measured by scanning the crystal elements in *x* and *y* directions with the scanning step being set to 0.1 mm. The frequency response (36.0 kHz – 39.0 kHz) of single piezoelectric elements with different orientations *x* (1) and *y* (2) is presented in Fig. 3.3.6.

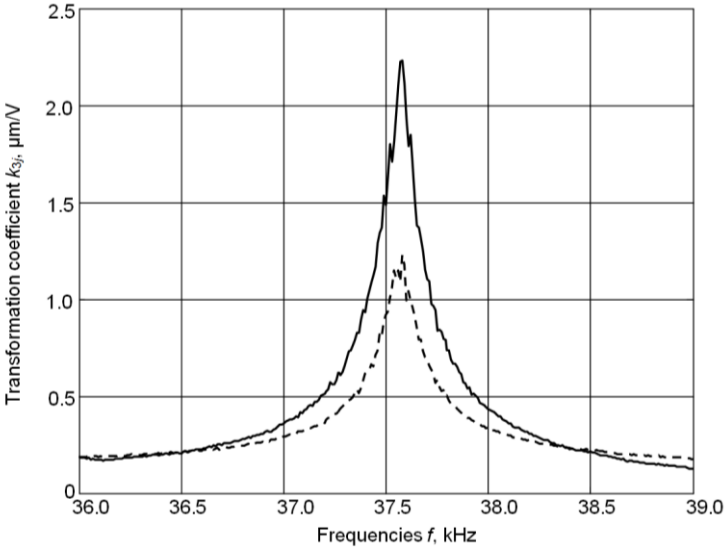

Fig. 3.3.6. Electromechanical transformation coefficient k_{3j} of the PMN-32%PT single crystal (15 x 15 x 1) mm^3: *y* (2) direction – the solid line; *x* (1) direction – the dashed line

PMN-32%PT single crystals with the dimensions of (15 x 15 x 1) mm^3 (Fig. 3.3.4) were sliced into narrower strips (15 x 5 x 1) mm^3 and (13 x 2 x 1) mm^3 which

were investigated. The spatial distributions of mechanical displacements of the active surfaces of the crystals were evaluated in the dynamic mode when they were excited by a long radio pulse (N = 130 periods) by using a laser interferometer system.

The efficiency of electromechanical transformation was estimated by k:

$$k_{3j} = \frac{\xi_{3j}}{U}; \tag{3.3.2}$$

where k_{3j} is the transformation coefficient in direction x (1) or in direction y (2), j = 1, 2 are the indicated directions, ξ_{3j} is the mechanical displacement of the plate edge in direction x (1) or in direction y (2), U is the applied electric voltage. The results of the measurements are shown in Table 3.2.6.

Table 3.3.6. Measurement results of (15 x 15 x 1) mm^3 PMN-32%PT plates

Plates (15 x 15 x 1) mm^3	Directions	Resonance frequency f_r (kHz)	Transformation coefficient k_{3j} (μm/V)
1	y (2)	37.3	2.3
	x (1)	37.3	1.2
2	y (2)	37.5	2.2
	x (1)	37.5	1.1
3	y (2)	38.4	2.3
	x (1)	38.4	1.1

The results of measurements of spatial distributions of the normal displacements of the (15 x 15 x 1) mm^3 plate edges at the main resonance frequency f_r = 37.5 kHz are presented respectively in Fig. 3.3.7, *a* and 3.3.7, *b*. The colour scales in each figure depict the amplitude of mechanical displacements. The red colour corresponds to the maximal values whereas the blue colour denotes the minimal values of mechanical displacements. From the measurement results, it follows that the maximal mechanical displacement is obtained in direction y (2), and it is ξ_{32} = 15 nm at the centre of the plate edge. It is higher than in direction x (1); therefore, direction y (2) may be used for the radiation of ultrasonic waves. The spatial distributions of the normal displacements are non-uniform. In order to obtain more uniform distributions, the rectangular PMN-32%PT single crystals were cut into narrower strips (15 x 5 x 1) mm^3 and (13 x 2 x 1) mm^3. The measurement results at resonance f_r = 40.6 kHz of spatial displacements of single crystal strips (15 x 5 x 1) mm^3 are shown in Fig. 3.3.8 and Fig. 3.3.10 where the results for the main resonance f_r = 40.6 kHz of spatial displacements B and A-scan are presented. The results of the measurements are shown in Table 3.2.7. We should note, that transformation coefficient k_{3j} of a (15 x 5 x 1) mm^2 crystal strip is ~2.2 times higher than that of the (15 x 15 x 1) mm^3 crystal plate. The results of the measurements of bar (13 x 2 x 1) mm^3 are shown in Fig. 3.3.9 and Table 3.2.8.

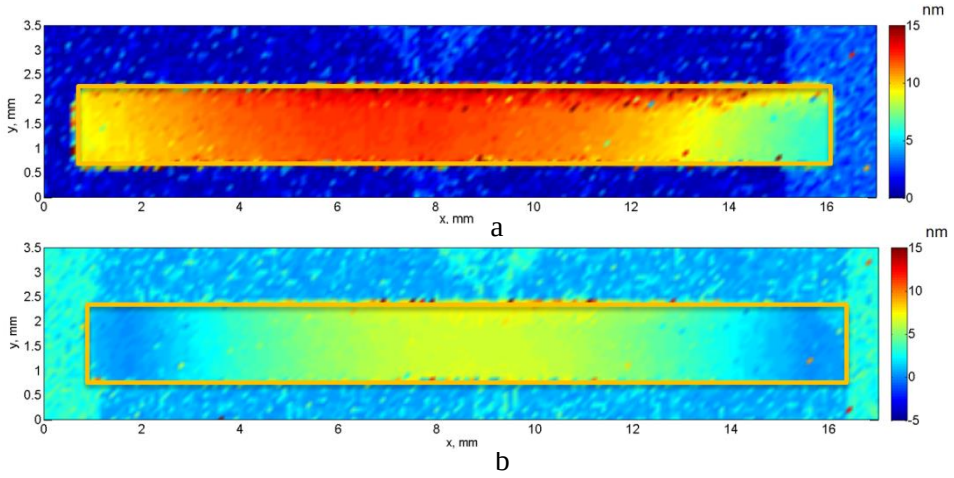

Fig. 3.3.7. Spatial displacements of the (15 x 15 x 1) mm^3 PMN-32%PT, plate edges at f_r = 40.2 kHz: a – *y* (2) direction; b – *x* (1) direction

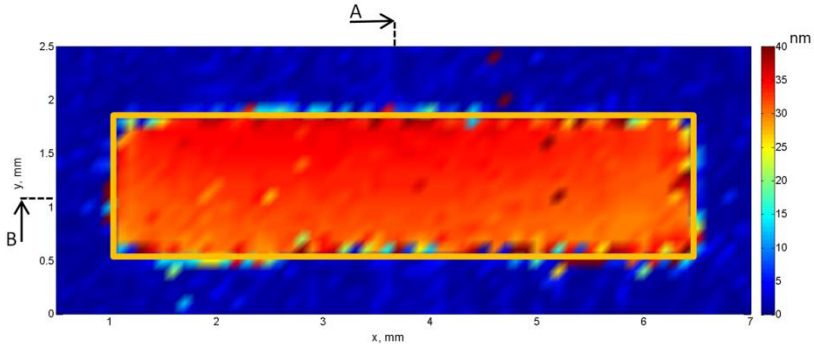

Fig. 3.3.8. Spatial displacements of the (15 x 5 x 1) mm^3 PMN-32%PT, strip edge at f_r = 40.6 kHz

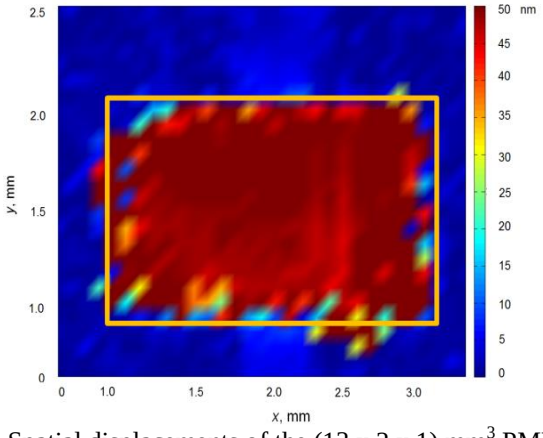

Fig. 3.3.9. Spatial displacements of the (13 x 2 x 1) mm^3 PMN-32%PT, bar edge at f_r = 46.2 kHz

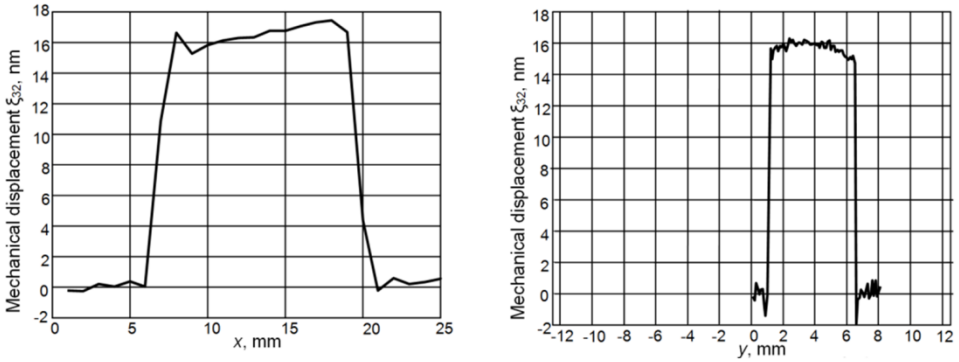

a b

Fig. 3.3.10. Main resonance f_r = 40.6 kHz of spatial displacements of the (15 x 5 x 1) mm^3 piece: a – B-scan, y = 1.1 mm; b – A-scan, x = 3.5 mm

Table 3.2.7. Measurement results of PMN-32%PT strips

Strips (15 x 5 x 1) mm^3	Resonance frequencies f_r (kHz)	Transformation coefficient k_{32} (μm/V)
1	40.6	5.1
2	41.0	5.0
3	41.1	4.9

Table 3.2.8. Measurement results of PMN-32%PT bars

Bars (13 x 2 x 1) mm^3	Resonance frequencies f_r (kHz)	Transformation coefficient k_{32} (μm/V)
1	46.2	0.94
2	45.9	0.75
3	45.8	0.78

Transformation coefficient k_{32} of (15 x 5 x 1) mm^3 single element is presented in Fig. 3.3.11.

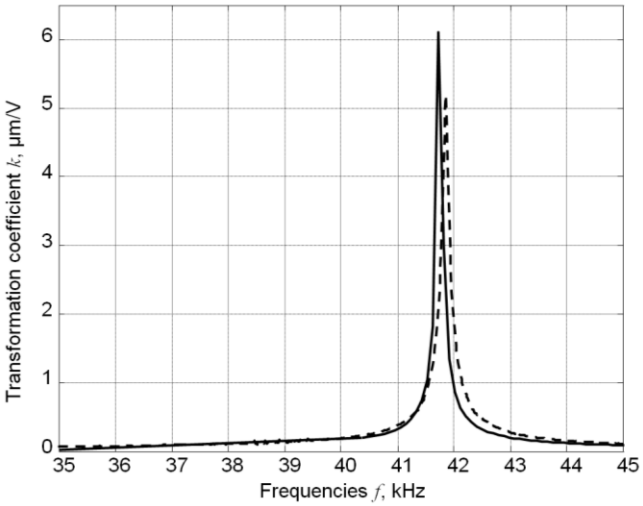

Fig. 3.3.11. Transformation coefficient k_{32}: the solid line – as simulated with FEM, the dashed line – as measured with the laser interferometer

The spatial distributions of the normal displacements of the (15 x 5 x 1) mm^3 and (13 x 2 x 1) mm^3 elements are more uniform than those of the (15 x 15 x 1) mm^3 plates. The highest transformation coefficient was observed in the case of the (15 x 5 x 1) mm^3 PMN-32%PT elements.

3.4. Acoustic matching of air-coupled ultrasonic transducer

Vibrations and frequency responses of single PMN-32%PT element transducers were investigated both theoretically and experimentally. In order to obtain a more uniform distribution of the displacements on the active surface used for the radiation of ultrasonic waves, the PMN-32%PT single crystals of dimensions (15 x 15 x 1) mm^3 were cut into narrower strips with the dimensions of (15 x 5 x 1) mm^3 and for the radiation of ultrasonic waves, the edge perpendicular to direction *y* (2) was selected where arrows indicate the radiation of the active aperture (Fig. 3.4.1).

Theoretical analysis was based on finite elements modelling (FEM) which was performed by using the ANSYS Mechanical APDL software with SOLID5 elements possessing piezoelectric properties.

For the improvement of the performance, special acoustic matching elements made of low impedance plastics were bonded to the active edge of the crystal [102 – 109]. It justifies the selection of the PMN-32%PT piezoelectric strips with the dimensions of (15 x 5 x 1) mm^3 as the active elements for air-coupled ultrasonic

transducers. The performance of ultrasonic transducers may be significantly enhanced by matching the elements attached to the piezoelectric strips (Fig. 3.4.1, *a* and *b*).

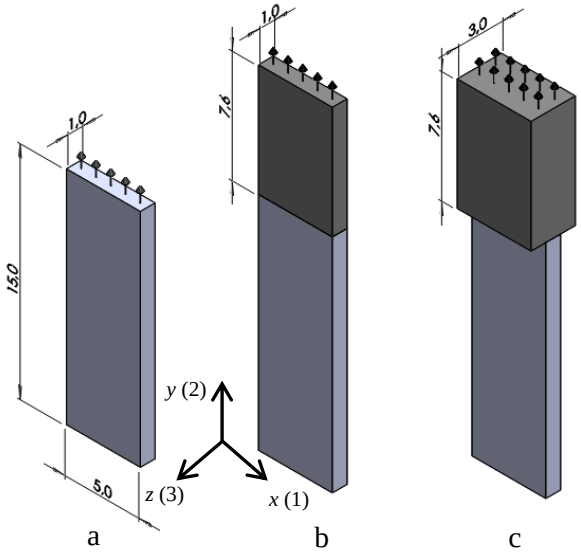

Fig. 3.4.1. Air-coupled ultrasonic transducers (the arrows indicate the radiation of the active aperture): a – a single PMN-32%PT element; b – a single element with the matching strip (the darker colour; the thickness equals w = 1 mm);
c – a single element with the matching strip (the thickness measures w = 3 mm)

In order to select the most suitable material, various materials – such as polystyrene foam AIREX R90.200, AIREX R90.300 and *FinnFoam* – were investigated. The acoustic properties of these materials are presented in Table 3.4.1.

Table 3.4.1. The properties of polymers used in the matching elements

Bulk materials			
Properties	**AIREX R90.200**	**AIREX R90.300**	***FinnFoam***
Density ρ (kg/m^3)	200	300	38
Ultrasound velocity c (m/s)	1340	1513	700
Acoustic impedance Z_s (MRayl)	0.268	0.454	0.0266

The velocity of the ultrasonic longitudinal wave was measured by employing the through-transmission pulse method at the frequency of 50 kHz in specially prepared samples, the dimensions of which were bigger than the wavelength. The length of the matching strips was chosen according to the wavelength of the ultrasonic waves in the polymeric matching element λ at the operation frequency, e.g. λ/4. We should note that the ultrasound velocity in the matching strips is lower

than in bulk materials; therefore, in order to select the proper length of the matching strips, the ultrasound velocity was measured in the strips not exceeding the thickness of 1 mm. Height h and length L in the bulk material are >> λ (the wavelength of ultrasonic waves), but h, L in the strip material are ~< λ. The boundary conditions of the waveguide affect the ultrasound velocity in the matching strip. The results of these measurements are presented in Table 3.4.2.

Table 3.4.2. The acoustic properties of strip-like matching elements

Strip-like materials			
Properties	**AIREX R90.200**	**AIREX R90.300**	***FinnFoam***
Ultrasound velocity c (m/s)	1272	1385	326
Acoustic impedance Z_s (MRayl)	0.254	0.415	0.0124
λ/4 (mm)	7.6	8.3	2.0

The simulated frequency responses of the mechanical displacements of the active surface of the ultrasonic transducer without the matching strip and with the different matching strips (AIREX R90.200 and AIREX R90.300) are presented in Fig. 3.4.2 and Fig. 3.4.3. The electric generator output impedance equals $R_g = 50$ Ω whereas excitation voltage $U_{pp} = 1$ V is applied.

In the case of the thick matching strip ($w = 3$ mm, Fig. 3.4.3), the frequency response becomes more non-uniform in comparison to the matching strip ($w = 1$ mm); the latter is the same as the thickness of the piezoelectric element.

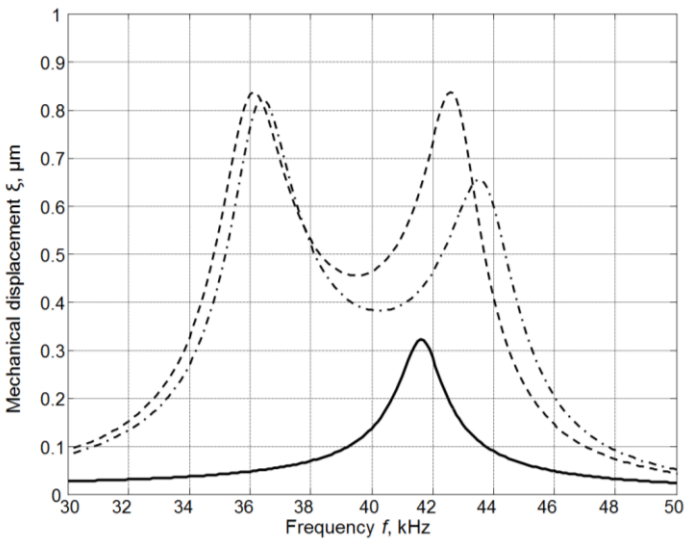

Fig. 3.4.2. Simulated frequency responses of the single PMN-32%PT element mechanical displacements: the solid line shows the data for the sample without the matching strip; for the data with the matching strip ($w = 1$ mm, $R_g = 50$ Ω): AIREX R90.200 is represented by the dashed line; AIREX R90.300 is shown by the dot-dashed line

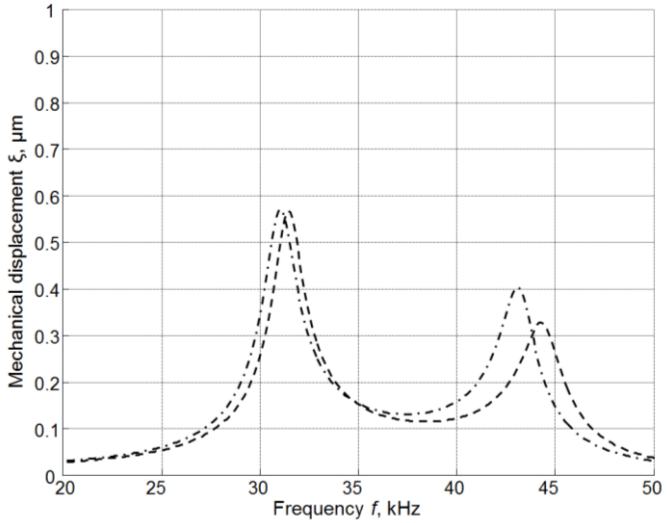

Fig. 3.4.3. Simulated frequency responses of the single PMN-32%PT element mechanical displacements with the matching strip (w = 3 mm, R_g = 50 Ω): the dashed line stands for AIREX R90.200; the dot-dashed line represents AIREX R90.300

The measured frequency responses of the displacements which are normal to the active surface are shown in Fig. 3.4.4.

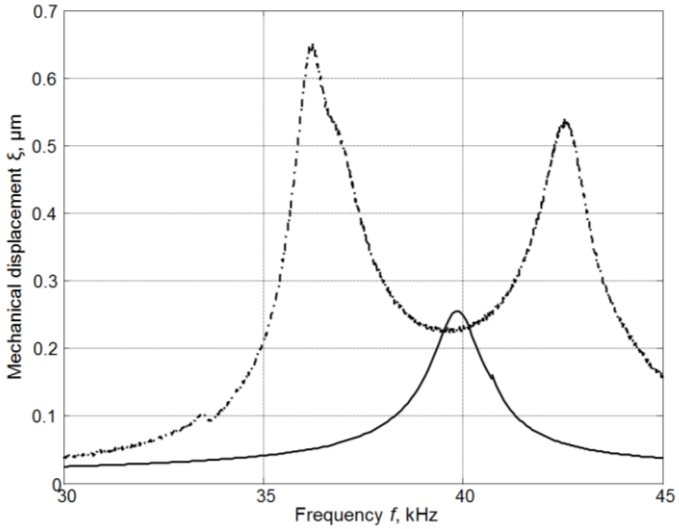

Fig. 3.4.4. The frequency response of the PMN-32%PT (15 x 5 x 1) mm^3 single crystal element without the matching strip (the solid line) and with the matching strip (the dashed line) measured with the laser interferometer

From the presented results, it follows that the most uniform frequency response is obtained in the case of the thin matching strip (w = 1 mm) made of polystyrene foam AIREX R90.200 and electric generator output impedance R_g = 50 Ω. The

frequency responses of the acoustic pressure in air as measured by employing the B& K 4138 type microphone are presented in Fig. 3.4.5.

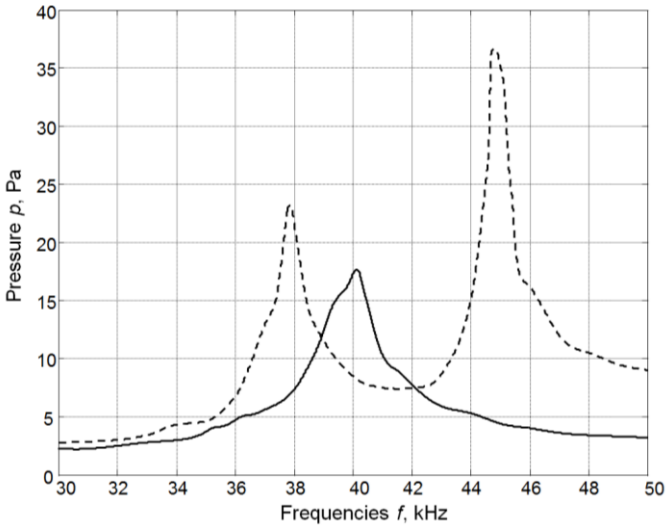

Fig. 3.4.5. Solid line depicts the single element; the dashed line represents the single element with the matching strip

The experimentally determined pulse response of the transducer with the matching strip made of AIREX R90.200 is presented in Fig. 3.4.6, *a*. For a comparison, the pulse radiated by the commercially available Murata MA40B7 transducer is shown in Fig. 3.4.6, *b*. Murata MA40B7 transducers are widely used around the world. Both transducers were excited by the burst of 5 periods with the central frequencies adjusted to the operation frequencies of the transducers, e.g. close to f_r = 40 kHz.

The peak-to-peak excitation voltage in both cases was the same: U_{pp} = 18 V. The measurements were performed in air by B& K instrumentation using 1/8 inch B& K 4138 microphone [110 – 112]. From the presented results, it is possible to see a much better performance of the PMN-32%PT single crystal transducer.

The frequency responses were obtained by calculating the displacements of the central point of the radiating surface with FEM at different frequencies. The matching strips made of *FinnFoam* material do not help to improve the frequency response of the transducer; however, they may still be used as the spacing elements in the ultrasonic array. In all cases, the output electric impedance of the electric generator was R_g = 50 Ω.

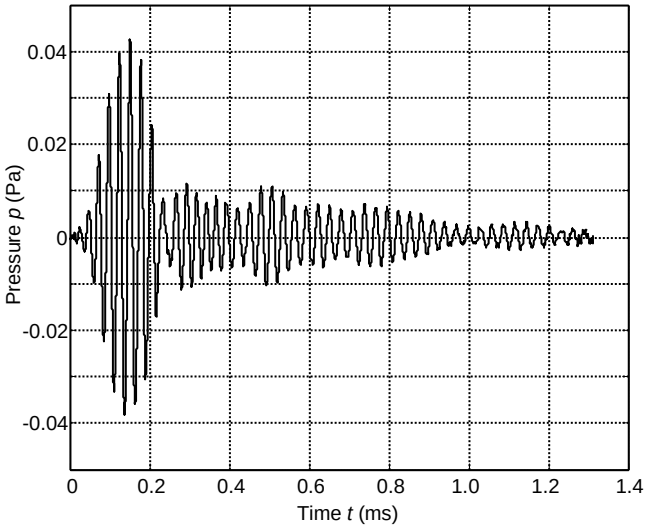

a

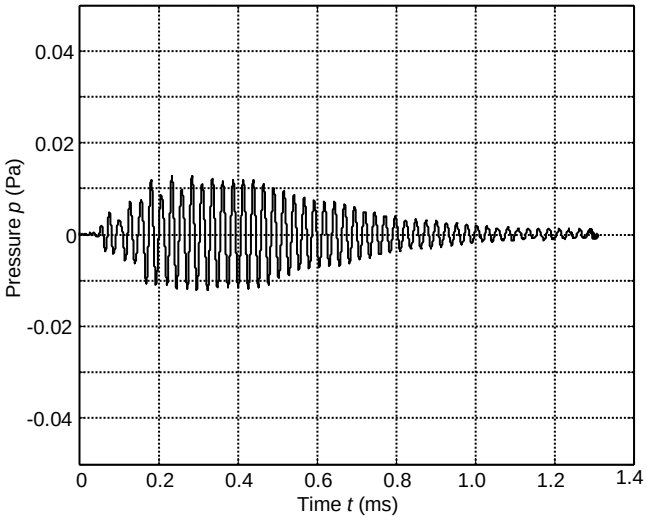

b

Fig. 3.4.6. Acoustic pressure pulses in air at a distance of 1 mm from the transducer measured with the Brüel& Kjaer wideband 1/8" microphone: a – PMN-32% PT single crystal transducer, f_r = 36.7 kHz; b – the Murata MA40B7 transducer, f_r = 37.9 kHz

Ultrasonic air-coupled transducers operating in a low frequency range were developed and investigated both in the transmitter and receiver modes. For that purpose, the transverse extension mode of the crystals is the most efficient option to be used. The principle of measurement is shown in Fig. 3.4.7, *a*. The transducer with the matching strip λ/4 was excited by the burst of 50 periods with the frequency f_r =

41.5 kHz at a distance of 1 mm. The waveform of the received signal is presented in Fig. 3.4.7, *b*.

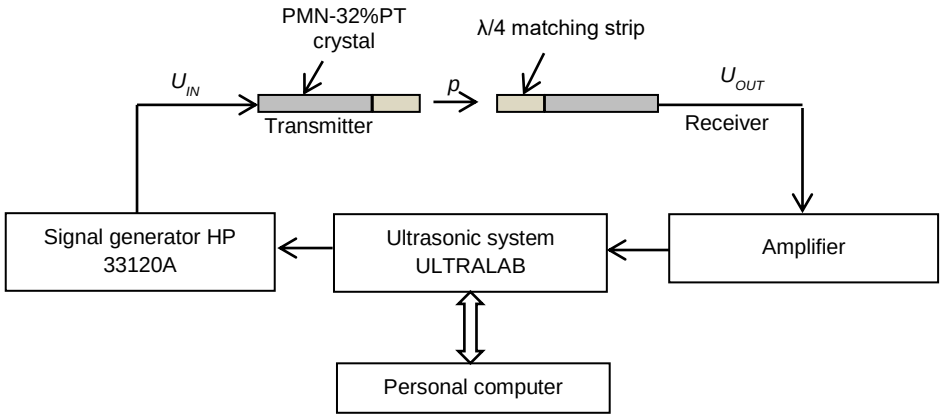

a

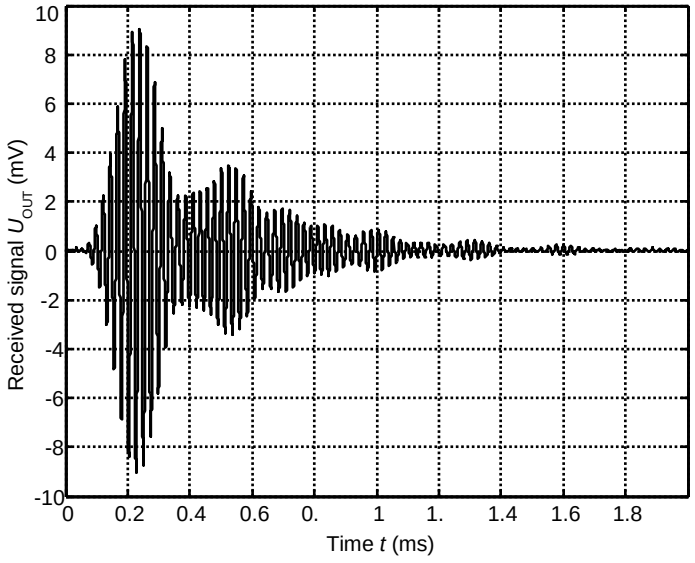

b

Fig. 3.4.7. Measurement of transduction losses:
a – experimental setup, b – the received signal at a distance of 1 mm

The peak-to-peak excitation voltage was set at U_{pp} = 0.5 V and excited by a burst of 50 periods. The developed transducer possesses transduction losses k = – 13.5 dB with the frequency f_r = 41.5 kHz at a distance of 1 mm, the transduction losses are k = – 30.4 dB at a distance of 100 mm; the excitation voltage was set to U_{pp} = 5.6 V. The transducer transduction losses were calculated according to the following formula:

$$k = 10 \log \frac{U_{OUT}}{U_{IN}}, \qquad (3.4.1)$$

where U_{IN} is the excitation voltage, U_{OUT} is the receiver voltage.

From the simulation results obtained by using the impulse response method (IRM), it follows that the transduction losses is – 34 dB at a distance of 100 mm. ~10% mismatch between the analytical simulation and the measurement results was observed.

3.5. Conclusions

1. The most prominent displacements take place in *x*0*y* plane of the crystal plate, e.g. in *x* (1) when k_3j = 1.2 μm/V and *y* (2) when k_3j = 2.3 μm/V directions. In order to determine on which edge the most prominent displacements are obtained, absolute measurements of the displacements at main resonance frequency f_{r2} of transverse extension mode (TE) were performed with the laser interferometer POLYTEC OFV-5000. In order to estimate the spatial distribution of the normal displacements of the PMN-32%PT single crystal elements were performed.
2. The high transformation coefficient k_{32} = 4.9 ÷ 5.1 μm/V of the transverse extension mode of the PMN-32%PT crystals allows them to be applied in the new type of air-coupled ultrasonic transducers. It justifies the selection of PMN-32%PT piezoelectric strips with the dimensions of (15 x 5 x 1) mm^3 as the active elements for air-coupled ultrasonic transducers.
3. The performance of air-coupled transducers may be significantly enhanced by using PMN-32%PT single crystals vibrating in the transverse extension mode as active elements. The application of this mode enables us to achieve operation frequencies lower than 1 MHz. Such frequencies are usually used in various air-coupled applications.
4. What concerns radiation, the edge of the crystal plate is employed. For further performance improvement, strip-like thin matching elements made of low acoustic impedance materials (such as polystyrene foam) may be used.
5. The matching elements improve not only the efficiency but also the bandwidth of the transducer and the radiated pulse waveforms as well. The developed transducer is denoted by transduction losses k = –13.5 dB with frequency f_r = 41.5 kHz.

4. DEVELOPMENT AND INVESTIGATION OF AIR-COUPLED ULTRASONIC ARRAY

PMN-32%PT crystals are already used in very high frequency ultrasonic phased arrays for medical applications, in ultrasonic transducers for non-destructive testing and for ultrasonic hydrophones. The application of the PMN-32 %PT crystals for air-coupled ultrasonic arrays is suggested in the present chapter. However, to the best of our knowledge, PMN-32%PT piezoelectric elements have not yet been systematically investigated from the point of view of their application for air-coupled ultrasonic arrays. For the improvement of performance, special acoustic matching elements made of low acoustic impedance plastics were bonded to the active edge of the crystal. The aperture used for radiation of ultrasonic waves in this case is rather small; therefore, in order to improve the directivity, an ultrasonic array consisting of 8 strips – like with PMN-32%PT elements – was proposed. The ultrasonic array was assembled from individual piezoelectric strips separated by insulating elements. In this case, a bigger rectangular aperture of the transducers is obtained.

The objective of this chapter is the development of wide band air-coupled ultrasonic arrays with improved performance achieved by using PMN-32%PT crystals.

4.1. Design of the PMN-32%PT of the air-coupled array

In order to achieve a more uniform distribution of the displacements on the active surface used for the radiation of ultrasonic waves, PMN-32%PT single crystals with the dimensions of (15 x 15 x 1) mm^3 were cut into narrower strips with the dimensions of (15 x 5 x 1) mm^3, and for the radiation of ultrasonic waves, the edge perpendicular to the direction *y* (2) was selected. The ultrasonic array (Fig. 4.1.1) consisting of eight PMN-32%PT crystal strips (15 x 5 x 1) mm^3 was thus produced.

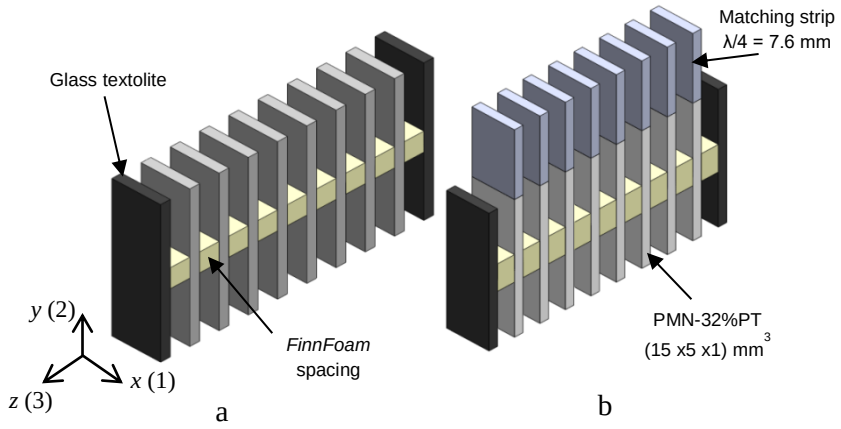

Fig. 4.1.1. Air-coupled ultrasonic array: a – without matching strips; b – with the matching strips

The PMN-32%PT crystal strips (15 x 5 x 1) mm^3 with the λ/4 matching strips operating in the transverse extension mode was developed. The λ is the wave length of the ultrasonic wave in the strip at the operation frequency of the ultrasonic transducer which is calculated according to the following formula:

$$\lambda = \frac{c}{f}; \tag{4.1.1}$$

where c is the ultrasonic velocity and f is the frequency. The pitch between individual elements of the array was selected slightly less than $\lambda_a/2$, where λ_a is the wave length in air at the operation frequency. The necessary distance between particular array elements is maintained by spacing elements. The spacing elements are made of *FinnFoam* material with the dimensions of (2 x 3 x 5) mm^3. They enable to minimize the acoustic cross-talk between piezoelectric elements in the array.

The application of phased arrays provides a possibility to control electronically the radiated ultrasonic field in air. In order to improve the performance of the array, piezoelectric elements with matching strips are used.

The ultrasonic air-coupled array consists of the upper cover, the housing, the piezoelectric array, the printed circuit board (PCB), the bottom cover and the electric connector. The views of the array are presented in Fig. 4.1.2 and Fig. 4.1.3.

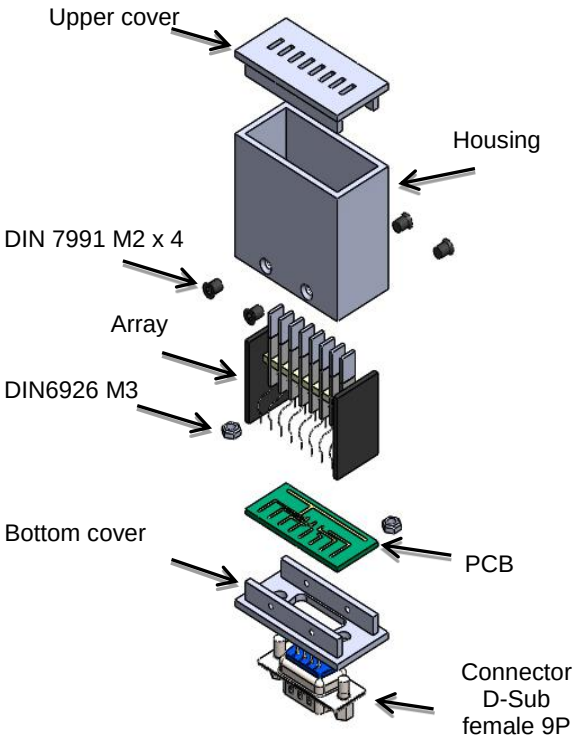

Fig. 4.1.2. Disassembled image of the air-coupled array

The upper cover was made of Polyethylene terephthalate PET plastic (produced by UAB "Plastena"). It is mechanically solid, rigid and solid plastic bearing high mechanical loads and pressure. This plastic features very low and stable friction coefficient, thus its wear-cycle is longer if compared to polyamide (PA) or polyacetal (POM). In comparison to polyacetal, PET plastic may work under higher temperatures and is more resistant to various acids. It does not absorb moisture; thus the stability of dimensions is retained during the process of production. The density of the employed material is 1.38 g/cm^3, its operating temperature ranges from +20 °C to +115 °C, the short term operating temperature may go up to +180 ^{o}C, and the moisture absorption is less than 0.3 %. The upper cover was overlaid with a metallized film. It is used for the shielding of external electromagnetic fields.

The housing of the ultrasonic air-coupled array is made of 1 mm-thick aluminium.

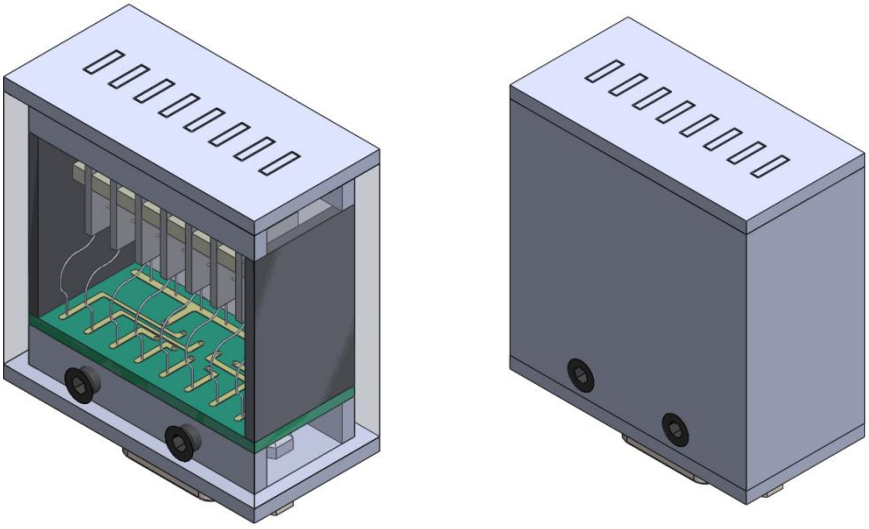

a b

Fig. 4.1.3. Air-coupled ultrasonic multi-elements array:
a – transparent view; b – external view

The printed circuit board (PCB) was made at Professor Kazimieras Baršauskas Ultrasound Institute of Kaunas University of Technology. The bottom cover was made of aluminium, and the connector was D-Sub female 9P.

The air-coupled array had the following external dimensions: the width of 20 mm, the height measuring 48.64 mm and the length of 40 mm.

4.2. Investigation of vibrations of air-coupled ultrasonic array by FEM

The air-coupled array was modelled by using the ANSYS software. The volume of the piezo-element was meshed by using SOLID5, FLUID30, FLUID130 and SOLID45 elements. The presented model visualizes its 3D structure. The simulation

takes into account free boundary conditions and the coupling between electric and mechanic fields. The piezoelectric element has 8 nodes with four nodal degrees of freedom *x* (1), *y* (2), *z* (3) directions and electric voltage *U*. The electric excitation voltage was U_{pp} = 1V when excited by a long harmonic pulse. The 3D model is presented in Fig. 4.2.1.

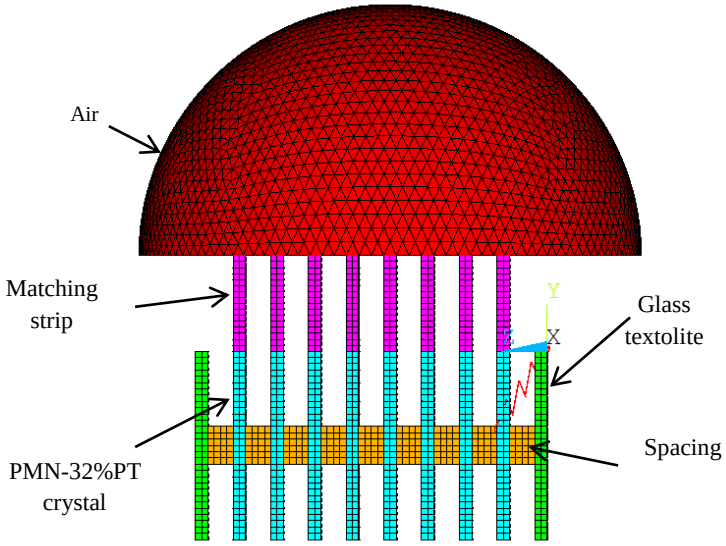

Fig. 4.2.1. The 3D model of the air-coupled array

Finite elements modelling (FEM) was performed in order to obtain better understanding of the spatial distribution of mechanical displacements. The front surfaces of the air-coupled ultrasonic array were using the radiation of ultrasonic fields in the air. The simulation results showed the best location to fix the piezo-elements in the construction. The best area to fix them was found to be in the centre of the piezo-element because the mechanical displacement of a piezo-element is zero. The material and construction of the gaskets between the PMN-32%PT crystal strips was selected to minimize the acoustical cross-talking between piezoelectric elements.

The spatial distribution of the displacement modulus in direction *y* (2) in the array elements at two different frequencies f_{r1} = 35.7 kHz and f_{r2} = 42.8 kHz corresponding to the two peaks in the frequency response of the array is presented in Fig. 4.2.2 *a* and *b*. We should note that the displacements in Fig. 4.2.2 for better clarity are increased by $6 \cdot 10^4$ times. The amplitude scale is shown on the right in micrometres. The colour scale depicts the amplitude of spatial distributions of mechanical displacements in PMN-32%PT crystal elements. The red and blue colours correspond to the maximal values of spatial distributions of the displacement modulus.

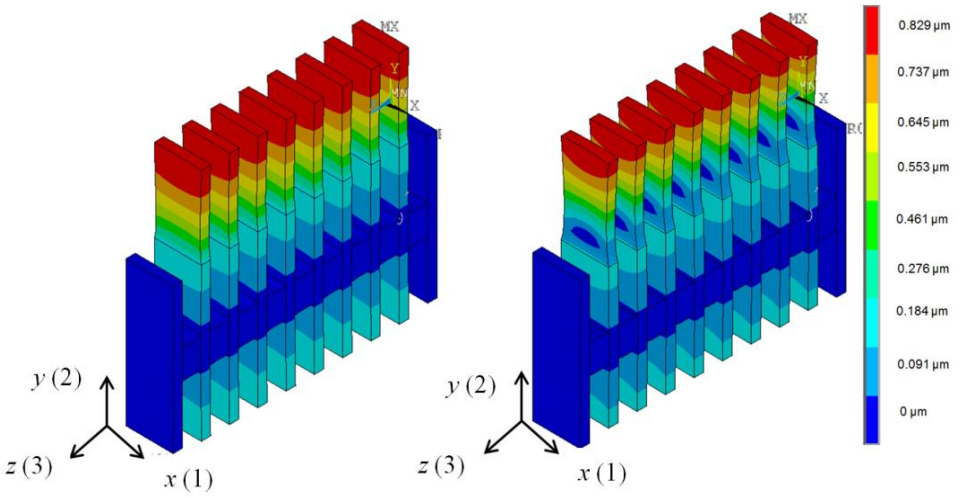

Fig. 4.2.2. Spatial distribution of displacements of the air-coupled array: a – f_{r1} = 35.7 kHz; b – f_{r2} = 42.8 kHz; c – excited No. 5 element

For the spatial distribution of the displacement modulus in direction y (2) in the array elements at frequency f_r = 42.8 kHz when excited, only element No. 5 is presented in Fig. 4.2.3. The simulated frequency responses of the PMN-32%PT mechanical displacements and acoustic pressure in the air of the air-coupled array are presented in Fig. 4.2.4 and 4.2.5.

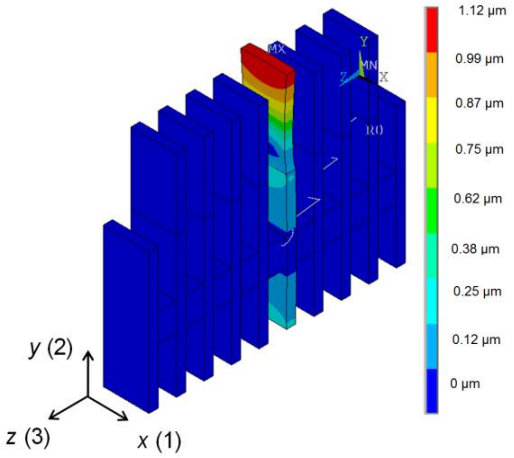

Fig. 4.2.3. Spatial distributions of the displacements of the air-coupled array when only No. 5 element is excited

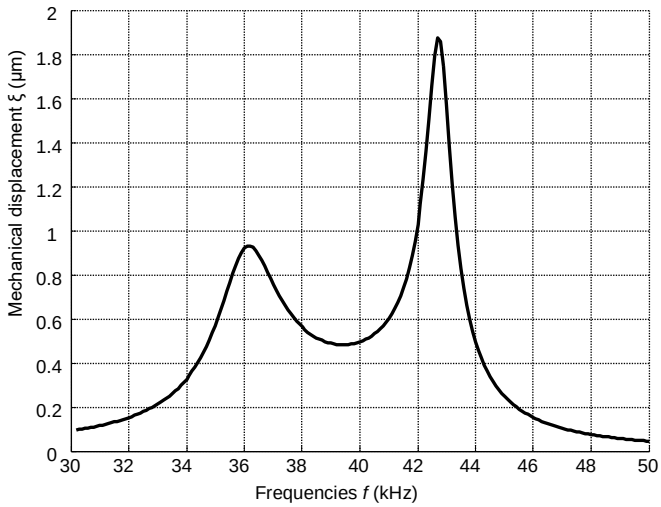

Fig. 4.2.4. Simulated frequency response of the PMN-32%PT mechanical displacements when only No. 5 element is excited

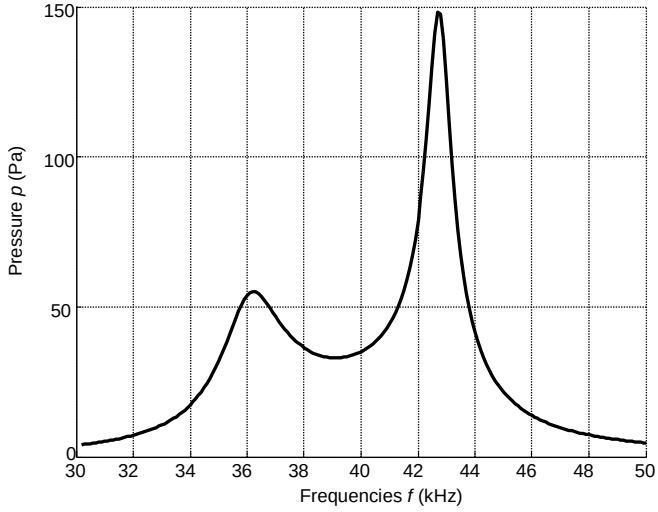

Fig. 4.2.5. Simulated frequency response of the PMN-32%PT acoustic pressure in the air when only No. 5 element is excited

The vibration and the acoustic field's motions of the piezoelectric element are shown in Fig. 4.2.6 and Fig. 4.2.8. The simulation results are presented in Fig. 4.2.7 and Fig. 4.2.9 where the solid line is the mechanical displacement and the pressure of element No. 4 whereas the dashed line is the mechanical displacement and the pressure of element No. 6 of the air-coupled ultrasonic array. The mechanical displacements are about 864 times smaller on elements No. 4 and No. 6 than on the excited element (No. 5). We should note that the displacements in Fig. 4.2.7 for

better clarity are shown in the nanometre scale. The excitation voltage was U_{pp} = 1 V by long harmonic pulse. In order to estimate the level of cross-talks between the neighbouring array elements, simulation of mechanical displacements of the radiating surfaces of a few neighbouring elements was performed when only one element (No. 5) was excited in the array. The simulation showed that vibrations and the acoustic pressure of the individual elements in the array are very close to the corresponding responses of the PMN-32%PT single element with (15 x 5 x 1) mm^3 dimensions.

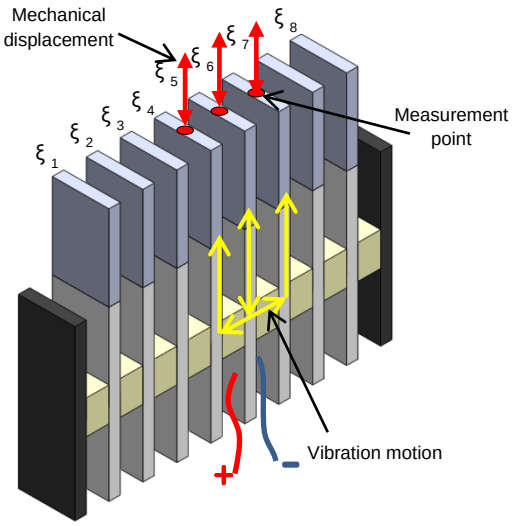

Fig. 4.2.6. Vibration motion

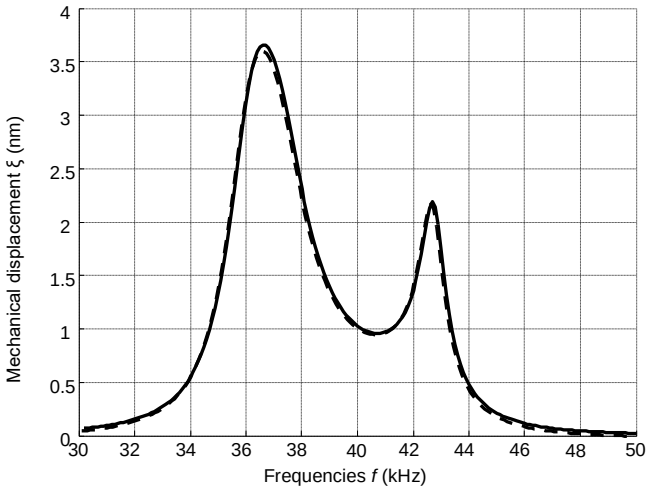

Fig. 4.2.7. Simulated frequency responses of the mechanical displacements when No. 5 element is excited. The solid line represents element No. 4 and the dashed line outlines element No. 6

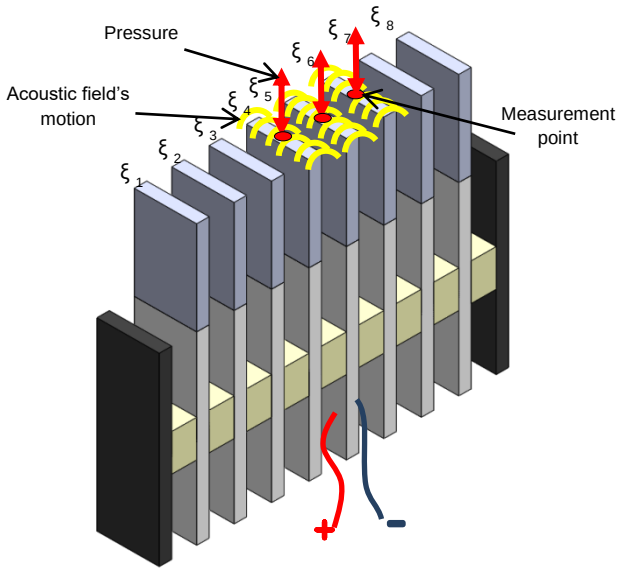

Fig. 4.2.8. Acoustic field's motion

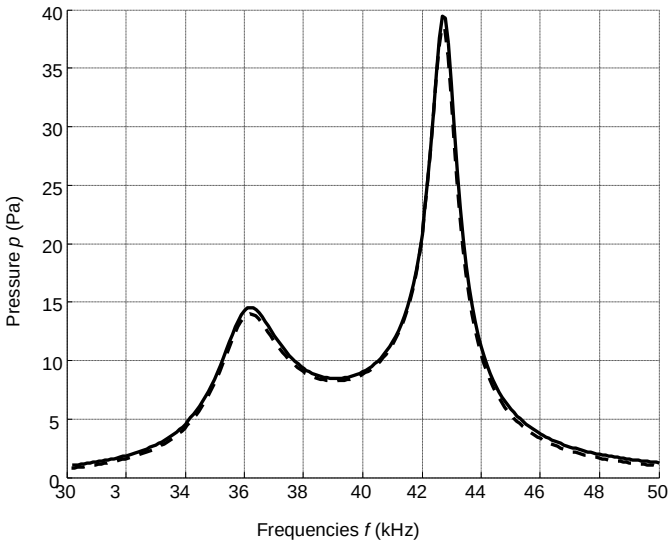

Fig. 4.2.9. Simulated frequency responses of the acoustic pressure in the air when No. 5 element is being excited. The solid line represents element No. 4 whereas the dashed line shows element No. 6

Frequency responses of the ultrasonic array with the matching strip λ/4 when all the elements are excited are shown in Figs. 4.2.10 and 4.2.11 where the solid line represents the frequency responses of the array with the matching strip, the width of which is w = 1 mm whereas the dashed line corresponds to the width of w = 3 mm. The frequency responses of the array depend on the thickness of the matching strips.

In the case of the thick matching strip (w = 3 mm, Figs. 4.2.10 and 4.2.11), the frequency response becomes more non-uniform in comparison to the matching strip thickness of which w = 1 mm is the same as the thickness of the piezoelectric element. Please note that Fig. 4.2.10 and Fig. 4.2.11 show mechanical displacements and the acoustic pressure in the air when all the elements are excited in the air-coupled ultrasonic array.

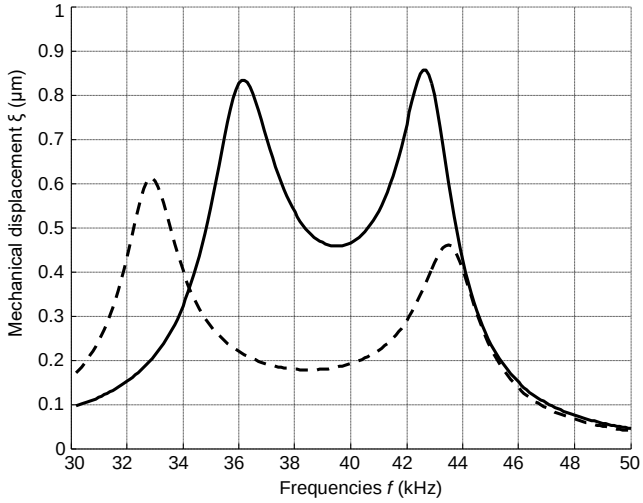

Fig. 4.2.10. Simulated frequency responses of the mechanical displacements by the ultrasonic array with the matching strip λ/4.
Solid line: w = 1 mm and dashed line: w = 3 mm

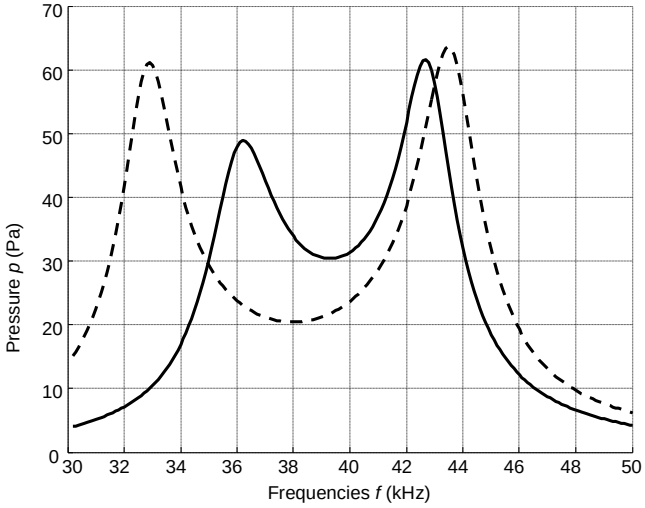

Fig. 4.2.11. Simulated frequency responses of the acoustic pressure radiated by the ultrasonic array with the matching strip λ/4.
Solid line: w = 1 mm and dashed line: w = 3 mm

The frequency responses of the mechanical displacements of the active surface and of the acoustic pressure in the air for the ultrasonic array without the matching strip and with the matching strip (AIREX R90.200) are presented in Fig. 4.2.12 and Fig. 4.2.13, respectively. In both cases, the output electric impedance of the electric generator was $R_g = 5\ \Omega$.

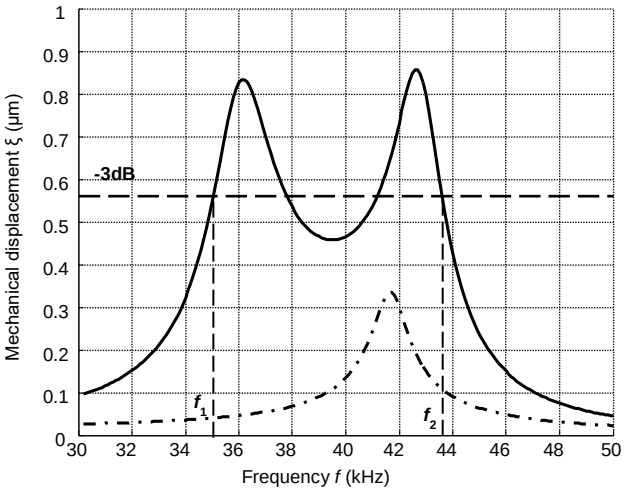

Fig. 4.2.12. Simulated frequency responses of mechanical displacements. Solid line depicts the case with the matching strip λ/4 (w = 1 mm) whereas the dot-dashed line shows the values obtained without the matching strip

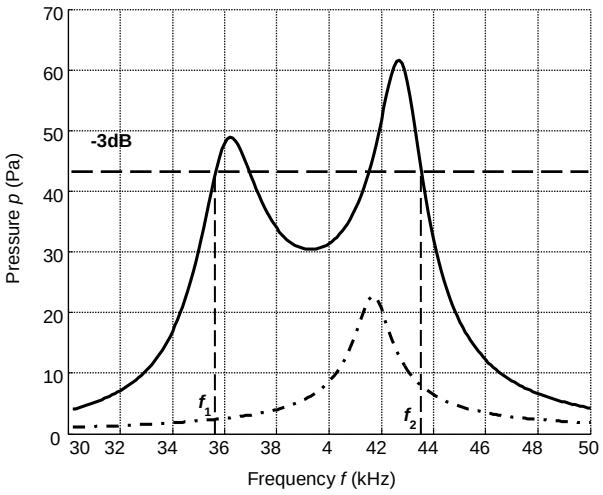

Fig. 4.2.13. Simulated frequency responses of the acoustic pressure in air. The solid line shows the values for the matching strip λ/4 (w = 1 mm) whereas the dot-dashed line depicts the case without the matching strip

From the simulated results, it follows that the best performance of the air-coupled ultrasonic transducer in terms of bandwidth and transduction losses is

obtained with the λ/4 thin (w = 1 mm) matching strip made of plastic AIREX R90.200.

In all the cases, the most prominent displacement took place on the active surfaces of the matching strips which are used for the radiation of ultrasonic waves. The bandwidth of the air-coupled ultrasonic array is from 35 kHz to 45 kHz. The displacements of the opposite end of the piezoelectric strips are almost 9 times smaller.

4.3. Impulse response method (IRM) for rectangular apertures

The performance of the air-coupled ultrasonic array may be evaluated by analysing ultrasonic fields radiated into the surrounding air. For the calculation of such fields, numerical, e.g. finite elements and analytical methods are used [113 – 115]. We selected the impulse response method (IRM) for the calculation of the acoustic pressure generated by the array of rectangular pistons. For this purpose, the open source software tool *The Lamb Matlab Toolbox* was used. The *Matlab* software is based on the PhD Thesis presented in [116 – 117].

This is a natural extension of the method for predicting the pressure field from a rectangular source by using the impulse response method (IRM) which is extended further for a phased array [118 – 123].

The software tool was adopted in terms of the excitation signal generation, transducer geometry calculation, excitation and the radiation zone coordinate points calculation. A new set of functions was devised for the visualization of the acoustic pressure for the air-coupled array.

From the classical theory of sound, instantaneous pressure $p(\vec{M},t)$ in an ultrasonic field can be expressed as (4.3.1) [117]:

$$p(\vec{M},t) = \rho_0 \frac{\partial \phi}{\partial t}(\vec{M},t); \tag{4.3.1}$$

where ρ_0 is the density, $\phi(\vec{M},t)$ is the velocity potential related to particle velocity $\vec{V}(\vec{M},t)$ obtained from Equation 4.3.2:

$$\vec{V}(\vec{M},t) = -\vec{\nabla}\phi(\vec{M},t). \tag{4.3.2}$$

Let us consider a transducer with a rectangular aperture 2b long and 2a wide where $a \leq b$ and which is located on $z_0 = x0y$ plane. The aperture of the transducer is divided into four quadrants S_1, S_2, S_3 and S_4 (Fig. 4.3.1).

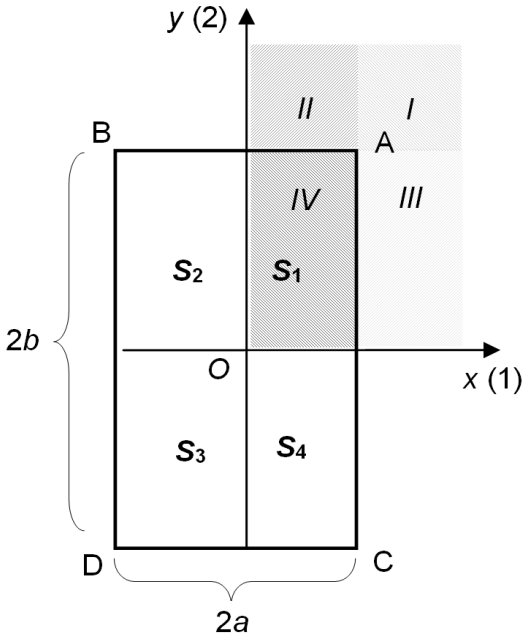

Fig. 4.3.1. The rectangular piston zones

The geometry and coordinate system for the impulse response of a rectangular piston is presented in Fig. 4.3.2.

Fig. 4.3.1 shows the first quadrant $S_1$with its four regions (I, II, III, IV) with distances d_i, where i = 1, 2, 3 and 4, point P'(x, y, 0), projection of P (x, y, z) on the radiator plane form straight lines which are the sides of the rectangular piston [116 – 117]. The analytical expression of $h(\bar{x},t)$ is defined by employing Eq. 4.3.3:

$$\begin{aligned} &\textit{Region I} = x \geq a,\ y \geq b, && d_1 = x - a, \\ &\textit{Region II} = x < a,\ y \geq b, && d_2 = y - b, \\ &\textit{Region III} = x \geq a,\ y < b, && d_3 = x + a, \\ &\textit{Region IV} = x < a,\ y < b, && d_4 = y + b. \end{aligned} \tag{4.3.3}$$

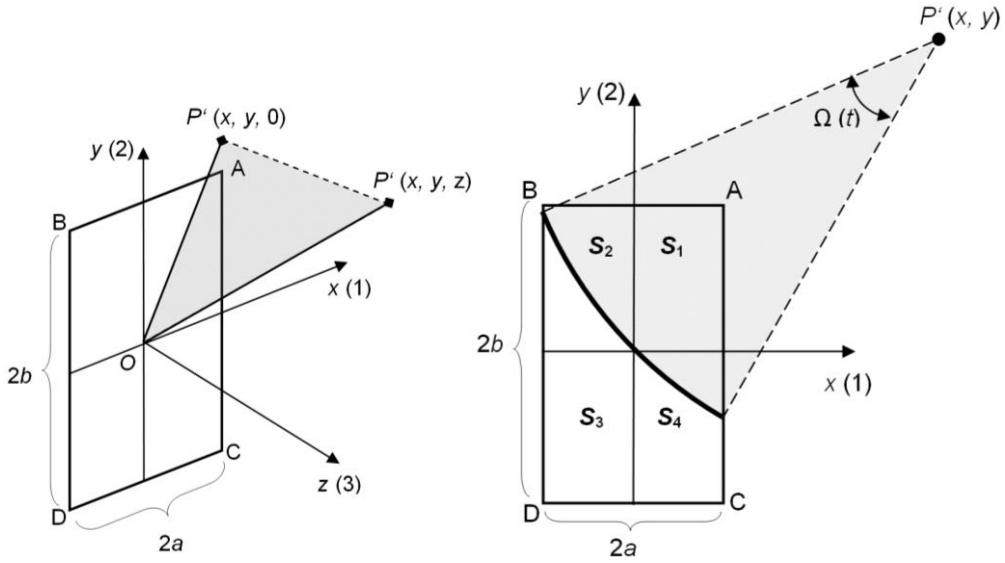

Fig. 4.3.2. The geometry and coordinate system of a rectangular piston

The time instant at which the upcoming sphere touches the surface for the first time at t is:

$$t = \frac{z}{c}. \tag{4.3.4}$$

It may thus be concluded that the impulse response (IR) function h (P, t) is a time-limited function restricted to the time interval for regions *I*, *II*, *III* and *IV*, respectively:

$$h(P,t) = c \cdot \frac{\beta(z,t)}{4\pi} \cdot \Omega(P',t). \tag{4.3.5}$$

Obliquity factor β depends on the boundary conditions. For rigid, soft and free field boundary conditions, the obliquity factor is given in the time domain by employing Eq. 4.3.6:

$$\beta(z,t) = \begin{cases} 2, & \text{rigid baffle,} \\ 2z/(ct), & \text{soft or pressure release baffle,} \\ 1+[z/(ct)], & \text{free field.} \end{cases} \tag{4.3.6}$$

The pressure field at a given point P is found from impulse response h (P, t) and vibration velocity v_i (t) of the radiating aperture:

$$p(P,t) = \rho \frac{\partial v(t)}{\partial t} * h(P,t). \tag{4.3.7}$$

The whole acoustic field radiated by the array is obtained as a sum of fields p_i radiated by individual elements:

$$p(P,t) = \sum_{i=1}^{N} p_i(P,t); \tag{4.3.8}$$

where N is the number of elements in the array. It means that for the calculation of the acoustic fields in air, vibration velocities v_i (t) of all the radiating rectangular apertures are required.

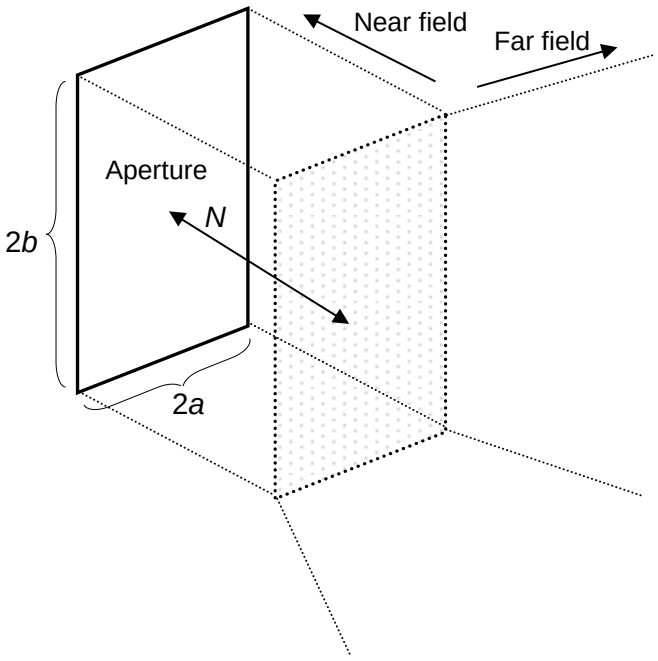

Fig. 4.3.3. The near and far fields of the air-coupled array

The near and far fields of the air-coupled array are shown in Fig. 4.3.3. The near field of the analysed array is according to Eq. 4.3.9 [120 – 121]:

$$N_{rc} = \frac{2a * 2b}{\pi * \lambda_0} = \frac{2a * 2b}{\pi * \frac{c}{f}} = 21.1\text{mm}; \tag{4.3.9}$$

where a is the width of the air-coupled array, b is the lenght and λ_0 is the sound wave length in the air at operation frequency f_{vid} = 47.91 kHz.

It means that the efficient focusing of radiated acoustic fields at such low frequencies may be achieved at short distances, e. g. up to 21 mm.

4.4. Experimental investigation of a multi-element ultrasonic array

For the calculation of acoustic fields by employing the impulse response method, it is necessary to know the vibration velocities of the radiating surfaces of the array's elements, which for different elements may be different.

The laser interferometer method (Fig. 4.1.1, *a*) is applied for the measurement of the vibrations velocities of air-coupled ultrasonic arrays (Fig. 4.1.1, *b*). The housing of the ultrasonic air-coupled array is presented in Fig. 4.1.1, *c*. By using the measured data, we can simulate the radiated acoustic fields in the air of the air-coupled ultrasonic array with the *Matlab* software.

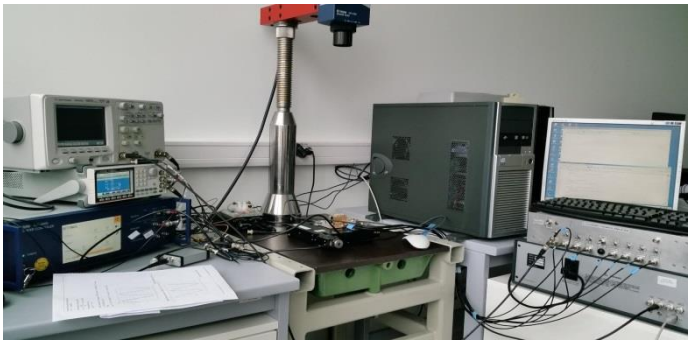

a

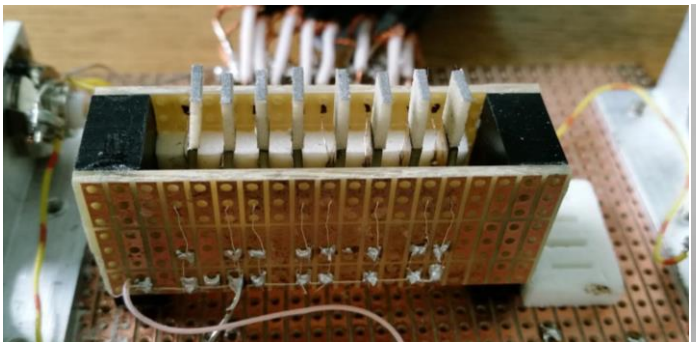

b

c

Fig. 4.4.1. a – the laser interferometer method stand; b – air-coupled array; c – the assembled air-coupled array

The experimental setup consists of the laser interferometer POLYTEC OFV – 5000, the generator AFG-3051, the oscilloscope Agilent DSO5023A and the main device Dasel SITAU 32:128:2 LF TR with an 8-channel power amplifier (Fig. 4.4.2).

The measurements results of the PMN-32%PT vibration velocities and mechanical displacements are shown in Table 4.4.1.

Mechanical displacements ξ of the PMN-32%PT air-coupled array were measured with a laser interferometer. The air-coupled array frequency was set at f_{vid} = 37.91 kHz. Each element of the air-coupled array was adjusted individually.

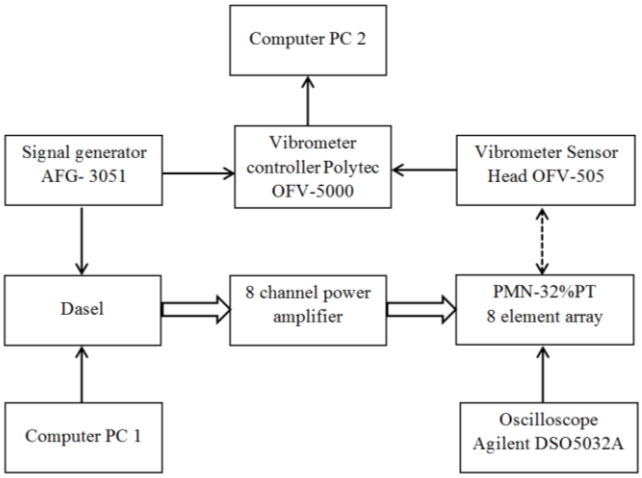

Fig. 4.4.2. Experimental setup for the investigation of velocities in the air-coupled ultrasonic array

Table 4.4.1. Measurement results based on the employment of laser interferometer

R_g = 50 Ω	Displacement amplitude A (nm)	Vibration velocity v (m/s)	Excitation voltage amplitude U_A (mV)	Normalized displacement A/U_A (μm/V)	Normalized vibration velocity v/U_A (m/s/V)
No. 1	40	0.0095	70	0.57	0.1358
No. 2	40		70	0.57	0.1358
No. 3	40		70	0.57	0.1358
No. 4	40		70	0.57	0.1358
No. 5	40		90	0.44	0.1048
No. 6	40		70	0.57	0.1358
No. 7	40		75	0.53	0.1262
No. 8	40		100	0.40	0.0953

Excitation voltage amplitude U_A was set at such a level that it enabled us to get the displacement amplitude of A = 40 nm. The measurement results are shown in Fig. 4.4.3. The solid line corresponds to the 8 elements of the array whereas the dashed line visualizes the 9 spaces between the PMN-32%PT elements. The mechanical displacements of the connection spaces between the elements are approximately 0.04 – 0.05 μm/V. It is 20 times smaller than that of the elements of the air-coupled array. No. 5 and No. 8 elements of the array exhibit less prominent mechanical displacement than others. It was concluded that it may stem from slightly different resonant frequencies of the piezoelectric elements. The output electric impedance of the electric generator was R_g = 50 Ω.

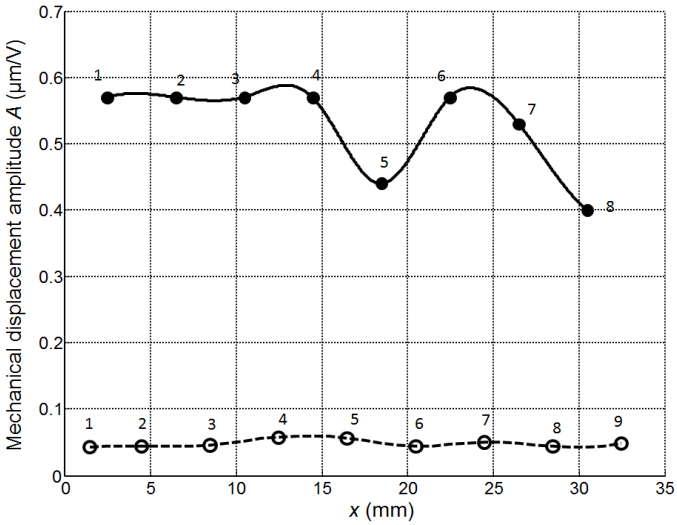

Fig. 4.4.3. The amplitude of the mechanical displacements of the air-coupled array. The numbers on the curves are the numbers of the array elements.
The solid line shows the elements (1 – 8);
The dashed line demonstrates the spaces between elements (1 – 9)

The measurement results of the vibration velocities of the radiating surfaces of the developed array will be used for the modelling of the radiated acoustic fields when employing the impulse response (IR) method. The simulation results are presented in Subchapter 4.5.

4.5. Simulation results of radiated acoustic fields

The impulse response method (IRM) was chosen for the simulation of the radiated acoustic fields created by the vibrating air-coupled array. The air-coupled array consists of 8 narrow rectangular strips with the dimensions of (15 x 5 x 1) mm^3 and the 3.0 mm spaces between the elements. The surfaces of the narrow strips radiate a particle velocity pulse of 5 cycles with the sinus type envelope and 1 m/s amplitude (Fig. 4.5.1). The main frequency is f_{av} = 37.91 kHz with the 20 – 80 kHz limited bandwidth. The spatial distribution of the radiated acoustic fields at the air-coupled array was calculated for the two cases. In the first case, the signal delays for emitting air-coupled array elements were not involved; an unfocused beam was observed. In the second case, the signal delays for emitting air-coupled array elements were used; a focused beam was observed. The signal delays graph is shown in Fig. 4.5.2; it is used for the focused beam.

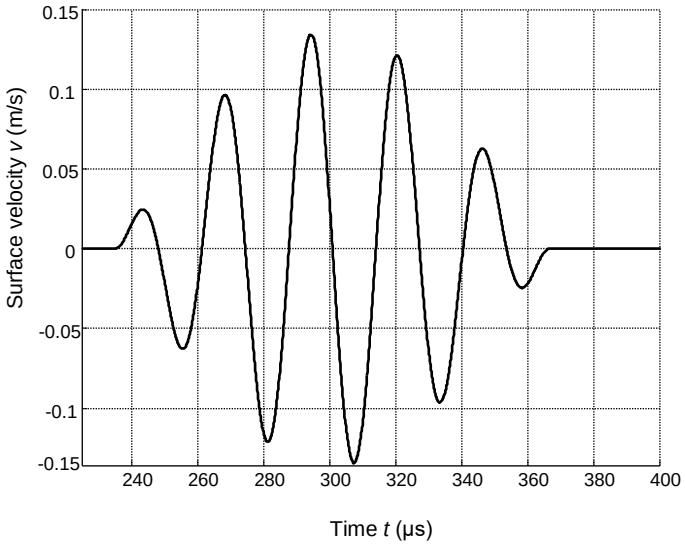

Fig. 4.5.1. Surface velocity signal of the air-coupled array

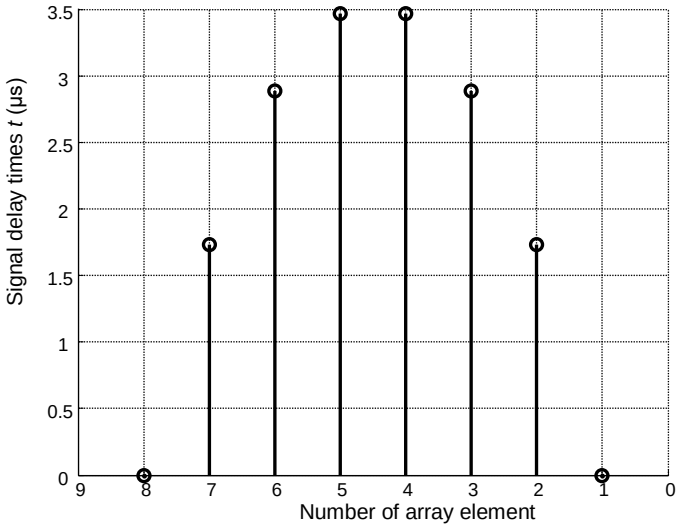

Fig. 4.5.2. Signal delays and emission of air-coupled elements

The structure of the air-coupled array pressure field changes along the distance. Three zones constitute the investigated area: the near field, the intermediate field and the far field. The near field limit of the air-coupled array depends on the frequency. In our case for f_{av} = 37.91 kHz, the value is N_{rc} = 21.1 mm. Taking into account the 37.91 kHz frequency, the six distances at which spatial distributions of the acoustic fields were calculated were chosen as follows: 1 mm for the near field; 20 mm for

the intermediate field; 40 mm, 60 mm, 80 mm and 100 mm for the far field (Fig. 4.5.3).

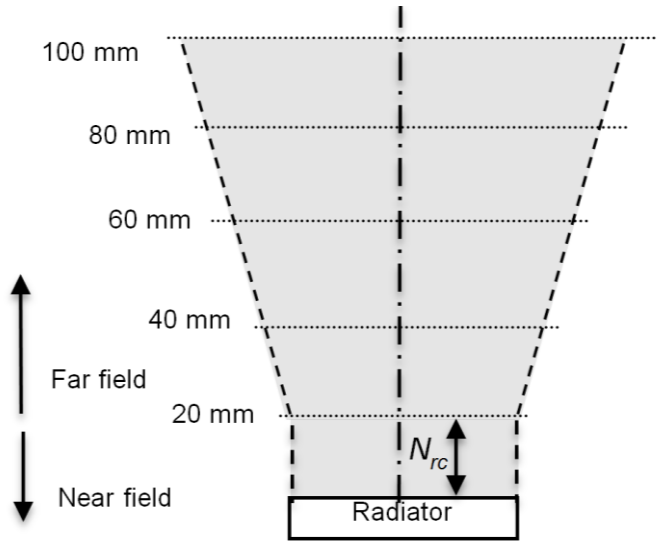

Fig. 4.5.3. The distances at which spatial distributions of the acoustic fields were calculated

By selecting different delays for the excitation instants of different array elements, it is possible to focus or/and deflect the ultrasonic beam; deflection angle α of the air-coupled array was being changed in the range of ±20°.

The results of the simulation at the different distances 1 mm, 20 mm, 40 mm, 60 mm, 80 mm and 100 mm for unfocused and focused beams of the air-coupled array are shown in Fig. 4.5.4 and Fig. 4.5.5.

We should note that the spatial distributions of acoustic pressure k_{tr} are shown in different scales, and in this case not absolute p but rather the normalized value of the acoustic pressure is used:

$$k_{tr} = \frac{p}{U_{pp}}; \qquad (4.5.1)$$

where U_{pp} is the respect to the excitation voltage.

The simulation results showed that the focused beam is obtained at the intermediate field at a distance of 20 mm. The maximal normalized acoustic pressure is k_{tr} = 6 Pa/V in the unfocused beam and k_{tr} = 11 Pa/V in the focused beam, e. g. 1.8 times better than in the unfocused beam.

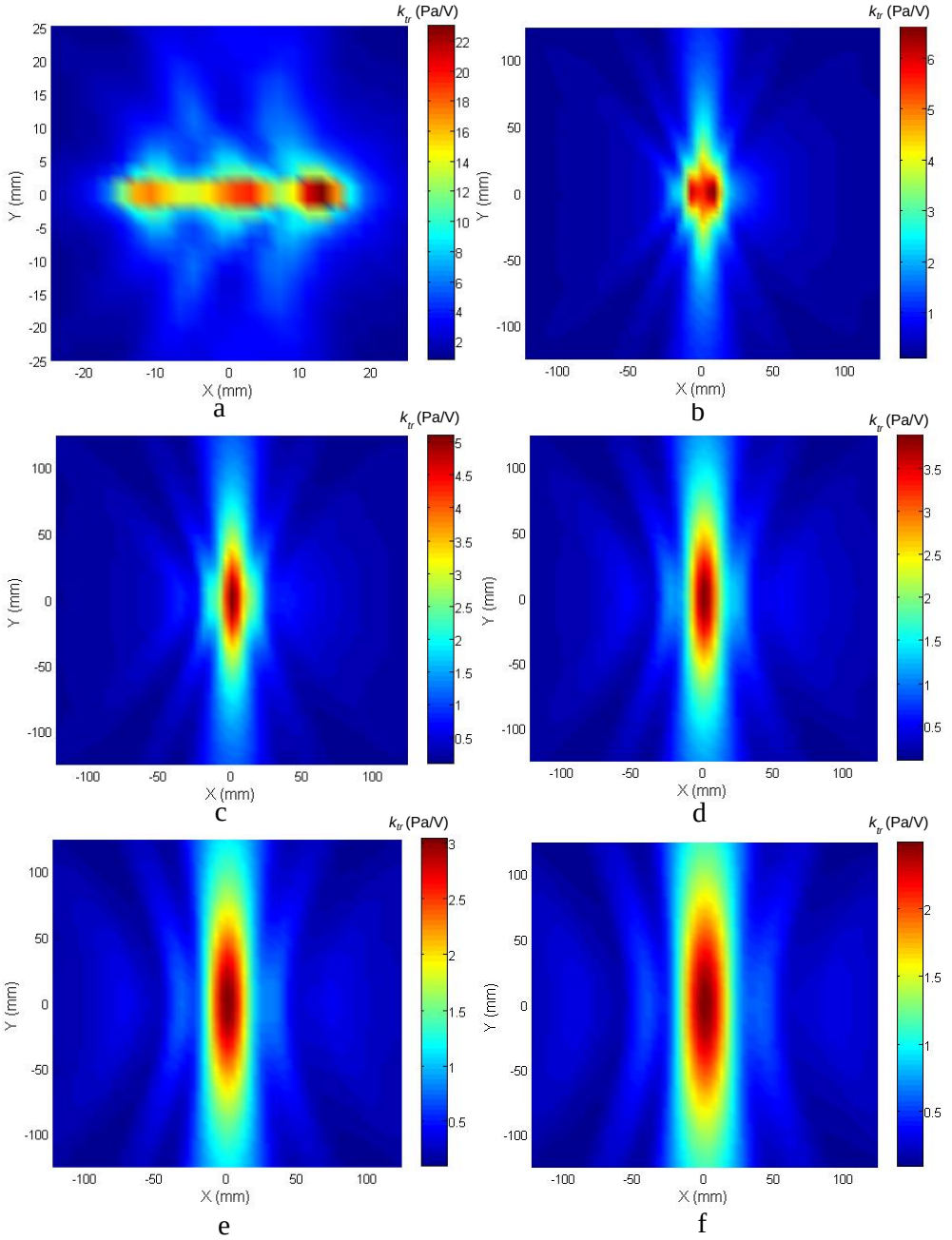

Fig. 4.5.4. The spatial distributions of normalized acoustic pressure k_{tr} in air in the case of unfocused beam: a – at 1 mm, b – at 20 mm, c – at 40 mm, d – at 60 mm, e – at 80 mm, f – at 100 mm distance

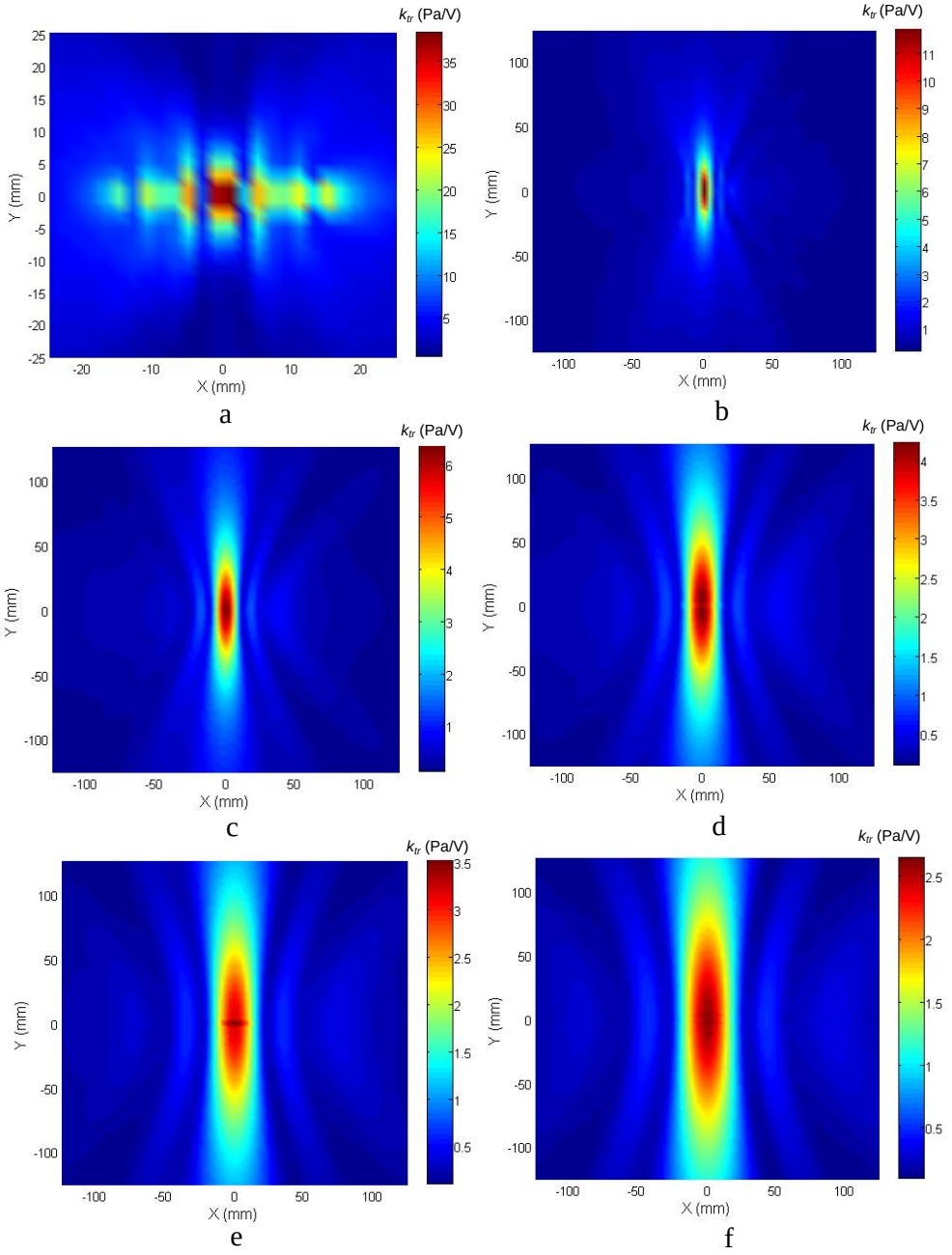

Fig. 4.5.5. Spatial distributions of the normalized acoustic pressure k_{tr} in the case of the focused beam: a – at 1 mm, b – at 20 mm, c – at 40 mm, d – at 60 mm, e – at 80 mm, f – at 100 mm distance

The normalized acoustic pressure in air at the distance of 80 mm from the array at different beam deflection angles was also simulated Deflection angle α of the air-

coupled array was changed from –20˚ to 20˚ at a step of 10˚. The simulation results are shown in Fig. 4.4.6.

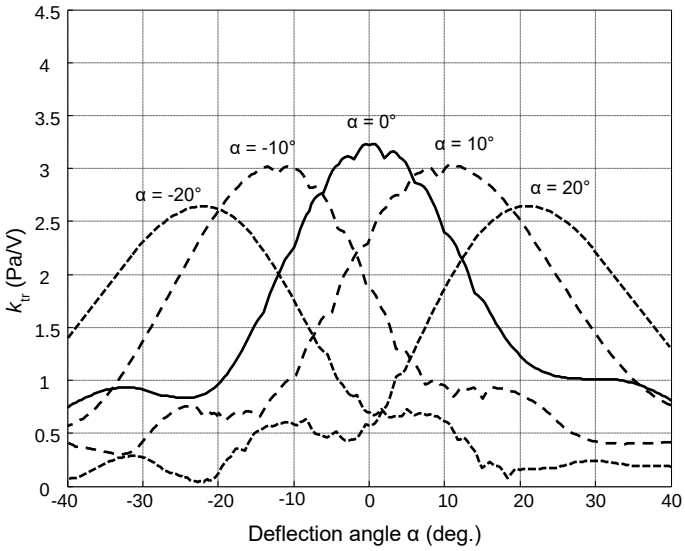

Fig. 4.4.6. Simulated normalized acoustic pressure distributions across the ultrasonic beam at a distance of 80 mm from the array at different beam deflection angles α

Such visualization enables us to obtain better estimates of the transduction efficiency of the array. The ultrasonic beam deflection simulated results show excellent beam steering possibilities in the range of ±20°.

4.6. Experimental investigation of radiated acoustic fields

Measurements of the acoustic pressure fields radiated by the developed air-coupled array were performed by the Brüel& Kjaer wide band 1/8" microphone. The measurements were performed at the distance of 1 mm from the radiating surface. The measurements were carried out by using the measurement setup which consists of the ultrasonic measurement system "ULTRALAB" (Baršauskas Ultrasound Research Institute) with the XYZ scanner, the 4138-type acoustic microphone with the measurement amplifier NEXUS WH 3219 (Brüel & Kjaer) and the 8-channel signal generator. The measurement system is shown in Fig. 4.6.1.

The three axes *X, Y, Z* scanner drives the B& K 4138 type microphone in space. The 8 elements of the developed array were excited by the 5 period burst of harmonic voltage from the multichannel signal generator.

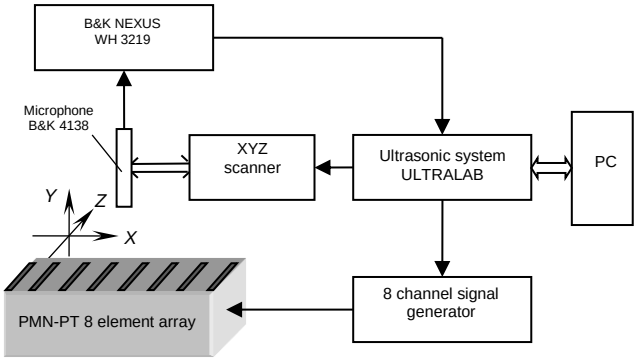

Fig. 4.6.1. The experimental setup for the investigation of ultrasonic fields radiated by the air-coupled ultrasonic array; PC – a personal computer.

During the experiments, the frequency response and the spatial distributions of the acoustic pressure across the ultrasonic beam in air were investigated (Fig. 4.6.2).

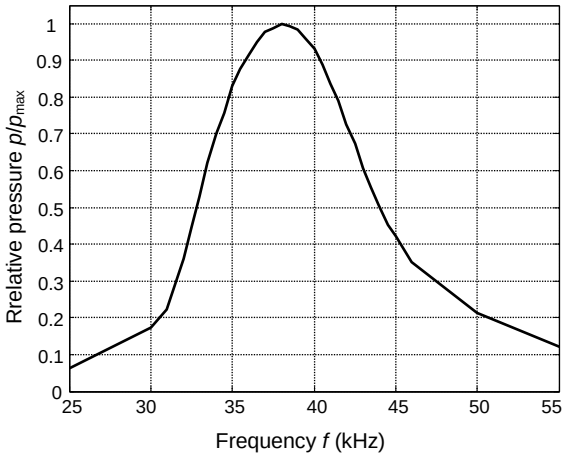

Fig. 4.6.2. The measured frequency response of acoustic pressure p radiated by the 8-element array with the matching strips at the distance of 80 mm

The frequency response was measured by placing the microphone on the symmetry axis of the array. Due to the interference of ultrasonic fields radiated by individual elements, the frequency response is rather smooth, and the achieved frequency bandwidth at the –6 dB level is $\Delta f_{0.5} = 0.3\, f_0$, e.g.; it is quite wide. Here, $f_{av} = 37.91$ kHz is the central frequency of the array. The measurement results of the acoustic pressure in the air in the case of the unfocused beam at the set of distances 1 mm, 10 mm and 80 mm from the array surface are presented in Fig. 4.6.3. We should note that in this case absolute p (Fig. 4.6.3, *a*, *b* and *c*) and the normalized value of acoustic pressure $k_{tr} = p/U_{pp}$ with respect to excitation voltage U is

presented in Fig. 4.6.3, *d*. B-scan along *Y* and X axes at the distance of 80 mm is presented in Fig. 4.6.3, *e* and *f*, where black lines show the width of the window.

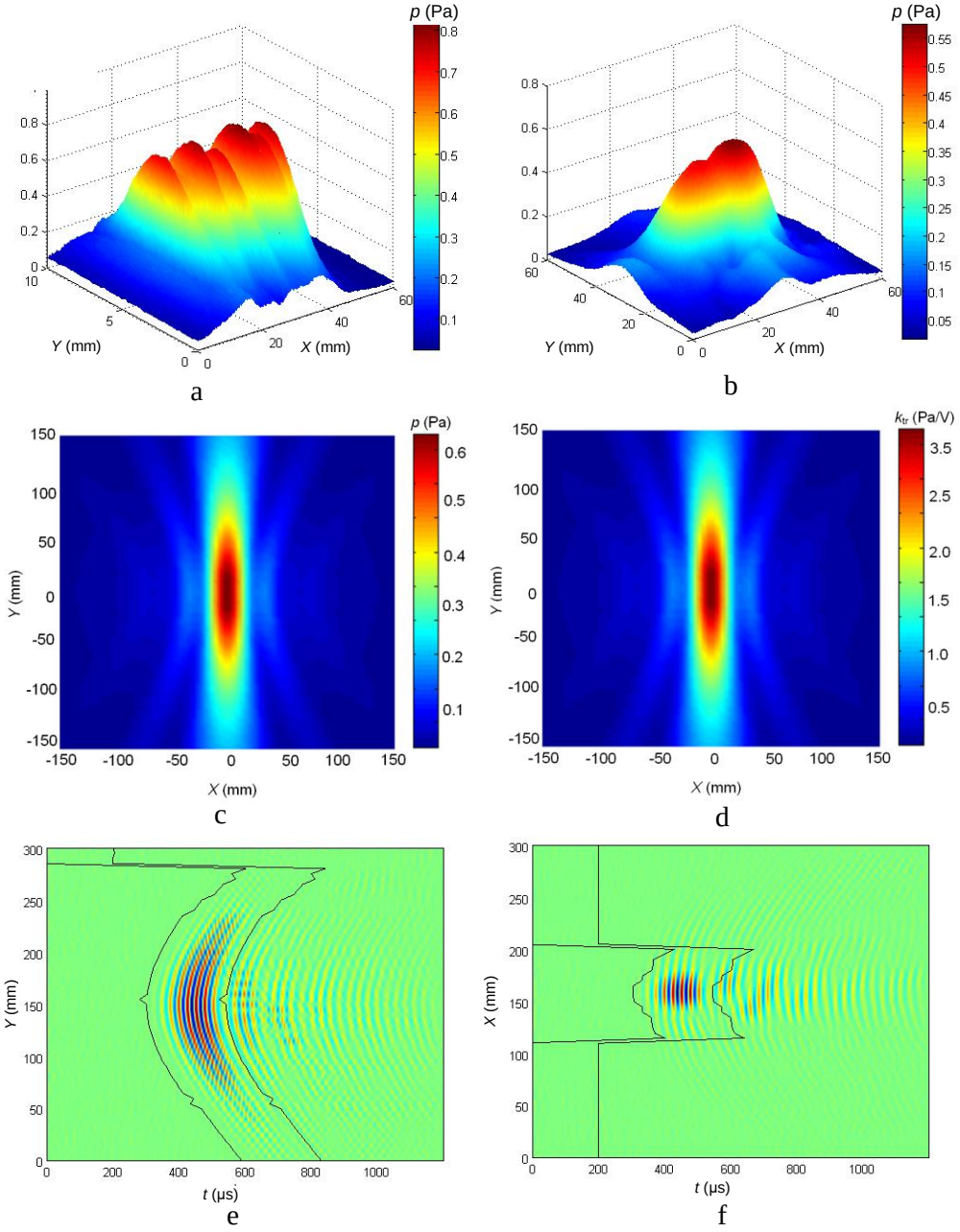

Fig. 4.6.3. Measured acoustic pressure in air in the case of the unfocused beam: a – at 1 mm, b – at 10 mm, c – at 80 mm at (absolute pressure *p*, Pa), d – at 80 mm (at normalized pressure k_{tr}, Pa/V), e – B-scan along *Y* axis at the distance of 80 mm, f – B-scan along *X* axis at the distance of 80 mm

The developed array was excited by f_{av}=37.91 kHz frequency 5-period burst with the peak to peak amplitude of U_{pp}=1 V. The measurement results of the radiated acoustic fields with the focused beam at different distances (10 mm and 40 mm from the array surface) are presented in Fig. 4.6.4. The measured delay times of piezoelectric elements are shown in Table 4.6.1.

Table 4.6.1. Measured delay times of piezoelectric elements

10 mm distance							
No. 1	No. 2	No. 3	No. 4	No. 5	No. 6	No. 7	No. 8
0 μs	7.8 μs	15 μs	19.3 μs	19.3 μs	16.1 μs	10.5 μs	1.4 μs
40 mm distance							
0 μs	2.3 μs	4.9 μs	6.4 μs	6.3 μs	4.9 μs	3.8 μs	0.1 μs

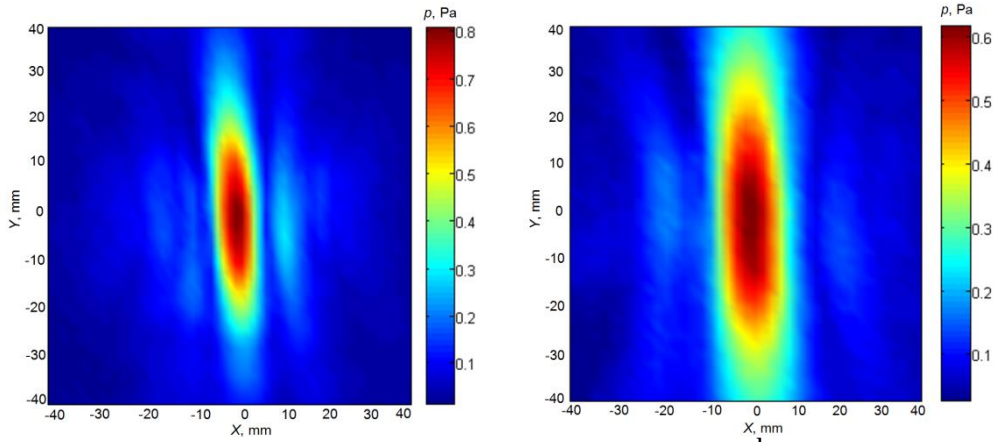

Fig. 4.6.4. Measured radiated acoustic fields in the case of the beam focused at different distances: a – at 10 mm, b – at 40 mm

The possibility to control electronically the deflection of the ultrasonic beam was also investigated. The elements of the array were excited thus introducing delays of the excitation instants according to the linear law:

$$\tau_i = \tau_0 \pm i\Delta t_i; \qquad (4.6.1)$$

where t_0 is the initial delay, Δt_i is the delay between adjacent elements and i is the number of the array element. The results illustrating the beam steering are shown in Fig. 4.6.5.

Such a presentation enables to obtain a better estimate of the transduction efficiency of the array. The ultrasonic beam deflection measurement results show very good beam steering possibilities in the range from –20° to +20°.

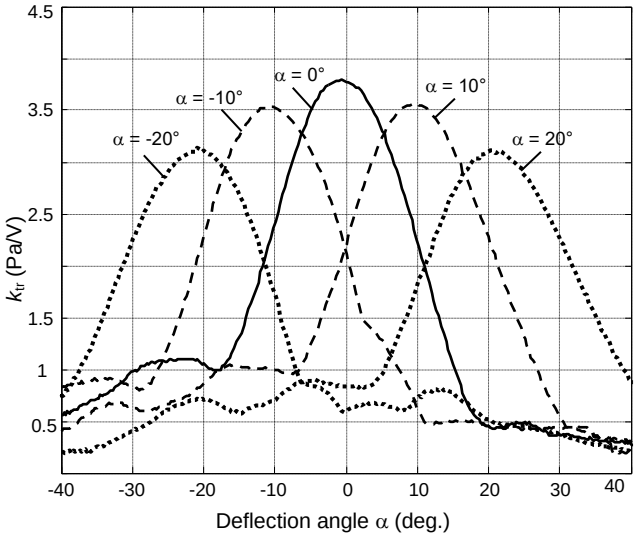

Fig. 4.6.5. Measured normalized acoustic pressure distributions across the ultrasonic beam at the distance of 80 mm from the array at various beam deflections angles α

We should note that in this case not absolute p but rather the normalized value of the acoustic pressure $k_{tr} = p/U_{pp}$ with respect to excitation voltage U_{pp} is presented in Fig. 4.6.5.

4.7. Conclusions

1. Multi-element low frequency (~40 kHz) air-coupled ultrasonic array consisting of strip-like PMN-32%PT crystals vibrating in the main transverse extension mode was proposed and investigated. The pitch between the individual elements was selected at slightly less than $\lambda_a/2$, where λ_a is the wave length in air.
2. For the improvement of the performance of the array, strip-like matching elements made of low acoustic impedance material AIREX R90.200 were developed. From the simulations and measurements results it follows that the best performance of the air-coupled ultrasonic array in terms of bandwidth and transduction losses is obtained with a thin (w = 1 mm) matching strip, the length of which is $\lambda/4$, where λ is the ultrasound velocity in the plastic strip.
3. The frequency response and the bandwidth of the array are quite similar to the frequency response of single array elements. The finite element modelling shows that the biggest displacements are obtained on the radiating surfaces of the matching strips whereas displacements of the opposite end of the piezoelectric element are almost 9 times smaller.
4. For the theoretical investigation of the radiated acoustic fields created by vibration of the air-coupled array of rectangular pistons, the impulse response

method (IRM) was chosen. Theoretical and experimental investigations of the acoustic fields radiated by the 8-element ultrasonic array demonstrated not only good performance of the array in the pulse mode, but also excellent possibilities of electronically steering the ultrasonic beam in space as well.

CONCLUSIONS

1. Piezoelectric PMN-32%PT single crystal elements rectangular plates and strips have been investigated. Extraordinarily high piezoelectric properties of the PMN-32%PT crystals allow the development of a new type of air-coupled ultrasonic transducers denoted by excellent performance.
2. A novel measurement technique for the simultaneous monitoring of the piezoelectric properties and structural changes of the PMN-32%PT single crystal during the poling process has been proposed and successfully performed. It has been clearly demonstrated how the domain structure transforms and how the piezoelectric properties of the PMN-32%PT crystals develop during the poling process. The standard uncertainty of additional capacitors is u (C_S) = ±0.5%. The standard uncertainty of the electromechanical coupling coefficient is u (k^*_{32}) = ±0.24%. The expanded measurement uncertainty is U_k = 1.1%.
3. For low frequency (<100 kHz) air-coupled ultrasonic transducers as active elements, PMN-32%PT crystal strips with <011> cut and [011] poling direction vibrating in the main transverse extension mode (TE) in the direction were proposed. PMN-32%PT single element transduction coefficient k_{32} is 25 times better than that of the PZT-29 element (f_r = 50 kHz) whereas mechanical displacement ξ is 11 times better than that of the similar PZT-29 element with the matching strip. The developed transducer possesses the transaction losses of –13.5 dB with the frequency of f_r = 41.5 kHz at the distance of 1 mm.
4. For the improvement of the transduction efficiency and pulse responses, strip-like matching elements made of low acoustic impedance plastic AIREX R90.200 were proposed. The ultrasonic array consisting of 8 PMN-32%PT crystal strips (15 x 5 x 1) mm^3 with the $\lambda/4$ matching strips operating in the transverse extension mode in the direction of y (2) axis was developed. Good agreement between the finite element simulation and the measurement results was observed.
5. For the theoretical investigation of the radiated acoustic fields created by a vibrating air-coupled array of rectangular pistons, the impulse response method (IRM) was chosen. Theoretical and experimental investigations of the acoustic fields radiated by the 8-element ultrasonic array demonstrated not only good performance of the array in the pulse mode but also excellent capacity of steering the ultrasonic beam in space electronically as well. ~14% mismatch between the simulation and the measurement results was observed.

FUTURE RESEARCH

In this dissertation, the measurement method of the piezoelectric properties of PMN-PT single crystals during the poling process and crystals for novel air-coupled ultrasonic transducers and multi-element arrays was investigated. The finite element modelling and experiments showed that the performance of the developed air-coupled ultrasonic transducer is a few times superior to that of the air-coupled PZ-29 composite ultrasonic transducer of similar dimensions. The investigation of the acoustic fields radiated in air by the developed multi-element arrays was also conducted.

The future research should focus on:

1. Thorough investigation of the domain structure and its properties during the poling process.
2. Investigation of ultrasonic air-coupled transducers operating both in the transmitting and receiving modes.

REFERENCES

1. CHIMENTI D.E. Review of air-coupled ultrasonic materials characterization. *Ultrasonics*, 2014, vol. 54, 1804-1816. ISSN 0041-624X.
2. CASTAINGS M., CAWLEY P. The generation, propagation, and detection of Lamb waves in plates using air-coupled ultrasonic transducers. *Journal of Acoustical Society of America*, 1996, vol. 100, 3070–3077. ISSN 0001-4966.
3. LI C., HUTCHINS D., GREEN R.J. Short-range ultrasonic communications in air using quadrature modulation. *IEEE Trans. Ultrason. Ferroelectr. Freq. Control*, 2009, vol. 56, 2060–2072. ISSN 0885-3010.
4. HALLER M.I., KHURI-YAKUB B.T. Micromachined 1-3 composites for ultrasonic air transducers. *Rev. Sci. Instr.*, 1994, vol. 65, 2095–2098. ISSN 0034-6748.
5. GOMEZ ÁLVAREZ-ARENAS T.E. Air-Coupled Piezoelectric Transducers with Active Polypropylene Foam Matching Layers. *Sensors*, 2013, vol. 13, 5996-6013. ISSN 1424-8220.
6. ZHANG S., LI, F. High performance ferroelectric relaxor-$PbTiO_3$ single crystals: Status and perspective. *Journal of Applied Physics*, Feb. 2012, vol. 111, no. 3. ISSN 0021-8979.
7. DAVIS M., DAMJANOVIC D. and SETTER N. The Direct Piezoelectric Effect in $[001]_C$ – Poled Relaxor – Ferroelectric Single Crystals Contrasting Longitudinal and Transverse Modes. In *2004 IEEE International Ultrasonics, Ferroelectrics, and Frequency Control Joint 50th Anniversary Conference, August 23-27, 2004.* Applications of Ferroelectrics, 2004. ISAF-04. 2004 14th IEEE International Symposium, 2004, 102-105.
8. LI F., LI, J., XU Z. and ZHANG S. Electrostrictive effect in ferroelectrics: An alternative approach to improve piezoelectricity. *Journal of Applied Physics*, 2014; 1:011103. ISSN 0021-8979.
9. CHEN R., NESTOR CABRERA-MUNOZ E., LAM K.H., et al. PMN-PT Single-Crystal High-Frequency Kerfless Phased Array. *IEEE Trans. Ultrason. Ferroelectr. Freq. Control*, 2014, vol. 61, 1033–1041. ISSN 0885-3010.
10. EDWARDS G., CHAN H. L.W., BATTEN A., LAM K.H., LUO H.S. and SCOTT, D.A. PMN-PT single crystal transducer for non-destructive evaluation. *Sens. Actuators A*, Nov. 2006, vol. 132, no. 2, 434–440. ISSN 0924-4247.
11. KAZYS R.J., SLITERIS R., SESTOKE J., VLADISAUSKAS A. Air – coupled Ultrasonic Transducers based on an Application of the PMN-32%PT Single Crystals. *Ferroelectrics. Abingdon: Taylor& Francis.* 2015, vol. 480, issue 1, 85-91. ISSN 0015-0193.
12. KAZYS R.J., SLITERIS R., SESTOKE J. Application of PMN-32PT piezoelectric crystals for novel air-coupled ultrasonic transducers. *Physics procedia*, 2015, vol. 70, 896-900. ISSN 1875-3892.

13. KAZYS R.J., SLITERIS R., SESTOKE J. Development of Air–Coupled Low Frequency Ultrasonic Transducers and Arrays with PMN-32%PT Piezoelectric Crystals. *IEEE International Ultrasonics Symposium (IUS),* October 2015, 1-4, ISBN 9781479981823.
14. BIATEAU C., HOSTEN B. and ROZIERE R. Measurement of Air-Coupled Transducer Characteristics for Ultrasonic Non-destructive Evaluation. *Review of Quantitative Nondestructive Evaluation,* 2002, vol. 21, 921-928.
15. LEVASORT F., PASCAL TRAN-HUU-HUE L., CERTON D. and LIETHIECQ M. Piezoelectric materials for ultrasonic transducers: review of recent developments. [Referred to the version presented on February 1, 2016]. Available online at: http://webistem.com/acoustics2008/acoustics2008/cd1/data/fa2002-sevilla/forumacusticum/archivos/ult04010.pdf.
16. HOSTEN B., CASTAINGS M. The use of electrostatic, ultrasonic, air-coupled transducers to generate and receive Lamb waves in anisotropic, viscoelastic plates. *Ultrasonics,* 1998, vol. 36, 361-365. ISSN 0041-624X.
17. RAIŠUTIS R., KAŽYS R., ŽUKAUSKAS E. and MAŽEIKA L. Ultrasonic air-coupled testing of square-shape CFRP composite rods by means of guided waves. *NDT& E International,* 2011, vol. 44, 645-654. ISSN 0963-8695.
18. SALAZAR J., TURO A. et al. High-Power High-Resolution Pulser for Air-Coupled Ultrasonic NDE Applications. *IEEE Transactions on Instrumentation and Measurement,* December, 2003, vol. 52, no. 6, 1792-1797. ISSN 0018-9456.
19. BLOMME E., BULCAEN D. and DECLERCQ F. Recent observations with air-coupled NDE in the frequency range of 650 kHz to 1.2 MHz. *Ultrasonics,* 2002, vol. 40, 153-157. ISSN 0041-624X.
20. YANO T., TONE M. and FUKUMOTO A. Range Finding and Surface Characterization Using High-frequency Air Transducers. *IEEE Transactions on Ultrasonics, Ferroelectrics, and Frequency Control,* March 1987, vol. UFFC-34, no. 2, 232-236. ISSN 0885-3010.
21. TODA M. New Type of Matching Layer for Air-Coupled Ultrasonic Transducers. *IEEE Transactions on Ultrasonics, Ferroelectrics, and Frequency Control,* July 2002, vol. 49, no. 7, 972-979. ISSN 0885-3010.
22. KAŽYS R., DEMČENKO A., ŽUKAUSKAS E., MAŽEIKA L. Air-coupled ultrasonic investigation of multi-layered composite materials. *Ultrasonics,* 2006, vol. 44, 819-822. ISSN 0041-624X.
23. GOMEZ ÁLVAREZ-ARENAS T.E. Acoustic impedance matching of piezoelectric transducers to the air. *IEEE Transactions on Ultrasonics, Ferroelectrics, and Frequency Control,* 2004, vol. 51, no. 5, 624- 633. ISSN 0885- 3010.
24. GALBRAITH W., HAYWARD G. Development of a PVDF membrane hydrophone for use in air-coupled ultrasonic transducer calibration. *IEEE*

Transactions on Ultrasonics, Ferroelectrics, and Frequency Control, November 1998, vol. 45, 1549-1558. ISSN 0885-3010.
25. KAŽYS R. J., VOLEISIS A. and ŽUKAUSKAS E. Wideband air-coupled ultrasonic transducers. *Ultragarsas*, 2004, No. 3 (52), 21-28. ISSN 1392-2114.
26. BUIGAS M., MONTERO F. et al. Electro-acoustical characterization procedure for cMUTs. *Ultrasonics,* March, 2005, vol. 43, issue 5, 383-390. ISSN 0041-624X.
27. PREGO BORGES J.L., MONTERO DE ESPINOSA F. et al. Diffraction aperture non-ideal behaviour of air coupled transducers array elements designed for NDT. *Ultrasonics,* 2006, vol. 44, 667-672. ISSN 0041-624X.
28. GOMEZ ÁLVAREZ-ARENAS T. E. Air-Coupled Transducers Based on 1-3 Connectivity Single Crystal Piezocomposites. *2012 IEEE International Ultrasonics Symposium*, 7-10 October 2012, 2230 – 2233. ISSN 1051-0117.
29. HC Materials Corporation. Piezoelectric PMN-PT Single Crystal Products. HC Materials. Referred to the version presented on February 22, 2016. Available online at http://www.hcmat.com/.
30. ZHOU Q., LAU, S. et al. Piezoelectric films for high frequency ultrasonic transducers in biomedical applications. *Progress in Material Science,* 2011, vol. 56, 139-174.
31. YOKONO Y. et al. Air-Coupled Ultrasonic Inspection technique for FRP Structure. *12th A-PCNDT 2006 – Asia-Pacific Conference on NDT, 5th*, November 2006. [Open 2016-06-01]. Website http://www.ndt.net/article/apcndt2006/papers/56.pdf.
32. TICHY J., ERHART J., KITTINGER E., PRIVRATSKA J. Fundamentals of piezoelectric sensorics, 2010, *Springer*, vol. 60, 146-197. ISBN 978-3-540-43966-0.
33. TIAN J., HAN P. and PAYNE D. Measurement Along the Growth Direction of PMN-PT Crystals: Dielectric, Piezoelectric, and Elastic Properties. *IEEE Transactions on Ultrasonics, Ferroelectrics, and Frequency Control*, September 2007, vol. 54, no. 9. ISSN 0885-3010.
34. CHEN H., GE C. et al. Growth of lead molybdate crystals by vertical Bridgman method. *Indian Academy of Sciences.* October 2005, vol. 28, no. 6, 555-560.
35. RAO W.F., XIAO K.W. et al. Control of domain configurations and sizes in crystallographically engineered ferroelectric single crystals: Phase field modelling. *Applied Physics Letters,* 2010, vol. 97.
36. DU Z., ZHU M., ZHANG T. and MA. J. Crystallization of Pb((Zn, $Mg)_{1/3}Nb_{2/3})O_3$-$PbTiO_3$ Thin Films Via Immobilization of Pb^{2+} Ions During Sol-Gel Process. *Journal of the American Ceramic Society*, 2010, vol. 93, 4036-4040.
37. PARK S. E. and SHROUT T. R. Ultrahigh strain and piezoelectric behaviour in relaxor based ferroelectric single crystals. *Journal of Applied*

Physics, August 1997, vol. 82. ISSN 0021-8979.
38. MATHEW D., DAMJANOVIC D., HAYEM D., SETTER N. Domain engineering of the transverse piezoelectric coefficient in perovskite ferroelectrics. *Journal of Applied Physics*, 2015, vol. *98.* ISSN 0021-8979.
39. BAEK S. H., RZCHOWSKI M. S. and AKSYUK V. A. Giant piezoelectricity in PMN-PT thin films: Beyond PZT. *Materials Research Society 2012*, November 2012, vol. 37, 1022-1029. ISSN 0272-9172.
40. *Piezoelectric Properties of Ceramic Materials and Components, Part 1: Terms and Definitions*, Eur. Std. EN 50324, 2002.
41. ZHANG R., JIANG W., JIANG B. and CAO W. Elastic, Dielectric and Piezoelectric Coefficients of Domain Engineered $0.70Pb(Mg_{1/3}Nb_{2/3})O_3$-$0.30PbTiO_3$ Single Crystal. *China Materials Letters*, 2005, vol. 59.
42. HE C., JING W., WANG F., ZHU K. and QIU J. Full Tensorial Elastic, Piezoelectric and Dielectric Properties Characterization of [011]-Poled PZN-9%PT Single Crystal. *IEEE Transactions on Ultrasonics, Ferroelectrics, and Frequency Control*, June 2011, vol. 58, no. 6. ISSN 0885-3010.
43. CHEN C., ZHANG R., WANG Z. and CAO W. Electromechanical coupling coefficient k_{31}^{eff} for arbitrary aspect ratio resonators made of [001] and [011] poled $(1-x)Pb(Mg_{1/3}Nb_{2/3})O_3$-$xPbTiO_3$. *Journal of Applied Physics*, 2009 Mar 15, vol. 105. ISSN 0021-8979.
44. ZHANG S., SHROUT T.R. Relaxor-PT Single crystals: Observations and Developments. *IEEE Transactions on Ultrasonics, Ferroelectrics, and Frequency Control*, October 2010, vol. 57, no. 10. ISSN 0885-3010.
45. RITTER T., GENG X. et al. Single Crystal PZN/PT-Polymer Composites for Ultrasound Transducer Applications. *IEEE Transactions on Ultrasonics, Ferroelectrics, and Frequency Control*, July 2000, vol. 47, no. 4. ISSN 0885-3010.
46. GUO W., JIN D. et al. Low temperature piezoelectric and dielectric properties of lead magnesium niobate titanate single crystals. *Journal of Applied Physics*, 2007, vol. 102. ISSN 0021-8979.
47. WANG Y., WING S. et al. Giant magnetoelectric effect in mechanically clamped heterostructures of magnetostrictive alloy and piezoelectric crystal-alloy cymbal. *Applied Physics Letters*, 2008, vol. 93.
48. JIN B. M., GUO R. and BHALLA, A.S. Piezoelectric properties and equivalent circuits of ferroelectric relaxor single crystals. *Journal of Materials Science*, 1997, vol. 32, Issue 8, 2055-2058.
49. HANA P., BURIANOVA L. et al. Elastic Stiffness Constants of PZN-4.5%PT Single Crystal Influenced by DC Bias Electric Field Applied at Various Directions to Prototypic Crystal Symmetry. *Ferroelectrics. Abingdon: Taylor& Francis*, 2005, vol. 319, 145-154. ISSN 0015-0193.
50. ZHU B. P., GUO W.K. et al. Structure and Electrical Properties of (111)-Oriented $Pb(Mg_{1/3}Nb_{2/3})O_3$-$PbZrO_3$-$PbTiO_3$ Thin Film for Ultra-High-

Frequency Transducer Applications. *IEEE Transactions on Ultrasonics, Ferroelectrics, and Frequency Control*, September 2011, vol. 58, no. 9. ISSN 0885-3010.

51. HAN J., CAO W. Interweaving domain configurations in [001]-poled rhombohedral phase $0.68Pb(Mg_{1/3}Nb_{2/3})O_3$-$0.32PbTiO_3$ single crystals. *Applied physics letters*, September 2003, vol. 83, no. 10.
52. *IEEE Standart on Piezoelectrisity*, ANSI/IEEE Std., 1987, 176-1987.
53. *Guide to Dynamic Measurements of Piezoelectric Ceramics With High Electromechanical Coupling*, Int. Std. CEI/IEC 60483, 1976, 1997 p. 40, ICS 31.140.
54. CHEN K.C. Studies of PZT/EPOXY and PMN-PT/EPOXY composites for ultrasonic transducer application. Dissertations, August 2000, Hong Kong Polytechnic University. Referred to the version presented on February 22, 2016. Available online at http://ira.lib.polyu.edu.hk/bitstream/10397/3349/2/b15354283.
55. TIAN J., HAN P., PAYNE D.A. Measurement along the growth direction of PMN-PT crystals: dielectric, piezoelectric, and elastic properties. *IEEE transactions on ultrasonics, ferroelectrics and frequency control*, September 2007, vol. 54, No. 9. ISSN 0885-3010.
56. *Piezoelectric Ceramics Characterization*, ICASE, NASA/CR-2001-211225.
57. JIANG W., ZHANG R., JIANG B. and CAO W. Characterization of piezoelectric materials with large piezoelectric and electromechanical coupling coefficients. *Ultrasonics*, March 2003, vol. 41, 55–63. ISSN 0041-624X.
58. FIALKA J., BENEŠ P. Comparison of Methods for the Measurement of Piezoelectric Coefficients. *IEEE Transactions on Ultrasonics, Ferroelectrics, and Frequency Control*, May 2013, vol. 62, no. 5. ISSN 0885-3010.
59. KHOLKIN A.L., WUTCHRICH Ch. et al. Interferometric measurements of electric field-induced displacements in piezoelectric thin films. *Review of Scientific Instruments.* May 1996, vol. 67, 1935-1941. ISSN 0034-6748.
60. FIALKA J., SKULA D. Utilization of the laser interferometer for the measurement of piezoelectric charge constant d_{31} and d_{33}. Doctoral degree programme (2, 3), FEEC BUT.
61. SHARAPOV V. *Piezoelectric Sensors, Microtechnology and MEMS*, 2011, Springer-Verlag: Berlin Heidelberg. ISBN 978-3-642-15311-2.
62. КАЖИС, Р.Й., ДОМАРКАS, В.И. Контрольно-измерительные пьезоелектрические преобразователи. Вильнюс, 1975.
63. KAZYS R. J. Ультраэвуковые информационно-измерительные системы. Вильнюс, 1986.
64. ZHANG R., JIANG B. and CAO W. Characterization of piezoelectric materials using ultrasonic and resonant techniques. *Medical Imaging 1998: Ultrasonic Transducer Engineering*, May 1998, vol. 154.

DOI:10.1117/12.307996.
65. MAEL G., HICHEM D. et al. Electromechanical properties of single domain PZN-12%PT measured by three different methods. *Solid State Sciences*, March 2010, vol. 12, 298–301.
66. JORDAN T.L., QUANAIES Z. *Piezoelectric Ceramics Characterization*. Institute for Computer Applications in Science and Engineering (ICASE), 2001.
67. OHNO I. Rectangular Parallelepiped Resonance Method for Piezoelectric Crystals and Elastic Constants of Alpha-Quartz. *Physics and chemistry of minerals*, 1990, vol. 17, 371-378.
68. YARALIOGLU G.G., ERGUN A.S. et al. Calculation and Measurement of Electromechanical Coupling Coefficient of Capacitive Micromachined Ultrasonic Transducers. *IEEE Transactions on Ultrasonics, Ferroelectrics, and Frequency Control*, April 2003, vol. 50, no. 4. ISSN 0885-3010.
69. LIU J.M., PAN B. et al. Piezoelectric coefficient measurement of piezoelectric thin films: an overview. *Material Chemistry and Physics*, 2002, vol. 75, 12-18.
70. LANG S.B. Ultrasonic Method for Measuring Elastic Coefficients of Bone and Results on Fresh and Dried Bovine Bones. *IEEE Transactions on Bio-Medical Engineering*, April 1970, vol. BME-17, no. 2.
71. KHOLKIN A., TANTIGATE C. and SAFARI A. Electromechanical properties of PMN-PT thin films prepared by pulsed laser deposition technique. *Integrated Ferroelectrics*, 1998, vol. 22, 515-523.
72. ABPLANALP M., BARASOVA D. et al. Scanning force microscopy of domain structures in $Pb(Zn_{1/3}Nb_{2/3})O_3$-8%$PbTiO_3$ and $Pb(Mg_{1/3}Nb_{2/3})O_3$-29%$PbTiO_3$. *Journal of Applied Physics*, March 2002, vol. 91, no. 6.
73. KOMMAREDDY V., PETERS J. J. et al. Air-Coupled ultrasonic measurements in composites. *Review of Quantitative Nondestructive Evaluation*, 2004, vol. 23, 859-866.
74. *Precision impedance analyser 6500B Series*, user manual, Wayne Kerr Electronics.
75. *Vibrometer Controller OFV-5000*, user manual, Polytec.
76. *Fiber-optic Vibrometer Sensor Head OFV-512*, user manual, Polytec.
77. Vibrometer Controller OFV-5000, user manual. Polytec. Open [2016 02 02]. Website http://www.polytec.com/fileadmin/user_uploads/Products/Vibrometers/OFV-5000/Documents/EN/OM_DS_OFV-5000_E_42346.pdf.
78. Ferroperm piezoceramics. Referred to the version presented on February 2, 2016. Available online at http://www.ferroperm-piezo.com.
79. Fiber-optic Vibrometer Sensor Head OFV-511/512, user manual. Polytec. Referred to the version presented on February 2, 2016. Available online at http://www.polytecpi.com/PDF/OFV-5000_Cont_Head_Decoders.pdf.
80. DAVIS M., DAMJANOVIC D. et al. Domain engineering of the transverse

piezoelectric coefficient in perovskite ferroelectrics. *Journal of Applied Physics*, 2005, vol. 98. ISSN 0021-8979.

81. KAZYS R. J., SLITERIS R., SESTOKE J. Monitoring of the Piezoelectric Properties and Structural Changes of the PMN-32%PT Crystals during Poling Process. *2014 Joint IEEE International Symposium on the Applications of Ferroelectric, International Workshop on Acoustic Transduction Materials and Devices & Workshop on Piezoresponse Force Microscopy, May 12-16, 2014.* ISSN 1099-4734.
82. KAZYS R. J, SLITERIS R., SESTOKE J. Simultaneous Monitoring of the Electromechanical Coupling Coefficients and Domain Structural Changes of the PMN-32%PT Crystals during Poling Process. *Ferroelectrics. Abingdon: Taylor& Francis.* 2015, vol. 480, issue 1, 24-31. ISSN 0015-0193.
83. TROLIER-MICKINSTRY S., MURALT P. Thin Film Piezoelectrics for MEMS. *Journal of Electroceramics*, January 2004, vol. 12, 7-17. ISSN 1573-8663.
84. BAEK S. H., PARK J. et al. Giant Piezoelectricity on Si for Hyperactive MEMS. *American Association for the Advancement of Science*, Nov 2011, vol. 334, 958-961. ISSN 1533-5046.
85. ZHANG R., JIANG B., JIANG W. and CAO W. Anisotropy in Domain Engineered $0.92Pb(Zn_{1/3}Nb_{2/3})O_3$-$0.08PbTiO_3$ Single Crystal and Analysis of its Property Fluctuations. *IEEE Transactions on Ultrasonics, Ferroelectrics, and Frequency Control*, December 2002, vol. 49, no. 12. ISSN 0885-3010.
86. ZHANG R., JIANG B. and CAO W. Single-domain properties of $0.67Pb(Mg_{1/3}Nb_{2/3})O_3$-$0.33PbTiO_3$ single crystals under electric field bias. *Journal of Applied Physics.* 2003, vol. 82, 787. ISSN 0021-8979.
87. PARK S.E., SHROUT T. R. Ultrahigh strain and piezoelectric behaviour in relaxor based ferroelectric single crystals. *Journal of Applied Physics.* 1997, vol. 82, 1804. ISSN 0021-8979.
88. LI F., ZHANG S. et al. Composition and phase dependence of the intrinsic and extrinsic piezoelectric activity of domain engineered $(1-x)PB(Mg_{1/3}Nb_{2/3})O_3$-$xPBTiO_3$ crystals. *Journal of Applied Physics*, 2010, Vol. 108. ISSN 0021-8979.
89. BROWN J.A., DUNPHY K. et al. Fabrication and performance of a single-crystal lead magnesium niobate-lead titanate cylindrical hydrophone. *Acoustical Society of America.* August 2013, vol. 134, no. 2, 1031-1038. ISSN 0001-4966.
90. KIM M., KIM J., CAO W. Aspect ratio dependence of electromechanical coupling coefficient of piezoelectric resonators. *Applied Physics Letter*, 2005, vol. 87, 132901.
91. OGAWA T., MATSUSHITA M. and YOSHIOKA, K. Giant Electromechanical Coupling factor of k_{31} Mode in $Pb(Zn_{1/3}Nb_{2/3})O_3$-$PbTiO_3$ and $Pb(Mg_{1/3}Nb_{2/3})O_3$-$PbTiO_3$ Single Crystals. *Ferroelectrics. Abingdon:*

Taylor& Francis, 2006, vol. 339, 3-11. ISSN 0015-0193.
92. KOZIELSKI L., ERHART J. and CLEMENS F.J. Light-Intensity-Induced Characterization of Elastic Constants and d33 Piezoelectric Coefficient of PLZT Single Fiber Based Transducers. *Sensors,* 2013, vol. 13, 2419-2429. ISSN 1424-8220.
93. CHOI K.C., MARGRAVES H.C., JUN I.S. et al. Opto-Electric Cellular Biosensor Using Optically Transparent Indium Tin Oxide (ITO) Electrodes. *Sensors*, 2008, vol. 8, 3257-3270. ISSN 1424-8220.
94. KAŽYS R.J., MAZAK E. The features of disk shape piezoelectric ceramic transducer equivalent circuit. *Acustica*, 1973; vol. 28, 208-214.
95. Measurement uncertainty in testing. *European federation of national Associations of measurement, Testing and Analytical Laboratories*. Technical report. 2002, vol. 1, 10-41.
96. NADER G., SILVA E.C.N. and ADAMOWSKI J.C. Effective Damping Value of Piezoelectric Transducer Determined by Experimental Techniques and Numerical Analysis. *Symposium Series in Mechatronics,* 2004, vol. 1, 271-279. ISBN 85-857699-20-3.
97. LERCH R. Simulation of Piezoelectric Devices by Two and Three-Dimensional Finite Elements. *IEEE Transactions on Ultrasonics, Ferroelectrics, and Frequency Control,* May 1990, vol. 37, no. 2. ISSN 0885-3010.
98. ANSYS Theory Manual. Referred to the version presented on July 26, 2016. Available online at http://148.204.81.206/Ansys/150/ANSYS%20Mechanical%20APDL%20Theory%20Reference.pdf.
99. JOO H.W., LEE C.H., JUNG H.K. Identification of the piezoelectric material coefficients using the finite element method with an asymptotic waveform evaluation. *Ultrasonics,* 2004, vol. 43, 13-19. ISSN 0041-624X.
100. VLADISAUSKAS A., ZUKAUSKAS E., SLITERIS R., RAISUTIS R., SENIUNAS G. Development of the non-damped wide-band ultrasonic transducers. *Ultrasound,* 2010, vol. 65, no. 4. ISSN 1392-2114.
101. IOVANE G., NASEDKIN A.V. Modal analysis of piezoelectric bodies with voids. II. Finite element simulation. *Applied Mathematical Modelling,* 2010, vol. 34, 47-59. ISSN 0307-904X.
102. KAZYS R., DEMCENKO A. et al. Air-coupled ultrasonic investigation of multi-layered composite materials. *Ultrasonics,* 2006, vol. 44, 819-822. ISSN 0041-624X.
103. VLADISAUSKAS A., ZUKAUSKAS E. et al. Development of the non-damped wide-band ultrasonic transducers. *Ultrasound,* 2010, vol. 65, no. 4.
104. KELLY S.P., HAYWARD G. et al. Characterization and Assessment of an Integrate Matching Layer for Air-Coupled Ultrasonic Applications. *IEEE Transactions on Ultrasonics, Ferroelectrics, and Frequency Control,* October 2004, vol. 51, no. 10, 1314-1323. ISSN 0885-3010.

105. SUN P., WANG G. et al. High Frequency PMN-PT 1-3 Composite Transducer for Ultrasonic Imaging Application. *Ferroelectrics. Abingdon: Taylor& Francis*, 2010, vol. 408, 120-128. ISSN 0015-0193.
106. HSU H.S., BENJAUTHRIT V. et al. PMN-PT-PZT composite films for high frequency ultrasonic transducer applications. *Sensors and Actuators A: Physical*, 2012, vol. 179, 121-124.
107. LIU D., YUE Q. et al. Broadband and High Sensitive Time-of-Flight Diffraction Ultrasonic Transducers Based on PMNT/Epoxy 1-3 Piezoelectric Composite. *Sensors*, 2015, vol. 15, 6807-6817. ISSN 1424-8220.
108. CHENG K.C., CHAN L.W. et al. Single crystal PMN-0.33PT/Epoxy 1-3 Composites for Ultrasonic Transducer Applications. *IEEE Transactions on Ultrasonics, Ferroelectrics, and Frequency Control*, September 2003, vol. 50, no. 9. ISSN 0885-3010.
109. KAZYS R., RAISUTIS R. et al. Air-coupled ultrasonic testing of CFRP rods by means of guided waves. *Physics Procedia*, 2010, vol. 3, 185-192.
110. CHEN R., NESTOR E. et al. PMN-PT Single-Crystal High-Frequency Kerfless Phased Array. *IEEE Transactions on Ultrasonics, Ferroelectrics, and Frequency Control*, June 2014, vol. 61, no. 6. ISSN 0885-3010.
111. BRÜEL & KJÆR. Product Data. Condenser Microphone Cartridges – Types 4133 to 4181. Referred to the version presented on May 3, 2016. Available online at http://www.bksv.com/doc/Bp0100.pdf.
112. BRÜEL & KJÆR. Product Data. The NEXUS Range of Conditioning Amplifiers Types 2690, 2691, 2692 and 2693. Referred to the version presented on May 3, 2016. Available online at http://www.upc.edu/sct/documents_equipament/d_157_id-560.pdf.
113. SAN EMETERIO J.L. Diffraction impulse response of rectangular transducers. *Journal of the Acoustical Society of America*, Aug. 1992, vol. 92, no. 2, pt. 1, 651-662. ISSN 0001-4966.
114. REIBOLD R., KAŽYS, R. Radiation of a rectangular strip-like focussing transducer. Part 1: harmonic excitation. *Ultrasonics*, 1992, vol. 30, no. 1, 49-55. ISSN 0041 624X.
115. REIBOLD R., KAŽYS, R. Radiation of a rectangular strip-like focussing transducer. Part 1: transient excitation. *Ultrasonics*, 1992, vol. 30, no. 1, 56-59. ISSN 0041 624X.
116. PREGO-BORGES J.L. The Lamb Matlab® toolbox, 1 Aug. 2010, first release, beta version 0.1. Referred to the version presented on May 13, 2016. Available online at http://se.mathworks.com/matlabcentral/fileexchange/28367-the-lamb-toolbox.
117. PREGO-BORGES J. Lamb: a simulation tool for air-coupled Lamb wave based ultrasonic NDE systems. PhD dissertation, 2010, The Polytechnic University of Catalonia (UPC), Department of Electronic Engineering

(EEL). Referred to the version presented on May 13, 2016. Available online at www.tdx.cat/bitstream/10803/6376/1/TJLPB1de1.pdf.

118. NEILD A., HUTCHINS D.A., ROBERTSON T.J., DAVIS L.A.J., BILLSON D.R. The radiated fields of focussing air-coupled ultrasonic phased arrays. *Ultrasonics*, 2005, vol. 43, no. 3, 183-195. ISSN 0041 624X.
119. CHEN J., DAI J.Y. et al. Broadband Focusing Ultrasonic Transducers Based on Dimpled $LiNbO_3$ Plate With Inversion Layer. *IEEE Transactions on Ultrasonics, Ferroelectrics, and Frequency Control,* December 2012, vol. 59, no. 10. ISSN 0885-3010
120. FINK M.A., CARDOSO J.F. Diffraction Effects in Pulse-Echo Measurement. *IEEE Transactions on Sonics and Ultrasonics,* July 1984, vol. SU-31, no. 4, 313-329. ISSN 0018-9537.
121. KRAUTKRAMER J., KRAUTHRAMER H. *Welkstoffprufung mit Ultraschall.* Berlin: Springer-Verlag, 1986, pp. 95-99. ISBN 978-3-662-10909-0.
122. HUO X., ZHANG S. et al. Elastic, dielectric and piezoelectric characterization of single domain PIN-PMN-PT: Mn crystals. *Journal of Applied Physics,* 2012, vol. 112. ISSN 0021-8979.
123. LI X.M., ZHANG R. et al. Surface Acoustic Wave Propagation in Relaxor-Based Ferroelectric Single Crystals 0.93 $PB(Zn_{1/3}Nb_{2/3})O_3$-0.07$PbTiO_3$ Poled along $[011]_C$. *Chinese Physics Letters,* 2012, vol. 29.

LIST OF SCIENTIFIC PUBLICATIONS ON THE TOPIC OF DISSERTATION

ARTICLES
in the publications of the main list of the Institute of Scientific Information (ISI)

1. Kažys, Rymantas Jonas; Šliteris, Reimondas; Šeštokė, Justina. Simultaneous Monitoring of the Electromechanical Coupling Coefficients and Domain Structural Changes of the PMN-32%PT Crystals during Poling Process. Publisher: Ferroelectrics. Abingdon: Taylor& Francis. ISSN 0015-0193. 2015, vol. 480, issue 1, p. 24-31. DOI:10.1080/00150193.2015.1012405.
2. Kažys, Rymantas Jonas; Šliteris, Reimondas; Šeštokė, Justina; Vladišauskas, Alfonsas. Air-coupled Ultrasonic Transducers based on an Application of the PMN-32%PT Single Crystals. Publisher: Ferroelectrics. Abingdon: Taylor& Francis. ISSN 0015-0193. 2015, vol. 480, issue 1, p. 85-91. DOI: 10.1080/00150193.2015.1012458.
3. Kažys, Rymantas Jonas; Šliteris, Reimondas; Šeštokė, Justina. Monitoring of the piezoelectric properties and structural changes of the PMN-32%PT crystals during poling process // 2014 Joint IEEE International symposium on the applications of ferroelectrics, International workshop on acoustic transduction materials and device & Workshop on piezoresponse force microscopy (ISAF – IWATMD – PFM), May 12-16, 2014, The Pennsylvania State University, State College, PA, USA. Piscataway, NJ: IEEE, 2015, ISBN 9781479938605. p. 83-86.
4. Kažys, Rymantas Jonas; Šliteris, Reimondas; Šeštokė, Justina. Development of air-coupled low frequency ultrasonic transducers and arrays with PMN-32%PT piezoelectric crystals // IEEE International Ultrasonics Symposium (IUS), 21-24 October 2015, Taipei, Taiwan. Piscataway, NJ: IEEE, 2015, ISBN 9781479981823. p. [1-4]. DOI:10.1109/ULTSYM.2015.0214.
5. Kažys, Rymantas Jonas; Šliteris, Reimondas; Šeštokė, Justina. Application of PMN-32PT piezoelectric crystals for novel air-coupled ultrasonic transducers // Physics procedia: ICU international congress on ultrasonics, Metz, France, 11-14 May, 2015. Amsterdam: Elsevier. ISSN 1875-3892. 2015, vol. 70, p. 896-900. DOI: 10.1016/j.phpro.2015.08.185.

Articles in journals included in other international databases

1. Kažys, Rymantas Jonas; Šliteris, Reimondas; Šeštokė, Justina; Zienius, Marius. Investigation of high frequency mechanical displacements in PMN-32%PT crystals by laser interferometry // Solid State Phenomena. ISSN 1012 0394. 2016, vol. 251, p83-88.

Articles in journals included in other national databases

1. Kažys, Rymantas Jonas; Šliteris, Reimondas; Šeštokė, Justina; Zienius, Marius. Investigation of high frequency mechanical displacements in PMN-32%PT crystals by laser interferometry // Mechatronic systems and materials: abstracts of the 11th international conference, MSM 2015, 7-9 July 2015, Kaunas, Lithuania / Editors: I. Skiedraitė, R. Rimašauskienė, L. Zubrickaitė, E. Dragašius. Kaunas University of Technology. ISSN 1822-8283. 2015, p. 67-68.

REPORTS IN SCIENTIFIC CONFERENCES

1. Kažys, Rymantas Jonas; Šliteris, Reimondas; Šeštokė, Justina. Monitoring of the piezoelectric properties and structural changes of the PMN-32%PT crystals during poling process // 2014 IEEE ISAF/IWATMD/PFM: 2014 05 12-16, Penn State, USA;
2. Kažys, Rymantas Jonas; Šliteris, Reimondas; Šeštokė, Justina. Simultaneous Monitoring of the Electromechanical Coupling Coefficients and Domain Structural Changes of the PMN-32%PT Crystals during Poling Process // European Conference of Application of Polar Dielectrics 2014: 2014 07 07-11, Vilnius, Lithuania;
3. Kažys, Rymantas Jonas; Šliteris, Reimondas; Šeštokė, Justina; Vladišauskas, Alfonsas. Air-coupling Ultrasonic Transducers based on an Application of the PMN-32%PT Single Crystals // European Conference of Application of Polar Dielectrics 2014: 2014 07 07-11, Vilnius, Lithuania;
4. Kažys, Rymantas Jonas; Šliteris, Reimondas; Šeštokė, Justina. Application of PMN-32PT piezoelectric crystals for novel air-coupled ultrasonic transducers // 2015 International Congress on Ultrasonics: 2015 05 11-15, Metz, France;
5. Kažys, Rymantas Jonas; Šliteris, Reimondas; Šeštokė, Justina; Zienius, Marius. Investigation of high frequency mechanical displacements in PMN-32%PT crystals by laser interferometry // 11th International Conference Mechatronic Systems and Materials: 2015 07 07-09, Kaunas, Lithuania;
6. Kažys, Rymantas Jonas; Šliteris, Reimondas; Šeštokė, Justina. Development of Air-Coupled Low Frequency Ultrasonic Transducers and Arrays with PMN-32%PT Piezoelectric Crystals // IEEE International Ultrasonics Symposium: 2015 10 21-24, Taipei, Taiwan;
7. Kažys, Rymantas Jonas; Šliteris, Reimondas; Šeštokė, Justina. Development of air-coupled ultrasonic transducers based on PMN-PT type single crystals // 19th World Conference on Non-Destructive Testing: 2016 06 13-17, Munich, Germany.

SL344. 2016-10-24, 15,5 leidyb. apsk. l. Tiražas 10 egz. Užsakymas 392.
Išleido Kauno technologijos universitetas, K. Donelaičio g. 73, 44249 Kaunas
Spausdino leidyklos „Technologija“ spaustuvė, Studentų g. 54, 51424 Kaunas